Thèse n° 10 467

Nonlocally-resonant metamaterials

Présentée le 8 décembre 2023

Faculté des sciences et techniques de l'ingénieur
Laboratoire d'ingénierie des ondes
Programme doctoral en physique

pour l'obtention du grade de Docteur ès Sciences

par

Aleksi Antoine BOSSART

Acceptée sur proposition du jury

Prof. F. Mila, président du jury
Prof. R. C. R. Fleury, directeur de thèse
Prof. R. Craster, rapporteur
Prof. F. Lemoult, rapporteur
Prof. G. Tagliabue, rapporteuse

École
polytechnique
fédérale
de Lausanne

2023

Acknowledgements

First, I want to wholeheartedly thank my advisor, Prof. Romain Fleury. I particularly enjoyed our frequent discussions on a wide range of scientific topics. EPFL recently made you an associate professor, congratulations! Generations of students will now also have the privilege to learn with you.

I also would like to thank my thesis committee, Prof. Mila, Prof. Craster, Prof. Tagliabue and Prof. Lemoult, for carefully reading this manuscript and for our interesting scientific discussion during my private defence.

My next round of thanks goes to the members of LWE, starting with the other Ph.D. students: Rongrong and Zhe, who shared this Ph.D. journey with me from the very beginning. Our intense whiteboard sessions, fuelled by fruit, as well as our more introspective discussions have left a deep imprint on me. Our elders, Theodoros and Farzad, who shared their wisdom with us as we were taking the first steps in our Ph.D. lives. Ali, Haoye, Tim and Junda, who joined along the way, made the lab an even livelier place, bubbling with creativity.

Our postdocs provided bright examples of many different facets of science. I watched in awe as Bakhtiyar orchestrated complex experiments, always quickly isolating the root cause of any problem that arose. Nadège showed me the value of taking a step back, be it when considering a fundamental scientific concept or the next career move. Maliheh, how far taking an idea seriously can take you. Matthieu, through constant dedication and planning, taught me about the social arcanes of science. Janez taught me to approach experiments with an open mind, and finally, Benjamin showed me that the best scientists are not above dumpster-diving for parts and scientific equipment.

Many others stayed at LWE for shorter research projects and collaborations, Sajjad, Pierre, Bingkun, Jonas, Tinggui, Qiaolu and Zhechen. You all taught me a great deal, bringing new perspectives on things as well as many occasions to celebrate. Last among LWE but not least, I want to thank Mercedes and Eva for making all this frictionless, shielding us from the mysterious administrative forces that lurk in the shadows.

The ELB0 floor would feel empty without the acousticians and the MAGicians: Mathieu, Maxime, Stas, Xinxin, Behzad, Vincent, Thach, Qin, Hervé, Anja, Denys, Danelys, Hannes, Adrian, Ismael, Martin, Robin and many others. Thanks for the countless lunches, flights to orbit, and afterwork adventures.

This list would not be complete without David, Jop, Corentin, and many others from Amsterdam, with whom I took the first steps on the intellectual path that led to this thesis.

J'aimerais aussi remercier Duche, Rance, Steve Hottinger, Baba, Cam, Mel, Aless, Céline, Thildance, Mel, Laura, Gabance, Manon, Jess et Pierre pour leur amitié sans faille, pour nos plans foireux et grandioses, mais également pour leur patience lors de mes monologues impromptus.

Finalement, rien de tout cela n'aurait eu lieu sans l'amour et le soutien de ma famille, que je remercie du fond du cœur. Mes parents, Leena et Henri, pour m'avoir toujours encouragé, par l'exemple, à lire, à être curieux et à sortir des sentiers battus. Mon frère Maki pour les fous rires et les jeux. Notre grand-père Anton pour nous avoir montré, ainsi qu'à nos cousines Sophie et Wanda, que l'on peut comprendre et réparer bien des choses avec les bons outils. La même attitude règne à Nivala, où Aku, Merja, Toivo, Paavo et Mummu nous ont accueilli de nombreux étés. J'aimerais remercier ma grand-mère Anne-Marie pour m'avoir transmis son amour de la nature, ainsi que pour les merveilleux mardis midi qui ont peuplé mon enfance. Quant à sa sœur, Jacqueline, elle a toujours été pour moi un modèle de liberté et d'humour. De grands mercis à Isabelle et Bernard, entre autres pour m'avoir initié aux joies des sports de montagne. Merci à Chantal, Gregor, Adrien, Camille et Harry pour m'avoir si chaleureusement accueilli à Formangueires.

Pour finir, Alice, tu m'as donné le dernier mot [1]. Je vais l'utiliser pour te dire à quel point ma vie est entrée en résonance dès qu'elle a croisé la tienne ; tout est plus beau, plus intense avec toi. Merci pour tout.

Winterthur, October 21, 2023 Aleksi Bossart

Résumé

Dans cette thèse, nous dévoilons une troisième voie pour manipuler les ondes élastiques au sein de milieux architecturés, distincte des concepts traditionnels de cristal phononique et de métamatériau à résonance locale. L’innovation centrale repose sur le concept de résonances non locales, définies comme des modes à fréquence nulle possédant des vecteurs d’onde non nuls, ce qui entraîne la formation de cônes de dispersion anormaux dans le spectre ondulatoire. Ce principe de fonctionnement original permet aux métamatériaux à résonance non locale d’éviter le compromis entre la largeur de bande à indice négatif et la sous-longueur d’onde qui caractérise les médias ondulatoires architecturés traditionnels.

En introduisant les graphes cinématiques comme outil de conception visuelle pour les modes de fréquence nulle dans les métamatériaux élastiques planaires, nous identifions diverses classes de mise à l’échelle des modes nuls, en mettant l’accent sur la classe oligomodale, caractérisée par un nombre fixe de modes de déformation globaux indépendants de la taille du système. Partant de cette base, nous obtenons des résonances élastiques non locales en imposant une condition d’onde de Bloch aux modes nuls hébergés par les géométries oligomodales.

Cela ouvre la voie à une exploration approfondie de la physique des ondes dans les métamatériaux à résonance non locale, aboutissant à une approche de conception inverse pour positionner librement des cônes anormaux dans l’espace k. Nous validons ensuite notre théorie par une combinaison de simulations par éléments finis, d’expériences de compression et d’expériences de vibration, établissant la viabilité pratique des géométries oligomodales et des métamatériaux à résonance non locale.

Ayant solidement ancré le concept central de résonance non locale, nous délimitons ses frontières en étudiant divers cas limites. Nous commençons par considérer plusieurs cas de bandes de fréquences interdites, ainsi que des domaines de vecteurs d’ondes instables, ce qui nous permet entre autres de découvrir un lien direct entre les résonances non locales et la dynamique des points exceptionnels. Nous nous écartons ensuite de l’adhésion stricte à la condition d’onde de Bloch, révélant ainsi des états de bord et des signatures spectrales de loi de puissance. Cela nous permet d’étendre notre perspective d’ondes pour inclure également divers modes nuls non-Bloch qui émergent naturellement dans l’étude des géométries oligomodales.

Enfin, nous revenons aux milieux architecturés qui ont inspiré cette introduction du concept

de résonance non locale, à savoir les milieux de fils entrelacés électromagnétiques, en étudiant leur équivalent élastique direct. Cela enrichit notre discussion en nous permettant d'étudier l'interaction entre la symétrie et les résonances non locales dans un cadre tridimensionnel. En particulier, nous montrons que la théorie des représentations s'applique naturellement à l'espace de permutation des composants macroscopiques entrelacés qui constituent le milieu de fils entrelacés.

En conclusion, cette thèse présente un nouveau paradigme pour la manipulation des ondes élastiques, que nous appelons métamatériaux à résonance non locale, offrant de nouvelles perspectives pour les matériaux multifonctionnels et le contrôle avancé des ondes.

Mots clefs : métamatériaux, résonance non-locale, géométries oligomodales, dispersion spatiale, réfraction négative, bandes de fréquences interdites, rotons, matériaux à fils entrelacés, cristaux phononiques.

Abstract

In this thesis, we unveil a third design path to manipulate elastic waves within architected media, distinct from the traditional phononic crystal and locally-resonant metamaterial concepts. The core innovation lies in the concept of nonlocal resonances, defined as zero-frequency modes possessing non-zero wave-vectors, resulting in anomalous dispersion cones within the wave spectrum. This distinct working principle allows nonlocally-resonant metamaterials to circumvent the bandwidth-subwavelengthness trade-off that characterises traditional architected wave media.

Introducing kinematic graphs as a visual design tool for zero-frequency modes in planar elastic metamaterials, we identify various classes of zero-mode scaling, with a specific focus on the oligomodal class, characterised by a fixed number of global deformation modes that remain independent of system size. Building upon this foundation, we obtain elastic nonlocal resonances by imposing a Bloch-wave requirement on zero-modes hosted by oligomodal geometries.

This opens up the door to a comprehensive exploration of the wave physics of nonlocally-resonant metamaterials, culminating in an inverse design approach to freely position anomalous cones within k-space. We then validate our theory through a combination of full-wave simulations, compression experiments and vibration experiments, establishing the practical viability of oligomodal geometries and nonlocally-resonant metamaterials.

Having firmly anchored the core concept of nonlocal resonance, we chart out its boundaries by studying various edge cases. We start by considering mass gaps, higher-frequency gaps and momentum gaps, and discover a connection between nonlocal resonances and exceptional-point dynamics in the process. We then depart from strict adherence to the Bloch wave requirement, thus revealing edge states and power-law spectral signatures. This allows us to extend our wave perspective to also include various non-Bloch zero-modes that naturally arise in the study of oligomodal geometries.

Finally, we connect back to the architected media that inspired the introduction of the nonlocal resonance concept, namely electromagnetic interlaced wire media, by studying their direct elastic equivalent. This enriches our discussion by allowing us to investigate the interplay between symmetry and nonlocal resonances within a three-dimensional framework. In particular, we show that representation theory naturally applies to the permutation space of

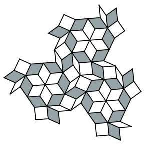

the macroscopic interlaced components that constitute the interlaced wire medium.
In conclusion, this thesis presents a novel paradigm for manipulating elastic waves, which we term nonlocally-resonant metamaterials, offering new vistas for multifunctional materials and advanced wave control.

Key words: metamaterials, nonlocally-resonant, oligomodal, spatial dispersion, negative refraction, band-gaps, rotons, interlaced, wire media, phononic crystals.

Contents

Acknowledgements **i**

Abstract **v**

List of figures **ix**

List of tables **xi**

1 Introduction **1**
- 1.1 The role of mesoscale structure in natural materials 1
- 1.2 Architected materials in wave physics 3
- 1.3 An alternative design path: nonlocal resonance 8

2 Kinematic Graphs **13**
- 2.1 Taming local mechanisms with the area law 15
  - 2.1.1 Kinematic graphs of four-bar linkages 17
  - 2.1.2 Combining elementary kinematic graphs 18
- 2.2 Mechanical tilings and zero-mode scaling 21

3 Anomalous Dispersion Cones **27**
- 3.1 Anomalous cone in a one-dimensional chain. 27
- 3.2 Multiple cones in an oligomodal metamaterial. 33
- 3.3 Broadband negative refraction 37
- 3.4 Anomalous cones on a field trip in k-space 40

4 Experimental Validation **45**
- 4.1 Actuating soft modes through uniaxial compression 45
- 4.2 Catching nonlocal resonances through vibrometry 50

5 Opening Gaps **55**
- 5.1 Gaps induced by additional couplings 55
- 5.2 Gaps induced at the kinematic graph level 60
- 5.3 Higher-frequency gaps and hybridisation 62

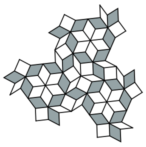

6 Non-Bloch Zero Modes **65**
- 6.1 The quadratic spectral signature of the elusive rotational zero-mode. 65
- 6.2 Power-law mode profiles in oligomodal geometries. 67
- 6.3 Concluding remarks. 70

7 The Role of Symmetry **73**
- 7.1 Space group redux 73
- 7.2 Weakly coupled elastic IWMs 78
- 7.3 Permuting giant components with isometries 79
- 7.4 Conclusion 85

8 Discussion and Outlook **87**
- 8.1 What we explored 87
  - 8.1.1 A design pathway based on nonlocal resonances 87
  - 8.1.2 A map of boundaries 88
- 8.2 *Hic sunt dracones* 90
  - 8.2.1 Metamaterials with roton-like dispersion and gapped elastic IWMs are two faces of the same coin 91
  - 8.2.2 Continuum theories for nonlocally-resonant metamaterials 91
  - 8.2.3 Entering the nonlinear regime 92
  - 8.2.4 Potential connections to condensed-matter physics 93
- 8.3 Conclusion 93

A Proof of lattice-integer relation **95**

B Details of the inverse design method **97**

C Fractal spectrum in quasicrystals **101**

Bibliography **119**

Curriculum Vitae **121**

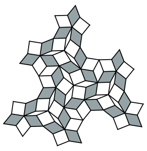

List of Figures

1.1 Hierarchy of mesoscale structure in natural materials. 2
1.2 The mesoscale structure of peafowl feathers lends them their iridescent colour. 3
1.3 The rise of architected media in wave physics. 4
1.4 The two traditional pathways to wave control in architected materials. 5
1.5 Ashby plot comparing the negative properties of various architected media. . . 7
1.6 The quest for an elastic counterpart to interlaced wire media. 9
1.7 Another historical strand: flexible metamaterials. 10

2.1 Kinematic degrees of freedom in a truss-hinge network. 14
2.2 Linearising the kinematics of a four-bar mechanism. 16
2.3 Some examples of arrow rules. 17
2.4 Decomposing the kinematics of an arbitrary cyclic linkage. 19
2.5 Simplifying the kinematics of a composite unit cell to an equivalent vertex. . . 20
2.6 Kinematic graphs of a bimodal linkage. 21
2.7 Localized modes and their extensive scaling. 21
2.8 The counter-rotating squares mechanism. 23
2.9 An oligomodal metamaterial. 24
2.10 Quasicrystalline geometry with logarithmically scaling number of mechanisms. 25

3.1 Minimal 1D model exhibiting a single anomalous cone. 28
3.2 Sending pulses through a nonlocally-resonant chain. 31
3.3 The spectral signature of line modes. 32
3.4 Multiple anomalous cones in a planar nonlocally-resonant metamaterial. . . . 34
3.5 Comparison between spring-mass and FEM spectra. 36
3.6 Negative refraction in a nonlocally-resonant metamaterial. 38
3.7 Probing the bandwidth of nonlocally-resonant negative refraction. 39
3.8 Oligomodal geometry with anomalous cones at Γ and M. 41
3.9 A geometry exhibiting anomalous cones away from the points of highest symmetry. 42
3.10 Moving an anomalous cone to an arbitrary location in k-space. 42

4.1 3D-printing oligomodal metamaterials. 46
4.2 Textured compression revealing two independent soft modes. 47
4.3 Textured compression of a quasicrystalline oligomodal metamaterial 48
4.4 Mode selection by strain rate (An experiment by D. Dykstra). 49

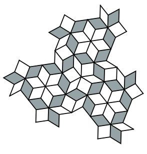

4.5 3D-printed nonlocally-resonant metamaterial. 50
4.6 Experimental setup of the laser vibrometry measurement. 51
4.7 Experimental isofrequency contours with two nonlocal resonances. 52

5.1 Anomalous cones as mass-gap to momentum-gap transition. 56
5.2 Emergence of momentum gaps in the counter-rotating squares metamaterial. . 59
5.3 Deformed local arrow rule that no longer leads to a global zero-mode. 60
5.4 Edge states from anomalous cones. 61
5.5 Spectra of pre-twisted isograph geometries 62
5.6 Probing the pre-twisting band gaps with FEM. 64

6.1 Quadratic spectral signature of a non-Bloch zero-mode in an elastic chain. . . . 66
6.2 Cubic spectral signature of a non-Bloch zero-mode in an elastic chain. 67
6.3 Quadratic spectral signature of a non-Bloch 2D zero-mode. 70

7.1 Nonlocal resonances in a weakly-coupled twisted elastic chain. 79
7.2 Nonlocal resonances in an interlaced 3D elastic metamaterial. 80

8.1 Ashby plot comparing nonlocally-resonant metamaterials with the state of the art. 89
8.2 Poincaré section of the distributed 2-DOF pendulum model. 92

B.1 Details of the inverse design method 97

C.1 Spectrum of a quasicrystalline oligomodal metamaterial with 32 × 32 cells. . . . 101

List of Tables

3.1 Effective range of negative refraction 40

7.1 Character table of the D_2 point group. 76
7.2 Character table of the O cubic point group. 83

1 Introduction

“Et si on les appelait méta-métamatériaux ? ”
— Moi
“Non”
— R. Fleury

The presence of *mesoscale structure* in many naturally-occurring materials heavily impacts their physical properties. In the first section, we [I] stress this point with several examples. This suggests introducing mesoscale structure in artificial materials as well [2], thus leading to the notion of *architected media* which we discuss in the second section. There, we center our discussion on wave properties, providing some historical context on the two main design paths to control waves in architected media, namely photonic crystals and locally-resonant metamaterials. In Sec.1.3, we sketch a third design strategy, based on nonlocal resonances. Finally, we present the structure and objectives of this thesis.

1.1 The role of mesoscale structure in natural materials

To a certain degree, the physical properties of an object are determined by its external shape and the atomic structure of the material composing it. For many materials, however, this is not the end of the story. For instance, the mechanical properties of metallic alloys are heavily impacted by structures at intermediate scales, which we will term the mesoscale structure of the material. Indeed, most alloys are far from forming perfect crystals; they are filled with various types of defects, dislocations and grain boundaries which modify their physical properties. As a concrete example, the toughness of an alloy is directly related with the average size of the crystalline grains through the Hall-Petch relationship [3, 4]. More generally, irreversible plastic deformations, with their slipping crystal planes and wandering defects, can be described in terms of dislocation dynamics [5].

[I] I will use the pronoun “we” in the remainder of the thesis, as a way to include you, the reader, in the discussion.

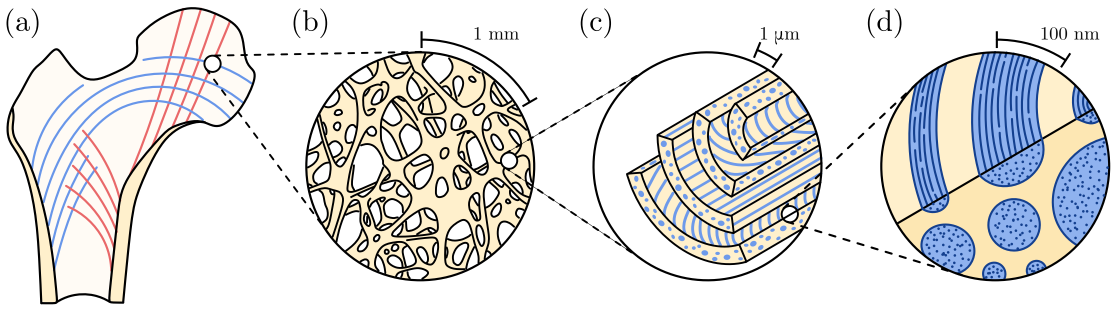

Figure 1.1: Hierarchy of mesoscale structure in natural materials. (a) Cross-section of a femur head, with the main tension-bearing lines depicted in blue and the main compression-bearing lines depicted in red. (b) Millimetric trabecular structure in the inner volume of the bone. (c) Micrometric inner structure of a single trabecula, consisting of anisotropic sheets stacked with varying orientation. (d) Nanometric structure of a single sheet, consisting of a composite of collagen fibers (blue) and a mineral matrix (yellow).

Mesoscale structure takes on an even more central role in determining the physical characteristics of living materials, which are actively reshaped by the forces of evolution to achieve functionality at a minimal cost. As an example, consider the intricate internal structure of bone, sketched in Fig.1.1. Several levels of organisation occur in the mesoscale range; slightly below the millimeter scale, we find an intricate scaffolding consisting of so-called trabeculae [6–8]. Going two orders of magnitude down in scale, it becomes apparent that each trabecula consists of many layers of oriented bone sheets [9]. One more level of organisation appears below the micrometer scale, revealing that each sheet is itself a composite of two materials, namely collagen fibers embedded in a mineral matrix [10]. Only below this level are the properties of the material directly determined by the type of atoms and their chemical bonds. Such hierarchies of mesoscale structures are recurrent in natural materials. They lend bone good mechanical properties in terms of fracture resistance and rigidity, for a low weight and minimal manufacturing constraints.

Since this thesis is not only concerned with mechanics but also with waves, our next example of mesoscale structure has to do with wave propagation. Consider the iridescent colours of peafowl feathers (Fig.1.2(a)). As already described by Hooke in his *Micrographia* (1665) [11], these colours are not related to pigmentation; they arise from an interference phenomenon. To understand it, let us dive down the hierarchical structure of peafowl feathers. The barb and barbule structures described in Fig.1.2(bc) have mechanical roles; we need to consider interactions of light with the next mesoscale substructure of the feather to understand its optical properties [12–14]. In Fig.1.2(d), we sketched the cross-section of a single barbule. The walls contain regular arrays of melanin rods, spaced by a few hundred nanometers. When light impinges on these rod structures, it is reflected at several depths. For light of appropriate wavelengths, this leads to a type of constructive interference known as Bragg interference.

Mathematically, it can be understood by noting that a ray of light reflected by a rod layer at depth L has to travel on a longer path than a ray reflected at the surface. In terms of the angle θ

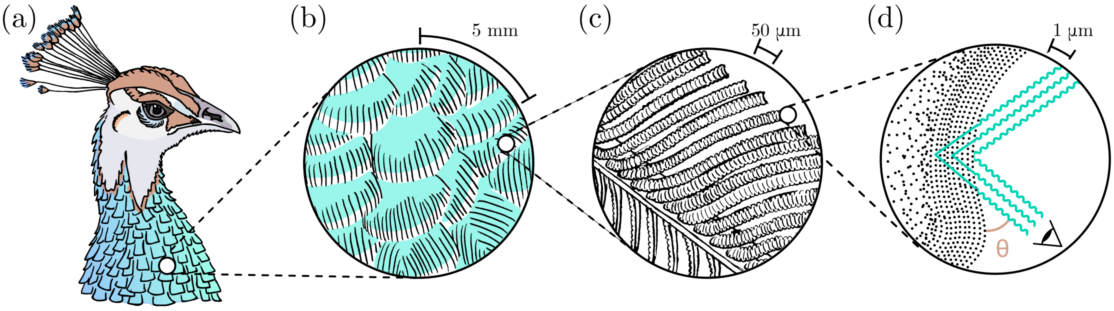

Figure 1.2: The mesoscale structure of peafowl feathers lends them their iridescent colour. (a) Sketch of a peahen head. (b) Sketch of the barb structures (black lines) in feathers. (c) Barbule substructure of a single barb. (d) Photonic crystal composed of melanin rods (black points) in the cross-section of a single barbule. The wavy lines indicate photons interfering constructively as they are reflected by layers at different depths. Rod layers are separated by a thickness L.

between the surface and the ray, this additional length is equal to $2L\sin(\theta)$. If the colour of the impinging light is such that an integer number of wavelengths fit in this added length, both rays interfere constructively. This selective reflection also explains the iridescent character of the feathers, because the length of the added path is angle-dependent. Different colours therefore dominate at different angles.

With these three examples from the natural world, we have seen that mesoscale structures can fundamentally alter material properties. Harnessing mesoscale structure in the design of artificial materials results in the concept of *architected media*. Early studies in that domain were mostly theoretical, given the crudity of the available manufacturing processes. While reaching the sophistication of the hierarchical self-assembly processes present in living tissues under ambient conditions remains a distant dream, the rise of additive manufacturing and other novel assembly techniques has unleashed vast possibilities in the realm of architected media.

1.2 Architected materials in wave physics

This section starts with a short historical perspective on architected wave media. We then discuss the underlying physical mechanisms in more detail using two toy models. Finally, we review the state of the art of elastic architected media and discuss the limitations of the two dominant approaches.

In Fig.1.3, we provide a limited selection of landmark architected media in wave physics. Two main flavours of architected media dominate wave physics: photonic crystals and locally-resonant metamaterials. Photonic crystals appeared first; their working principle essentially relies on Bragg interference, the very phenomenon on which structural color in peafowl feathers depends. Research on photonic crystals [15, 19–27] took off in 1987 with theoretical studies

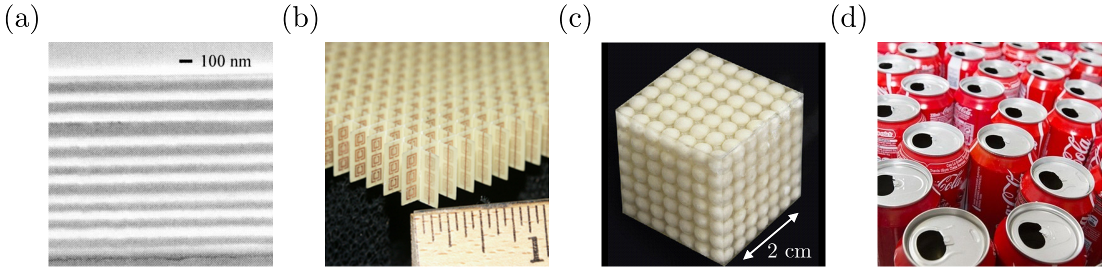

Figure 1.3: The rise of architected media in wave physics. (a) Omnidirectional dielectric mirror based on a photonic crystal. Adapted from [15]. (b) Doubly-negative electromagnetic metamaterial based on overlapping local electric and magnetic resonances. Adapted with permission from [16] (c) Elastic locally-resonant metamaterial based on spherical inclusions. From [17]. Reprinted with permission from AAAS. (d) Doubly-negative acoustic metamaterial based on soda cans. Adapted with permission from [18]

.

in electromagnetism and later blossomed experimentally, even reaching technologically relevant applications such as the perfect[II] dielectric mirror [28, 29] depicted in Fig.1.3(a). Their counterpart for elastic waves, phononic crystals, appeared later [30], opening new vistas in vibration control [31, 32]. This type of architected medium exhibits interesting physical properties, such as frequency bands in which wave propagation is forbidden (known as band-gaps) [33–37] and negative-index dispersion branches [38–44]. The main limitation of this approach is the bulkiness of the resulting structures, in which the lattice spacing must be of the order of the wavelength of interest to leverage Bragg interference. This is not a big issue in optics, but it can quickly become a limiting factor at larger wavelengths.

This bulkiness provided part of the motivation to develop a second design path for architected wave media. The second motivation was rooted in intriguing theoretical predictions by Lamb, Schuster and Veselago relating to negative-index media [45–47]. In particular, the latter predicted that media with simultaneously negative values for the electric permittivity and the magnetic permeability would lead to negative refraction, by making the effective refractive index n_{eff} negative. This intriguing notion, unobserved in natural materials, found a wide echo after Pendry pointed that it could be leveraged to produce lenses beating the diffraction limit [48, 49]. Using local resonances to effectively achieve negative properties within limited frequency bands, [50, 51] paved the way towards concrete mesoscale structures for doubly-negative media [52, 53]. One such structure is shown in Fig.1.3(b). Because their mesoscale structure consists of many individually resonant elements, these media are called *locally-resonant metamaterials* [54–59]. Again, elasticity followed electromagnetism with the elastic metamaterial of [60], depicted in Fig.1.3(c). Many other elastic metamaterials followed suit [17, 18, 61–96].

These developments also allowed the community to access the intervening regime of near-

---

[II] In the sense that it reflects at all angles and polarisations, without the losses associated to metallic mirrors.

zero effective properties, such as permittivity and density [97–100]. This extended palette of experimentally accessible refractive index values suggested an even more radical idea: in *transformation optics*, the index n_{eff} is tuned locally [101–108]. Using a change of variables based on conformal transformations[III] then allows one to translate back and forth between an effective-index metamaterial realisation and a deformed virtual space in which the index is constant. One can then leverage these deformed coordinates to cloak objects from impinging waves at particular frequencies. At optical wavelengths, this evokes invisibility cloaks, but nothing prevents us from considering much larger wavelengths. Pushing the relevant mesoscale structure well beyond the usual material scales, one can even envision structuring forests or cities to deflect seismic waves [109–111].

Local resonances provided a key to unlock this treasure trove of unusual wave phenomena, but frustratingly, they come with their own limitations. Indeed, to break free of the lattice-constant limitations that characterise photonic crystals, locally-resonant metamaterials have to pay a heavy price in the form of limited bandwidth. Such constraints, as well as related causality and nonlocality considerations, were studied in [112–115].

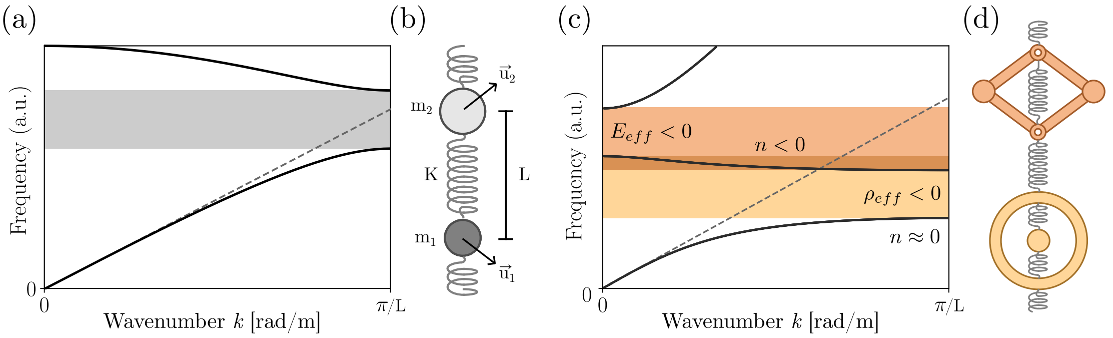

Figure 1.4: The two traditional pathways to wave control in architected materials. (a) Spectrum of a diatomic spring-mass chain, with a Bragg gap highlighted in grey and the sound cone indicated with a dashed line. (b) Geometry of the corresponding unit-cell. (c) Spectrum of a doubly-negative metamaterial, with the range of effective negative stiffness indicated in orange and the range of effective negative density indicated in yellow. The sound cone is indicated with a dashed line. (d) Metamaterial unit cell, with the mechanisms responsible for negative effective properties colour-coded accordingly.

To explain some of these limitations and tradeoffs with a minimal amount of technical detail, we introduce 1D models in Fig.1.4. We do so in the context of elasticity[IV], since this will be the physical setting of most of this thesis. First, we model phononic crystals with an infinite spring-mass chain, as shown in Fig.1.4(b). Consider the case in which the two masses in the unit cell are equal. The translation symmetry of the chain allows us to apply Bloch's theorem, thus relating the displacement at the nth mass in the chain to that of the mass at the origin with a simple phase: $u_n = e^{in\phi} u_0$. We can then compute the forces applying on the nth mass

---

[III] Conformal transformations are particularly convenient because they leave the wave equation invariant up to spatial variations in n_{eff}. In principle, one can also use more general transformations.

[IV] A field of research also pioneered by Hooke, incidentally.

using Hooke's law,

$$f_n = K(u_{n+1} - u_n) - K(u_n - u_{n-1}) = -2K\big[1 - \cos(\phi)\big]\, u_n, \tag{1.1}$$

where K denotes the stiffness of the springs. Inserting this in Newton's second law and looking for a solution at an angular frequency ω, we find

$$\omega(\phi) = \sqrt{2\frac{K}{m}\big[1 - \cos(\phi)\big]} = \sqrt{\frac{K}{m}}2\Big|\sin\Big(\frac{\phi}{2}\Big)\Big| \xrightarrow[\phi<<1]{} \sqrt{\frac{K}{m}}\phi. \tag{1.2}$$

Note that inter-cell phase from Bloch's theorem, ϕ, is often substituted by a Bloch wavenumber k, defined through $\phi = kL$. Equations of the type of Eq.(1.2), which relate the frequency and wavenumber of oscillatory modes, are called *dispersion relations*. In crystalline contexts, we will also use the term "band structure" interchangeably. In this simple example, we see that taking the long-wavelength limit (in which the intercell phase ϕ becomes small) leads to a linear dispersion relation, with elastic waves moving at a speed of $c_s = \sqrt{\frac{KL}{m/L}} = \sqrt{\frac{E}{\rho}}$. In this formula, Young's modulus $E = KL$ and the density $\rho = m/L$ respectively took over the roles of stiffness and mass. In the long-wavelength limit, we therefore recover the behaviour of continuum elasticity.

To model the interference phenomenon observed in the example of Fig.1.2, we now introduce regularly spaced imperfections in the chain, on which elastic waves will scatter and interfere. As shown in Fig.1.4(a), we achieve this by making every second cell slightly heavier. The resulting dispersion relation is drawn in Fig.1.4(a); for most k, this is simply a folded version of the relation obtained in Eq.(1.2). Something interesting occurs when the wavelength becomes commensurate with twice the lattice spacing: there, we see a frequency gap opening, in which waves can no longer propagate. This forbidden frequency range is called a Bragg gap; it results from the same interference phenomenon as the colour of peafowl feathers. Above this gap, a second band appears in addition to the usual acoustic dispersion band. This so-called optical branch exhibits negative group velocity, the very property that provided the initial impetus to the field of metamaterials. However, leveraging optical branch and Bragg gap properties requires rather bulky structures. Concretely, opening a Bragg gap at a frequency f requires unit-cells of a size $\sqrt{E/\rho}/(2f)$. This class of architected media, whose functionality relies on the phenomenon of Bragg interference, are called photonic or phononic crystals, depending on the nature of the waves involved.

Turning our attention to locally-resonant metamaterials, we consider a chain with two types of internal resonances, drawn in Fig.1.4(d). In the context of elasticity, the need for effectively negative permittivity and permeability is replaced by the need for negative density and stiffness. Each of the contraptions [61, 96, 116] depicted in Fig.1.4(d) induces one of these effective properties over a certain frequency range: the internal mass (yellow) induces negative density, whereas the lateral-inertia mechanism (orange) induces negative stiffness.

Since the speed of sound is given by $c_s = \sqrt{\frac{E}{\rho}}$, when either of these properties is negative, c_s becomes imaginary. The corresponding ranges of frequencies are called band-gaps. At these frequencies, waves cannot propagate and are replaced by evanescent modes. In the dispersion relation of the metamaterial chain, shown in Fig.1.4(c), we highlight these gaps in orange and yellow. A complementary way to interpret these gaps is to consider them as polariton hybridization gaps. A series of decoupled local resonances would be associated to a flat band at a particular resonance frequency, since any k-vector could be realized by selecting an appropriate initial phase in every resonator. As we couple them together, this flat band hybridises with the dispersion of a spring-mass chain, thereby opening locally-resonant gaps.

Things become really interesting if we manage to tailor the internal structure of these two mechanisms such that the two negative-property gaps overlap. This gives rise to a doubly-negative dispersion branch, shown in Fig.1.4(c), in which waves are again allowed to propagate. The twist is that group velocity in this low-frequency branch is negative, leading to all sorts of interesting properties such as negative refraction and subwavelength imaging. Locally-resonant band gaps and doubly-negative bands are no longer constrained by the lattice constant of the material, which leads to the notion of subwavelength wave control. As mentioned earlier, these properties are narrowband by design, since they are obtained by hybridising a standard elastic band with local resonances. For certain applications, this is a serious limitation.

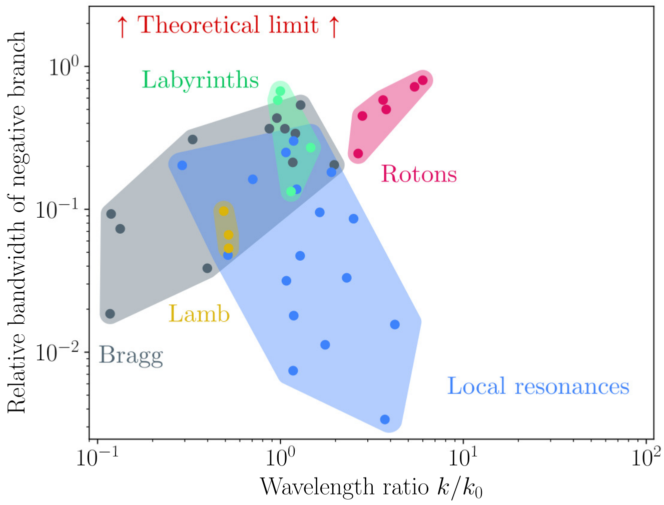

Figure 1.5: Negative index bandwidth versus subwavelength ratio k/k_0 for various elastic architected media. The data points are grouped in five families: phononic crystals (grey), labyrinthine crystals (green), Lamb waves (yellow), locally-resonant metamaterials (blue) and roton metamaterials (pink). The upper edge of the plot corresponds to the theoretical maximum of relative bandwidth, namely $\Delta\omega/\omega_c = 2$.

In Fig.1.5, we illustrate this broadband-subwavelength tradeoff by compiling several elastic negative refraction studies involving phononic crystals [38–43, 71, 73, 79, 80, 85, 94] and elastic metamaterials [44, 62, 63, 65, 68, 70, 72–78, 81, 84, 89]. We classify the studies into one group or the other on the basis of their self-identification. We also included three related sub-types of architected media in the diagram. First, we considered labyrinthine metamaterials [117–121], in which waves are controlled by delaying them through intricate coiled paths. The second category leverages points with zero group-velocity that can be found in the higher-frequency Lamb waves [122–126].

As for the third category, it consists in a very recent variety of elastic metamaterials, known as roton metamaterials [127–135]. In roton metamaterials, beyond-next-neighbour couplings are introduced, leading to the introduction of a negative-index region in the first branch of the spectrum. In practice, these couplings take the form of explicit elastic connectors or long-range radiative interactions. The associated local minimum, by analogy with the dispersion relations observed in superfluids [136–140], is called a roton minimum. After Ch.5 and Ch.7, we will be able to articulate the connections between roton metamaterials and the concept of nonlocal resonance, which we will introduce in the next section and develop in the remainder of this thesis. For now, we simply note that a certain degree of nonlocality lies at the heart of the roton approach, in the form of long-range couplings.

In Fig.1.5, we measure the subwavelength character of the material with the ratio $k/k_0 = k/(\omega_1/c_s)$. In this ratio, ω_1 and k are respectively the frequency and wavenumber of the negative branch's lowest point, while c_s denotes the speed of sound obtained in the long-wavelength limit. This ratio compares the actual wavelength with a reference wavelength predicted by using the linear dispersion of the continuum limit. In the presence of certain mesoscale structures, like the locally-resonant inclusions of metamaterials, this reference wavelength may be several times larger than the actual wavelength. As for the ordinate axis, it represents the relative bandwidth $\frac{\Delta\omega}{\omega_c} := \frac{\omega_2-\omega_1}{(\omega_2+\omega_1)/2}$, where ω_2 is the highest frequency in the negative-index band.

Interestingly, phononic crystals, labyrinthine phononic crystals, Lamb waves and locally-resonant metamaterials form a single continuous cluster on this diagram, with no clear-cut distinction. A continuous landscape of hybrid architected media exists. We also observe that the high values of subwavelength ratio associated to locally-resonant metamaterials lead to a quickly decreasing bandwidth, in line with the qualitative arguments we developed above. With their nonlocal couplings, roton metamaterials escape this tendency, being simultaneously more subwavelength and broadband than traditional concepts. In the papers that form the core of this thesis [141, 142], we followed a distinct, parallel path to escape the constraints of traditional architected media. We present this path in the next section.

1.3 An alternative design path: nonlocal resonance

In electromagnetism, an intriguing class of architected media [143–148] avoids the limitations of traditional architected media. These so-called *interlaced wire media* (IWMs) rely on a

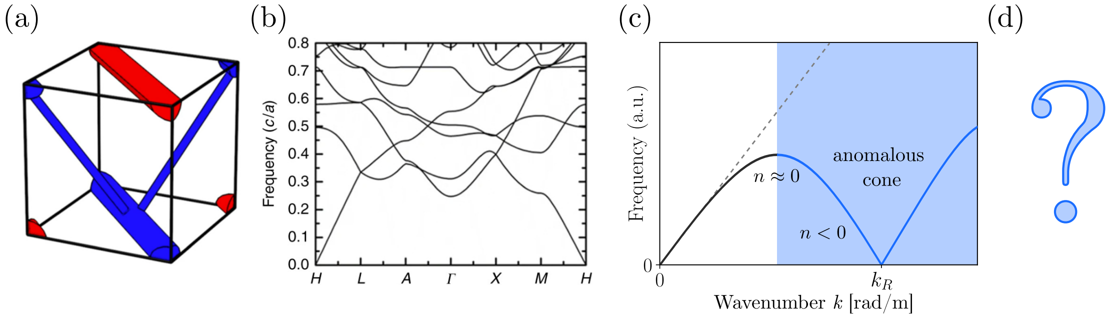

Figure 1.6: The quest for an elastic counterpart to interlaced wire media? (a) Unit-cell of the original interlaced wire medium, with the coloured volumes depicting conductors. The colours themselves indicate the two different electric potentials on these conductors. (b) Associated electromagnetic band structure. Panels (ab) are adapted with permission from [143]. (c) Hypothetical elastic equivalent, also exhibiting an anomalous cone (highlighted in blue), centered at a nonzero wavevector k_R. (d) Mysterious elastic micro-structure associated to the anomalous cone property, to be introduced later.

completely different physical principle. In Fig.1.6(ab), we reproduce the geometry and band structure from [143]. The presence of a wide, low-frequency domain of negative group velocity is manifest in Fig.1.6(b). The underlying design principle of such structures is the following: as shown in Fig.1.6(a), the medium consists of disconnected conducting components. In the more standard case, there would be one distinct component for every unit cell, with no global connectivity. In that case, we would be in the presence of a traditional wire medium, which could act as a locally-resonant metamaterial or a photonic crystal depending on the involved geometry and materials. In another well-known limit, a single, fully-connected giant component acts as a Faraday cage and therefore prevents the propagation of electromagnetic waves below a cutoff frequency determined by the lattice constant.

IWMs provide a strange intermediate situation: they consist in a finite number of disconnected giant components[V] (GCs), which does not scale with the number of cells in the system. Since they are disconnected, GCs can carry different static electric potentials. These nontrivial potential distributions can be interpreted as electromagnetic zero-frequency modes (zero-modes in short). Because the spectrum is continuous, other low-frequency modes emerge to connect the zero-modes to the higher-frequency branches of the spectrum. Then comes the literal twist: consider the case in which the GCs are *interlaced*, meaning that their positions within the unit cell are permuted upon translation by a lattice vector. In this situation, the positions of the zero-frequency electric potentials are also exchanged. This, in turn, implies that the zero-mode is associated to a nonzero wavevector! The band that emerges from this zero-mode therefore exhibits negative group velocity, one of the hallmark properties of doubly-negative metamaterials.

[V] We use the name "giant component" in reference to the well-established concept carrying the same name in graph theory. In both cases, the word "giant" means that a macroscopic fraction of the material or graph must belong to the giant component.

To clarify this intriguing concept and to generalise it beyond electromagnetism, we seek to extract its essential abstract ingredients. What is really needed to achieve the above behaviour in a wave system ? An intensive number of zero-frequency modes with nontrivial, periodic spatial patterns. In order to contrast them with the dominant concept of locally-resonant metamaterials, we will call these delocalised zero-modes *nonlocal resonances*. In this thesis, we seek to define a new class of architected media by generalising the abstract concept that underlies IWMs to a completely different physical setting[VI]. We will then leverage this platform to explore the peculiar physics associated to nonlocal resonances.

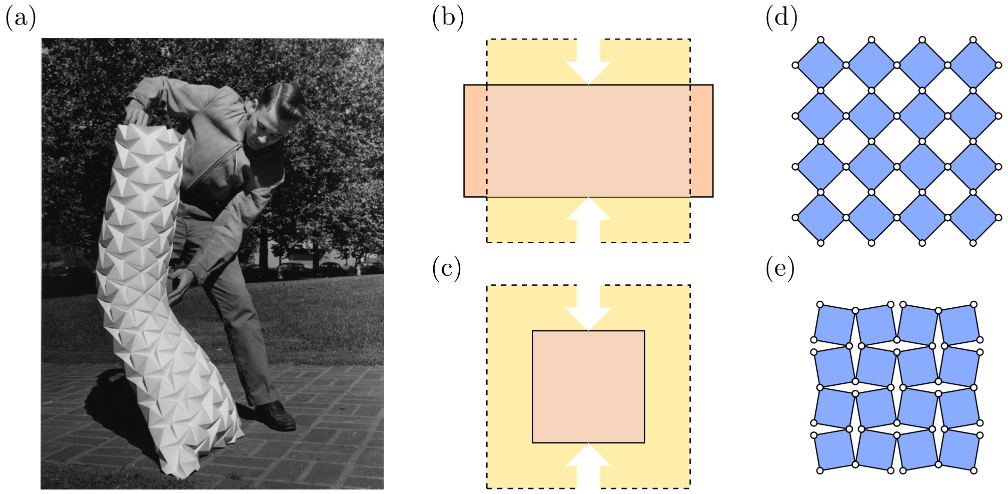

Figure 1.7: Another historical strand: flexible metamaterials. (a) Ron Resch with a flexible periodic origami (1960). (bc) Transverse deformation of compressed elastic materials (orange domains) with the undeformed domains in yellow and white arrows indicating the compression direction. The material in (b) has $\nu = 0.5$, while the material in (c) has $\nu = -1$, namely the theoretical lower bound for Poisson's ratio in an isotropic material. (d) The counter-rotating squares structure, with blue areas denoting rigid elements and white disks denoting hinges. (e) Actuated counter-rotating squares mechanism.

To provide a clean break from IWMs, we change the physical setting in two ways: we hop down from three to two dimensions and replace electromagnetism by elasticity. Note that this forbids any direct translation from the IWM design method: indeed, three spatial dimensions are required for interlacing. In this new setting, we seek an architected medium whose phononic spectrum exhibits anomalous dispersion cones, as depicted in Fig.1.6(c).

In other words, we are looking for a 2D elastic medium that hosts regular, zero-frequency deformation modes with nontrivial periodicity. This requirement resonates with another class of architected media, namely flexible metamaterials. In the previous section, we focused on wave metamaterials; flexible metamaterials belong to a different tradition centered around static or quasistatic mechanical properties. These materials could broadly be characterised

---

[VI] We do so in order to remove accidental properties of IWMs that may not be immediately related to their nonlocally-resonant character.

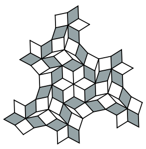

as artificial media that rely on folding motions and elementary mechanisms to achieve unexpected mechanical properties [141, 142, 149–160]. Flexible metamaterials also have a long and varied history; a potential starting point lies in the 1950s. This root starts with an artist, Ron Resch, pictured in Fig.1.7(a) with one of his periodic flexible origami. Resch explored many such flexible geometric structures, in two and three dimensions, predating their re-invention in physics sometimes by decades.

A more conventional starting point could be the introduction of auxetic materials by Roderic Lakes [161]. The defining feature of auxetic materials [162–165] is their negative Poisson's ratio, an adimensional number that measures the amount of lateral extension in medium upon compression. In standard elastic media, Poisson's ratio lies in the $\nu \in [0, 0.5]$ range; this corresponds to the positive lateral extension depicted in Fig.1.7(b). Auxetic materials, on the other hand, behave as shown in Fig.1.7(c): they lose volume as we compress them. Such behaviour typically relies on a complex inner structure, with empty pores closing as the material is compressed. The archetypal auxetic geometry, originally introduced in mineralogy [166–168] to model displacive phase transitions in perovskites, is depicted in Fig.1.7(d). It was later claimed by the auxetic community because of its extreme Poisson's ratio of $\nu = -1$; the underlying mechanism is depicted in Fig.1.7(e). Because of the relative rotation of the rigid squares that constitute the material, this structure is called the counter-rotating squares geometry.

These developments also connected with a tradition of continuum elasticity theories. Graeme Milton, for instance, investigated various extreme corners of the parameter space of elastic moduli [169–171] and introduced the notion of pentamode material [172, 173]. More unusual elasticity theories were also put to contribution, such as the elasticity theory of the Cosserat brothers [174–176] or micropolar theory [127, 177–179]. In these theories, local rotational degrees of freedom are taken into account; this is a necessary ingredient to properly homogeneise some types of flexible metamaterials.

Auxeticity then trickled towards fine-grained deformation control, naturally leading to the design of more complex shape-morphing behaviours [180–188]. Combinatorial methods [141, 189–194] provide powerful tools to design such shape-morphing structures. To cite two other developments, hierarchies of mesoscale structures were introduced in flexible metamaterials [2, 195–198], and various avatars of topology were uncovered [199–204]. Here, we only hastily summarised the zoology of flexible metamaterials; it is as flourishing as in the wave context of the previous section.

Let us stop our journey through the literature here to take a good look at the horizon and summarise our objectives. Motivated by the limitations of phononic crystals and locally-resonant metamaterials, but also by the extraordinary properties they manage to achieve within these confines, we seek a new class of wave material architectures. The initial impetus was given when we realised that the trailblazing shifted cones of IWMs only required a zero-mode with nonzero-wavevector, which we knew where to find within the realm of planar

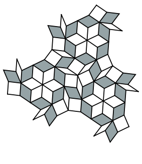

elasticity.

This entry point was the counter-rotating squares mechanism. Indeed, in the idealised limit of Fig.1.7(de), the counter-rotating squares metamaterial folds as an ideal mechanism. If the hinges bend for a negligible energetic cost, this mode effectively constitutes an elastic zero-mode. Examples of such mechanism-based zero-modes abound in flexible metamaterials. However, most of them are part of extensively-scaling families of zero-modes; the metamaterials that host them are very floppy, like the flexible origami surface held by Resch in Fig.1.7(a). The counter-rotating squares geometry is different: it only has a single, global degree of freedom. Furthermore, this zero-mode is nontrivially periodic: the deformations in neighbouring unit cells are exactly opposite, picking up a phase of π.

The counter-rotating squares mode fits all the requirements of a nonlocal resonance. Therefore, the first thing we will do is to try generalising the principles that underlie this deformation mode. In Ch.2, we introduce a graphical design method to systematically create geometries hosting such zero-modes. In particular, this method allows us to design structures that host a finite number of zero-modes, providing a path to multifunctional flexible metamaterials. We call such geometries *oligomodal.* We then adopt a wave viewpoint in Ch.3, in which we confirm that these zero-modes induce anomalous dispersion cones and explore the associated consequences on wave propagation. Ch.4 is dedicated to experimental validation, with experiments on 3D-printed samples demonstrating oligomodality, multifunctional mechanics and above all a nonlocally-resonant vibration spectrum. In Ch.5, we take a deeper dive in the various ways in which gaps arise in nonlocally-resonant metamaterials. The core of the research presented in Chapters 2 to 4, as well as part of Ch.5, was reported in Refs.[141] and [142]. Here, we reworked this material in depth, by streamlining our methods and finding new interconnections.

In Ch.5, we also briefly touch upon aspects of non-hermitian time evolution, the subject of a covid side project described in Ref.[205]. We did not fully include it in the thesis for the sake of thematic unity. As for Chapters 6 and 7, they consist in entirely new material, which may form the basis of future articles. Ch.6 is dedicated to the motley crew of zero-modes arising in oligomodal metamaterials that do not take the form of a Bloch wave, thus allowing them to escape the preceding analysis. Finally, we move on to 3D elasticity in Ch.7; we leverage this platform to investigate the interplay of nonlocal resonances with symmetries.

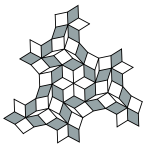

2 Kinematic Graphs

"The stuff with arrows is not clear."
— An honest referee

In the introduction, we saw that the classical flexible metamaterial based on the counter-rotating squares mechanism seemed to host a single zero-mode meeting the criteria of a nonlocal resonance. In the present chapter, we place this isolated example in a wider conceptual context and develop tools to design planar mechanisms with similar kinematics. In particular, we will introduce mechanical tilings that host several nonlocal resonances simultaneously. To that end, we introduce a graph-based method to design flexible metamaterials with various numbers of zero-energy modes. As a starting point to introduce our method, we note that zero-modes cannot involve changes in elastic energy, because the resulting restoring forces would ultimately lead to finite-frequency oscillations.

This consideration motivates us to model our flexible material as a mechanical linkage, i.e. as a collection of infinitely rigid bars connected by friction-less hinges. In Fig.2.1(a), we give an example of an amorphous planar linkage, with no particular symmetry. Our goal is to design linkages with interesting deformation modes, which we will later promote to zero-energy modes of a mechanical metamaterial. We will treat these dynamical aspects from Ch.3 onward, progressively replacing ideal linkages with spring-mass models and then realistic 3D-printable geometries. In this chapter, however, we start by focusing on the purely kinematic aspects of the problem.

In general, this is a difficult problem, involving strong geometric nonlinearities and compatibility conditions between the deformations of neighbouring regions. We tackle it step by step, starting by counting degrees of freedom (henceforth DOFs) and highlighting relevant substructures in the mechanical network. After hinges and bars themselves, the most basic conceptual units are triangles, such as the one shown in Fig.2.1(b). A rigid triangle in two dimensions can move in three ways: we can translate it in two independent directions and rigidly rotate it. Actually, all linkages exhibit these three DOFs, even the whole mechanical

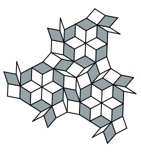

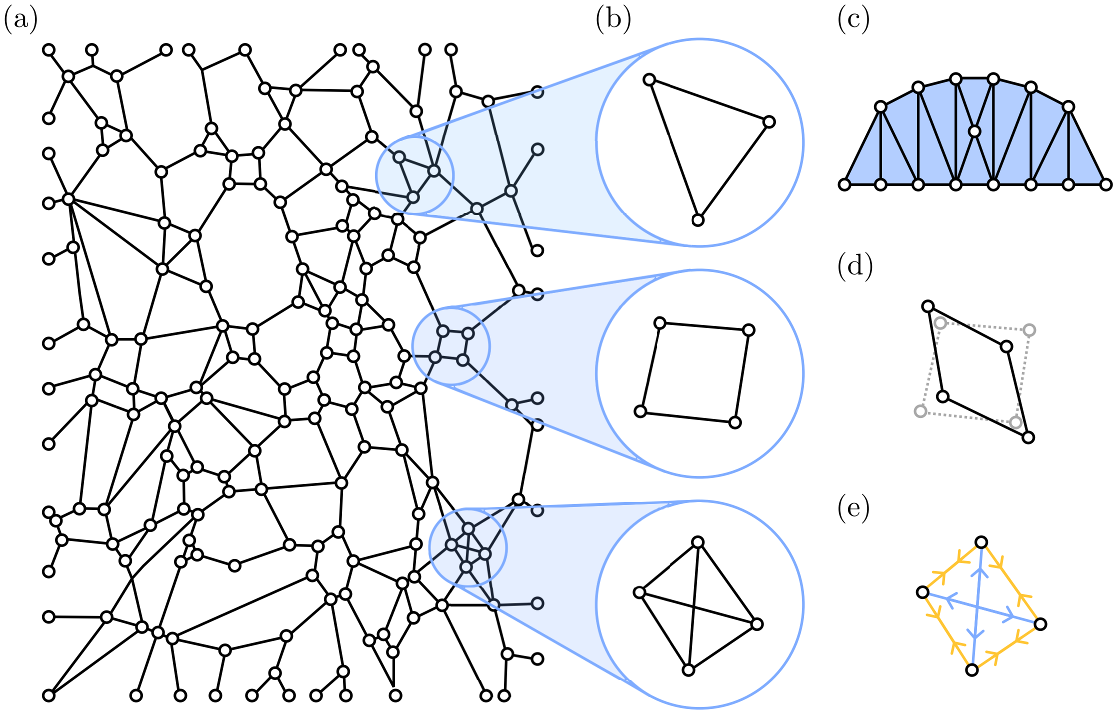

Figure 2.1: Kinematic degrees of freedom in a truss-hinge network. (a) aperiodic metamaterial, with perfect hinges depicted as white disks and rigid bars depicted as black lines. (b) Close-ups on interesting substructures of the mechanical network, providing examples of: (c) the rigidity of triangles, highlighted in blue, (d) the single degree of freedom associated with four-bar mechanisms, and (e) the states of self-stress associated with redundant constraints. In (e), tensile and compressive stresses are represented in blue and yellow, respectively.

network. What distinguishes triangles, and rigid bodies in general, is that they only have these three degrees of freedom. We can formalise this observation as follows: each hinge of the triangle can move in two independent directions, yielding a total of six DOFs, while each bar adds a single constraint, reducing the total to three DOFs. These are precisely the three aforementioned DOFs. Truss networks that consist exclusively of such triangles, such as the one depicted in Fig.2.1(c), are *statically determinate*; they do not exhibit internal degrees of freedom. In the remainder of the thesis, we will draw such rigid domains as coloured areas instead of triangulated trusses.

Things get more interesting as we move on to the second close-up of Fig.2.1(b), which depicts a four-bar linkage. We can count the degrees of freedom again: the hinges contribute eight DOFs in total. On the other hand, each rigid bar provides a constraint on the allowed motions, yielding four constraints. We are therefore left with four zero-modes: two independent translations, a rotation and, most interestingly, a nontrivial folding mechanism, depicted in Fig.2.1(d). This observation could encourage us, following Maxwell's footsteps [206], to introduce the following count:

$$N_m + 3 = 2N - c, \tag{2.1}$$

where N_m is the number of internal degrees of freedom, N the number of hinges and c the number of constraints. As an example, adding a diagonal bar in the linkage raises the value of c to five, yielding $N_m = 0$. We fall back to a triangulated truss, as in Fig.2.1(c), in which only global rigid motions are allowed. Adding a bar on the remaining diagonal means trouble for Eq.(2.1). Indeed, this makes the system over-determined and introduces a so-called state of self-stress. Such a state is depicted in Fig.2.1(e); it exhibits a nontrivial stress distribution on the bars, but the forces on the hinges sum to zero. Calladine [207] improved Maxwell's criterion to account for this subtlety,

$$N_m - N_{ss} + 3 = 2N - c. \tag{2.2}$$

The term N_{ss} is the number of states of self-stress, which correspond to redundant constraints. The presence of such states means that we cannot simply add degrees of freedom and subtract bar constraints. The spatial location of constraints matters. In particular, this implies that two metamaterials with the same number of hinges and bars do not necessarily host the same number of zero-modes. In other words, local mechanisms can be incompatible; the resulting mechanical frustration then prevents global deformations of the metamaterial.

A second difficulty lies in the highly nonlinear nature of linkage kinematics: in Fig.2.2(a), we follow the motion of a simple four-bar mechanism by tracing the path followed by the middle point of a bar. The resulting trajectory, drawn in red, is highly nontrivial. Keeping track of such kinematics for every single local DOF in the truss is a daunting task. Luckily, since we will ultimately be concerned with small-scale deformations and linear waves in metamaterials, we can use a simplifying assumption: motions will be restricted to slight deviations from the initial configuration of the mechanism. This will also allow us to represent local DOFs as directed graphs, which has the added advantage of simplifying the mechanical frustration issue: the problem becomes a combinatorial search of compatible local deformations.

2.1 Taming local mechanisms with the area law

To that end, we start by replacing each bar in the linkage with a complex number z_k, as shown in Fig.2.2(b). The argument and modulus of z_k respectively encode the angle and length of the bar. We then seek to describe small variations α_k of the internal angles $\tilde{\phi}_k = \phi_k + \alpha_k$, under the condition that the linkage remains closed. This will allow us to abstract the mechanisms as directed graphs of the type represented in Fig.2.2(c), where each hinge is represented as a white disk, henceforth known as a hinge node. As for the central black disk, it represents a

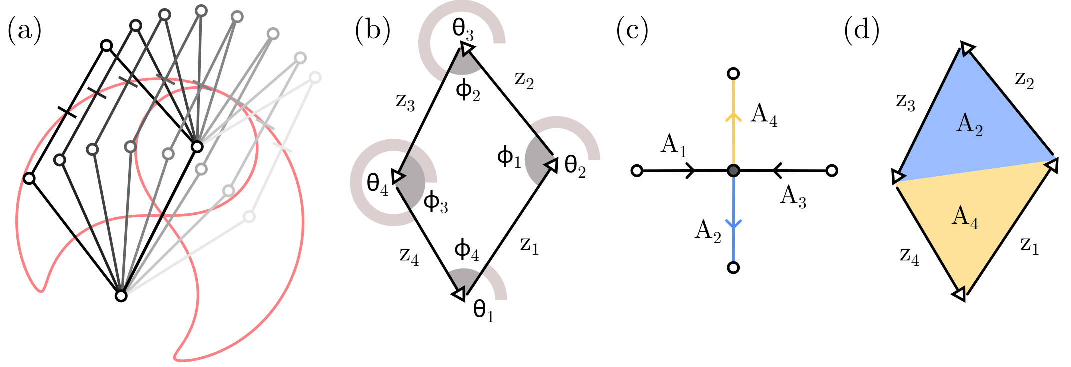

Figure 2.2: Linearising the kinematics of a four-bar mechanism. (a) Tracing the trajectory of the middle point of a bar in a single-DOF mechanism to visualise nonlinear kinematics. (b) Reference configuration around which we linearise the mechanism. (c) Equivalent directed-graph representation of the linear kinematics. (d) Area law for the arrow weights in the vertex representation, with colours corresponding to arrows in panel (c).

kinematic node; it encodes the relationship between the α_k. Positive α_k are represented as arrows going from the hinge node to the kinematic node, whereas negative α_k are represented with arrows going in the opposite direction. As a useful mnemonic for this convention, we note that the arrows point in the directions in which one should push to actuate the mechanism. The lengths of the bars and the initial configuration only play a role in determining the relative weights of the arrows, which we will now compute. Marking all deformed quantities with a tilde, the closure condition can be written as $\sum_{k=1}^{n} \tilde{z}_k = 0$, which in turn implies

$$\begin{aligned} 0 = \sum_{k=1}^{n} \tilde{z}_k = \sum_{k=1}^{n} |\tilde{z}_k| e^{i\tilde{\theta}_k} = \sum_{k=1}^{n} |z_k| e^{i(\tilde{\theta}_1 + (k-1)\pi - \sum_{j=1}^{k-1} \tilde{\phi}_j)} = \sum_{k=1}^{n} |z_k| e^{i(\theta_1 + (k-1)\pi - \sum_{j=1}^{k-1} \phi_j - \sum_{j=1}^{k-1} \alpha_j)} \\ = \sum_{k=1}^{n} z_k e^{-i \sum_{j=1}^{k-1} \alpha_j} \approx \sum_{k=1}^{n} z_k (1 - i \sum_{j=1}^{k-1} \alpha_j) = -i \sum_{k=1}^{n} \sum_{j=1}^{k-1} z_k \alpha_j. \end{aligned} \tag{2.3}$$

In the last step, we used the fact that the initial configuration is also closed. Choosing $n = 4$ and defining the infinitesimal-angle vectors $\vec{\alpha} := (\alpha_1, \alpha_2, \alpha_3, \alpha_4)^T$ yields the matrix equation

$$\begin{pmatrix} 1 & 1 & 1 & 1 \\ \mathrm{Re}(z_4 + z_3 + z_2) & \mathrm{Re}(z_4 + z_3) & \mathrm{Re}(z_4) & 0 \\ \mathrm{Im}(z_4 + z_3 + z_2) & \mathrm{Im}(z_4 + z_3) & \mathrm{Im}(z_4) & 0 \end{pmatrix} \vec{\alpha} = 0, \tag{2.4}$$

in which we also used the constraint $\sum_{k=1}^{n} \alpha_k = 0$, which reflects the fact that the sum of angles in a polygon only depends on the number of its sides. Applying row reduction, we find the

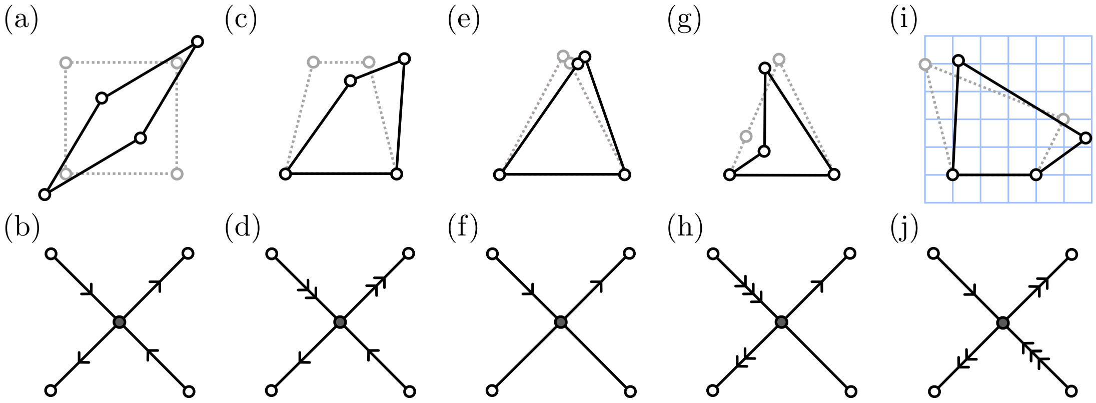

Figure 2.3: Some examples of arrow rules. Four-bar mechanisms are depicted on the top row. Hinges are depicted as white dots, while bars are represented by grey dashed lines when in the reference configuration and solid black lines when in the deformed configuration. The corresponding arrow rules are depicted on the bottom row, again with hinge vertices as white dots and with kinematic vertices as black dots. The cases considered are (a) four bars of equal length, (c) two opposing bars that are parallel and of unequal length, (e) the limiting case of a triangular frame, (g) three co-linear hinges and finally (i) a more generic mechanism with hinges sitting on a square grid.

kernel of this matrix, namely

$$\vec{\alpha} = \begin{pmatrix} \alpha_1 \\ \alpha_2 \\ \alpha_3 \\ \alpha_4 \end{pmatrix} = \epsilon \begin{pmatrix} z_3 \times z_4 \\ z_4 \times (z_2 + z_3) \\ z_2 \times (z_3 + z_4) \\ z_3 \times z_2 \end{pmatrix} = \epsilon \begin{pmatrix} z_3 \times z_4 \\ -z_4 \times (z_4 + z_1) \\ -z_2 \times (z_2 + z_1) \\ z_3 \times z_2 \end{pmatrix} = \epsilon \begin{pmatrix} z_3 \times z_4 \\ -z_4 \times z_1 \\ z_1 \times z_2 \\ -z_2 \times z_3 \end{pmatrix} =: \epsilon \begin{pmatrix} +A_3 \\ -A_4 \\ +A_1 \\ -A_2 \end{pmatrix}, \tag{2.5}$$

where $\epsilon \in \mathbb{R}$ is a small parameter[I]. This formula has a nice geometric interpretation: for an infinitesimal deformation of a four-bar mechanism, the small angular variation α_k at a given hinge is directly proportional to the area spanned by the two bars attached at the opposing corner, A_{k+2}, as highlighted in Fig.2.2(cd). We will call this the *area law*. The sign of the angular deformation is always opposite for neighbouring corners.

2.1.1 Kinematic graphs of four-bar linkages

This graphical representation is best understood by going through various examples and limiting cases; as a start, consider the case of a mechanism with bars of equal length, such as the one shown in Fig.2.3(a). Taking the square as our initial configuration, we see that all the internal triangles have the same area, hence yielding equal arrow weights. We can therefore abstract the deformation of Fig.2.3(a) as the directed graph of Fig.2.3(b). Interestingly, the high

---

[I] As for the cross products, they are defined as $w \times z := [\mathrm{Re}(w)\,\mathrm{Im}(z) - \mathrm{Re}(z)\,\mathrm{Im}(w)]/2$.

symmetry of this linkage means that the triangles retain equal areas even at large deformations, meaning that the graph description remains valid in the nonlinear regime.

In Fig.2.3(c), we consider a slightly less symmetric case, namely that of a trapezoidal mechanism. Using Cavalier's rule to determine the relative areas of the internal triangles, we obtain the directed graph of Fig.2.3(d). The hinges with obtuse angles are subject to larger angular deformations, with a factor determined by the ratio of the opposing parallel bars of the trapezoidal mechanism, here equal to two. Note that we use the convenient convention of representing the arrow weight through the number of depicted arrows.

Pushing the arrow ratio further, we get to the limiting case of a triangular truss, shown in Fig.2.3(e) in which we expect very little to happen. Indeed, the directed graph in this case tends to the limit of Fig.2.3(f), in which the bottom hinges feel no deformation whatsoever, since the opposing triangles have a vanishing area. As for the top hinges, they can still experience relative motion, but they are so close to each other that it hardly matters. Moving forward, we consider another special case, in which one of the triangles also has vanishing area, but this time because the linkage of Fig.2.3(g) has three aligned hinges. Since we set the central hinge in this alignment at one third of the total distance, we again get convenient integer arrow weights, which we represent with multiple arrows in Fig.2.3(h).

The convenience of this representation leads us to ask the following question: when can the arrow weights be represented by integers ? The answer, proven in Appendix A, is that this is the case if and only if the hinges can be made to sit on the nodes of a Bravais lattice. This makes it particularly convenient to draw potential unit cells on graph paper; determining the arrow weights then boils down to counting squares on the grid to determine the areas of the relevant triangles. For instance, consider the quadrilateral in Fig.2.3(i), which exhibits no particular symmetry besides the lattice condition we evoked. Its directed graph representation, shown in Fig.2.3(j), indeed only involves integer weights.

2.1.2 Combining elementary kinematic graphs

Inspecting the amorphous mechanical network of Fig.2.1(a), we notice that our restriction to four-bar linkages is a rather strong one. Large cyclic linkages could be involved in mechanism-based metamaterials. We now explain how to decompose the possible deformations of an arbitrary cyclic linkage into single degrees of freedom. By cyclic linkage, we mean a planar mechanism in which the bars and hinges form the sides and corners of a polygon. Applying the mode count of Eq.(2.2) yields $N_m = 2N - N - 3 = N - 3$. In the case of the heptagon drawn in Fig.2.4(a), we therefore expect to be able to decompose general deformations - such as the one of Fig.2.4(b) - into four DOFs. In order to extract these DOFs, we only actuate four hinges at a time, allowing us to use the area law on an equivalent quadrilateral linkage. In Fig.2.4(c), we always leave the three top hinges free to move, while fixing three of the bottom hinges. The free bottom hinge is indicated with a blue line. Measuring the areas of the inner triangles in these equivalent linkages, we obtain the arrow rules of Fig.2.4(d), in which we coloured some

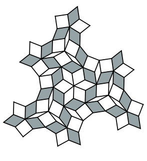

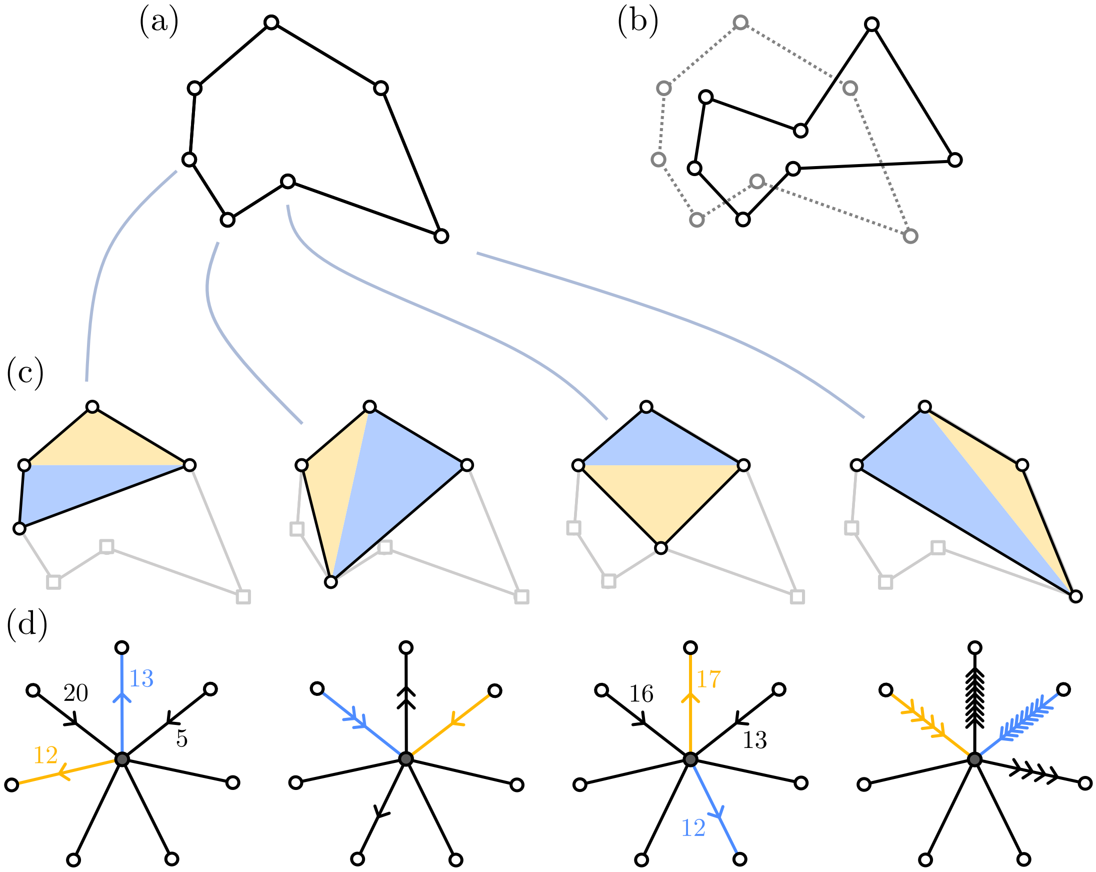

Figure 2.4: Decomposing the kinematics of an arbitrary cyclic linkage into combinatorial degrees of freedom. (a) Cyclic linkage with seven hinges in a reference configuration. (b) Generic deformation of the linkage. (c) Equivalent single-DOF mechanisms obtained by fixing three hinges, represented as grey squares. The areas relevant to compute arrow weights are coloured in yellow and blue. (d) Corresponding graph representations, with the edges corresponding to the above areas coloured accordingly.

of the edges to indicate their correspondance with an inner triangle. By construction, three of the bottom edges carry no arrow. Because we secretly drew the mechanism on a lattice, the arrow weights are again integers. General deformations can then be obtained as linear combination of these four arrow configurations.

To practice a bit before studying full-blown mechanical tilings, we study the kinematics of a composite mechanism involving several cyclic linkages, shown in Fig.2.5(a). To do so, we need a way to combine local graphs together. This is easily achieved by concatenating the graphs of neighbouring linkages at their shared hinges. We then introduce a small angular deformation at the top hinge of our composite mechanism, represented as an orange arrow in Fig.2.5(d). In Fig.2.5(e-j), we propagate the deformation on the graph through the arrow rules at kinematic nodes and hinges nodes. The arrow rule at hinge nodes is much simpler than at kinematic nodes: the only constraint is that the number of incoming and outgoing

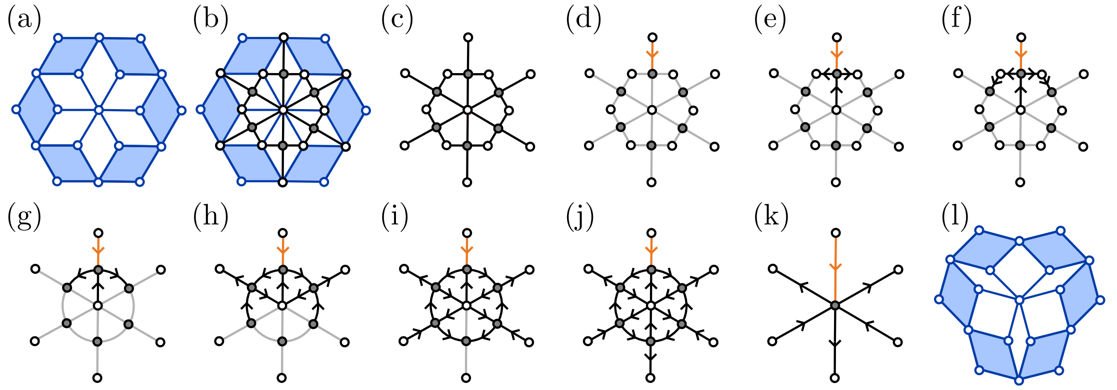

Figure 2.5: Simplifying the kinematics of a composite unit cell to an equivalent vertex. (a) Unit cell in its undeformed state, with hinges as white disks and rigid parts in solid blue. (b) Superimposed graph in solid black, with hinge vertices in white and kinematic vertices in black. (c) The same graph by itself. (d) Fixing an incoming arrow on the top edge, depicted in orange. (e) Three further edges are determined by a kinematic vertex. (f) Hinge vertices with two edges are determined by arrow conservation and can be erased, as done in (g). (hi) Propagating the arrows further along kinematic edges, until all edges are fixed in a self-consistent manner (j). (k) Simplifying the vertex representation to a single kinematic vertex with six edges. (l) Real-space representation of the mechanism.

arrows must be equal. We will refer to this rule as *arrow conservation*. Because the sum of internal angles in a polygon is invariant under mechanical deformations, we note that arrow conservation is also valid at kinematic vertices.

This is highly reminiscent of the ice rule invoked in the vertex models of statistical physics, which were the original inspiration of our graphical method. Vertex models were introduced to count micro-configurations of the hydrogen bonds in ice, in order to estimate its residual entropy [208–210]. In this context, the arrow conservation constraint encodes local charge balance: each bond between water molecules must involve a single proton, drawn as a arrow in the vertex model. This essential discreteness is reflected in the set of allowed arrow configurations; vertex models are even named after the number of different vertices they allow, with the most famous example being the six-vertex model. Our kinematic graphs differ starkly in this regard, because they allow for an infinite number of local arrow configurations. The adaptation of some of the combinatorial methods that apply to statistical vertex models to the less constrained case of kinematic graphs certainly provides an interesting challenge.

Arrow conservation makes hinge nodes with two edges particularly trivial: we can erase such nodes and directly connect the adjacent kinematic nodes with a single edge. We make use of this in Fig.2.5(g). Finally, since the whole graph was determined by fixing a single arrow, we can replace it with an equivalent six-legged kinematic vertex, shown in Fig.2.5(k). This furnishes an abstract representation of the zero-mode represented in Fig.2.5(l) that captures the deformation of the external shape of the mechanism. This additional simplification comes at the cost of forgetting about the internal kinematics of the mechanism, which are

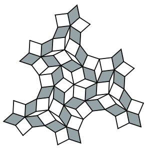

anyway irrelevant to understanding whether it is kinematically compatible with neighbouring mechanical elements.

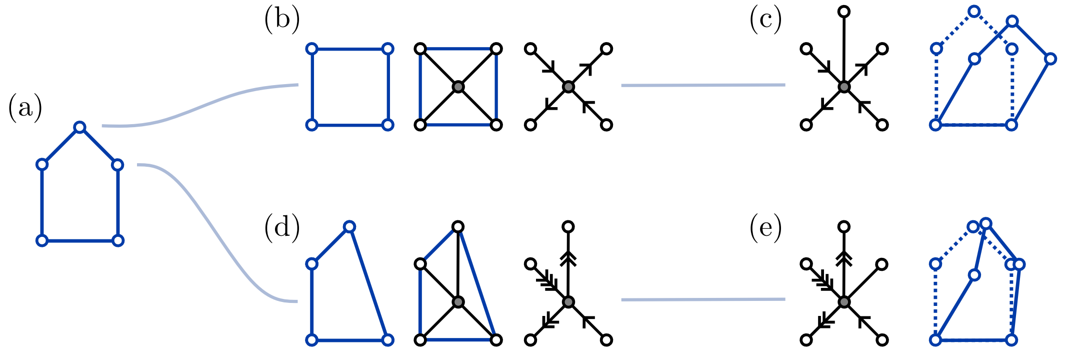

Figure 2.6: Kinematic graphs of a bimodal linkage. (a) Pentagonal linkage in the reference configuration. Hinges are represented by white disks and bars by solid blue lines. (b) Fixing the hinge in the top corner reveals a symmetric arrow rule, represented with solid black lines. (c) Representation of this DOF in the original structure. The reference configuration is represented with dashed lines, whereas the deformed configuration is represented with solid lines. (d) Fixing the top-right corner reveals a second DOF; we represent its effect on the original linkage in (e).

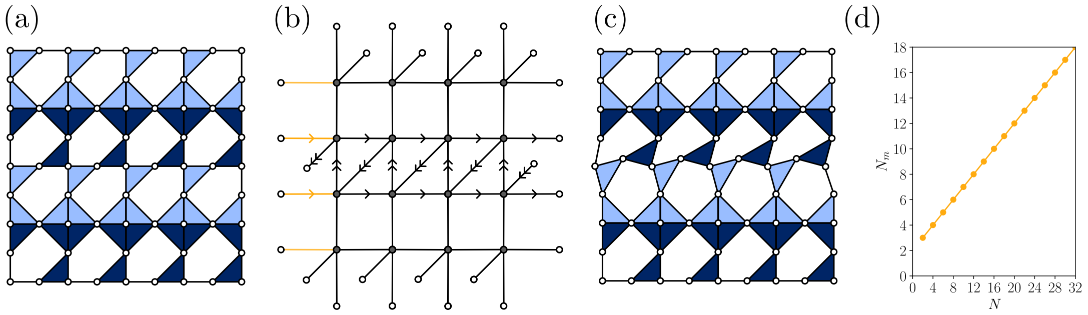

Figure 2.7: Localized modes and their extensive scaling. (a) Plurimodal metamaterial geometry in an undeformed state. Hinges are represented by white disks and bars by solid black lines. Rigid triangles are coloured in blue, with varying saturation to make it easier to determine the orientation of the unit cells. (b) Corresponding directed graph representation, with a compatible arrow configuration localized to two rows. (c) Real space representation of the localized mode. (d) Number of zero-modes as a function of system size in yellow.

2.2 Mechanical tilings and zero-mode scaling

Having tamed local kinematic complexity with these graphical tools, we can turn to the second difficulty we discussed: frustration effects in mechanical networks. To explore these effects, we tile the plane with the unit cell of Fig.2.6(a). Since it relies on a pentagonal linkage, it hosts two DOFs, which can again be obtained by successively fixing two different hinges, as shown in Fig.2.6(bd). This yields the two arrow rules depicted in Fig.2.6(ce). By construction, plane tilings relying on this bimodal unit cell have the same number of hinges and bars, and hence the same modal count. However, additional states of self-stress can arise, making room for further zero-modes. We start with a tiling that exhibits a large number of zero-modes and states of self-stress, shown in Fig.2.7(a). Note that we set the hinges on a Lieb lattice and simply change the orientation of the pentagonal linkage depending on the cell's position. The graph representation of this tiling is depicted in Fig.2.7(b). Playing the same arrow-fixing game as before, we note that one arrow needs to be constrained on every second row to fully fix the arrow content in the bulk. This is most easily visualised with the help of the arrow configuration of Fig.2.7(b), which is fully compatible with the arrow rules and remains localised on two rows. The corresponding real-space deformation is depicted on Fig.2.7(c). Such modes often arise in flexible metamaterials, as in early works by Guest and Hutchinson [211, 212]. In compressive experiments on foams [213–215], localized lines of deformation also occur regularly: we will call them line modes. Such modes make for a rather floppy material, since they allow each row to move independently. Their local character also implies that they scale extensively: in Fig.2.7(d), we plot the total number of zero modes N_m in a square $N \times N$ tiling as a function of N. Here, the scaling is linear, because of the 1D extension of the zero-modes. If they were instead localized in both directions, the number of zero-modes would instead scale quadratically in N. Such metamaterials, with a polynomially-scaling number of modes, will be termed plurimodal. To validate these combinatorial insights, we also carried a brute-force computation of the mode scaling with a more traditional compatiblity matrix approach. The compatibility matrix C lets us compute the bond extension $\vec{b} = C\vec{u}$ induced by infinitesimal displacement vector $\vec{u}$. Displacement vectors corresponding to zero-modes must fall in the kernel of C, since by definition they stretch no bond. To obtain the bond stretching induced by the displacement, we compute the distance between the two end nodes as

$$\begin{aligned}
b_{12} &= |\vec{r}_2 + \vec{u}_2 - \vec{r}_1 - \vec{u}_1| - |\vec{r}_2 - \vec{r}_1| = \sqrt{|\vec{r}_2 - \vec{r}_1|^2 - 2(\vec{r}_2 - \vec{r}_1)\cdot(\vec{u}_2 - \vec{u}_1) + |\vec{u}_2 - \vec{u}_1|^2} - |\vec{r}_2 - \vec{r}_1| \\
&\approx |\vec{r}_2 - \vec{r}_1| - \frac{(\vec{r}_2 - \vec{r}_1)\cdot(\vec{u}_2 - \vec{u}_1)}{|\vec{r}_2 - \vec{r}_1|} - |\vec{r}_2 - \vec{r}_1| \\
&= \frac{r_{2x} - r_{1x}}{|\vec{r}_2 - \vec{r}_1|} u_{1x} + \frac{r_{1x} - r_{2x}}{|\vec{r}_2 - \vec{r}_1|} u_{2x} + \frac{r_{2y} - r_{1y}}{|\vec{r}_2 - \vec{r}_1|} u_{1y} + \frac{r_{1y} - r_{2y}}{|\vec{r}_2 - \vec{r}_1|} u_{2y}, \qquad (2.6)
\end{aligned}$$

where $\vec{r}_i$ denotes the initial position of node i and $\vec{u}_i$ its displacement. Doing this for each bond, we obtain a matrix equation relating $\vec{b}$ and $\vec{u}$. To give a concrete example, the compatibility matrix of a square four-bar linkage can be written as

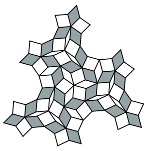

$$C = \begin{pmatrix} 1 & 0 & -1 & 0 & 0 & 0 & 0 & 0 \\ 0 & 0 & 0 & 1 & 0 & -1 & 0 & 0 \\ 0 & 0 & 0 & 0 & -1 & 0 & 1 & 0 \\ 0 & 1 & 0 & 0 & 0 & 0 & 0 & -1 \end{pmatrix}. \tag{2.7}$$

The kernel of this matrix is four-dimensional; from earlier discussions, we know that a basis consisting of two rigid translations, a rotation and a nontrivial mechanism can be picked. For instance, the displacement vector $\vec{u} = (u_{1x}, u_{1y}, u_{2x}, u_{2y}, u_{3x}, u_{3y}, u_{4x}, u_{4y})^T = (-1, -1, -1, 1, 1, 1, 1, -1)$ lies in the kernel of C and involves a nontrivial folding motion, namely the one depicted in Fig.2.3(a). When more degrees of freedom are present, we cannot easily pick an illuminating basis, but the zero-mode count still corresponds to the dimension of the kernel. This provides an alternative path to obtain the zero-mode scaling of Fig.2.7(d), by numerically computing compatibility matrix kernels for finite $N \times N$ tilings. Every mode-scaling plot shown in the remainder of the thesis was cross-checked using this method.

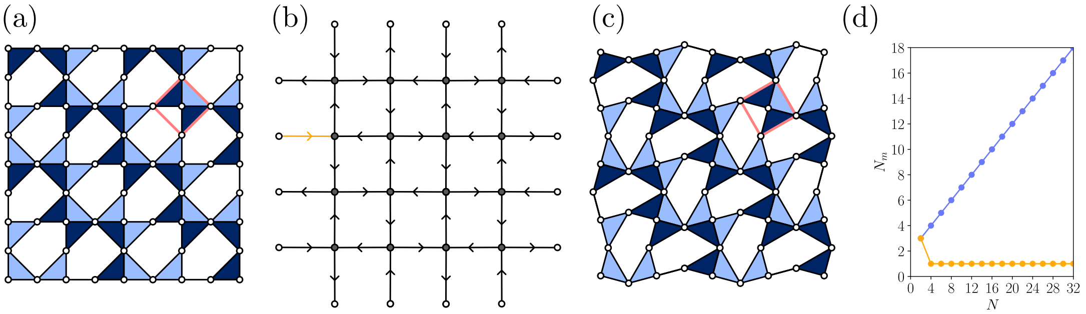

Figure 2.8: The counter-rotating squares mechanism. (a) Unimodal metamaterial geometry in an undeformed state. Note that the rigid elements composed of three triangles effectively behave as the virtual square drawn in pink. (b) Corresponding directed graph representation, with a compatible arrow configuration spreading on the entire graph uniformly. (c) Real space representation of the counterrotating squares mechanism. (d) Number of zero-modes as a function of system size in yellow, with previous mode scalings in blue.

In the above description of plurimodal structures, we passed over an important mode, which is present in every tiling of our pentagonal unit cell. To discuss it, we consider a highly frustrated configuration, represented in Fig.2.8(a). In this configuration, all the cells have a diagonal edge ending in a static set of triangles, which prevents it from being actuated. We can therefore erase all such edges to obtain the graph of Fig.2.8(b). Another way to see this is to consider that this geometry is kinematically equivalent to the counter-rotating squares geometry, as evidenced by the pink outline in Fig.2.8(a). Fixing an arrow anywhere on the graph is then sufficient to fully determine its arrow content; the metamaterial has a single zero mode. We depict the associated deformation in Fig.2.8(c). This mode is precisely the counter-rotating squares mode of Fig.1.7(e). In terms of mechanical properties, such geometries, which we might term unimodal, is more well-behaved than plurimodal ones. We contrast their mode-

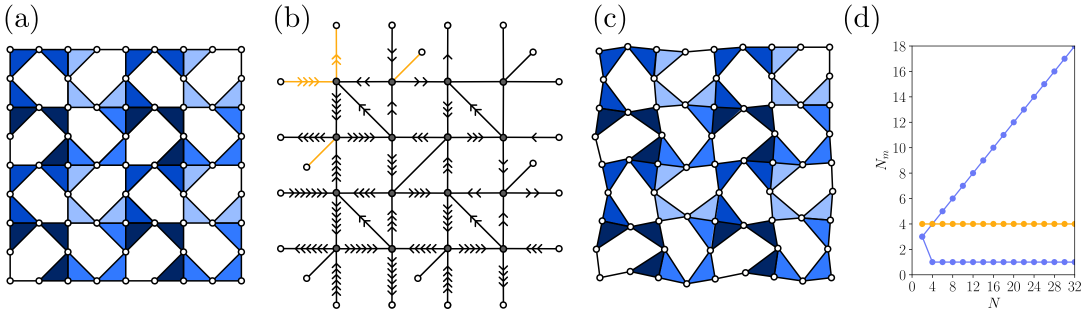

Figure 2.9: An oligomodal metamaterial. (a) Oligomodal metamaterial geometry in an undeformed state. (b) Corresponding directed graph representation, with a compatible arrow configuration spreading on the entire graph non-uniformly. The other three DOFs can be obtained by successive rotations of $\pi/2$. (c) Real space representation of this additional zero-mode. (d) Number of zero-modes as a function of system size in yellow, with previous mode scalings in blue.

scaling behaviours in Fig.2.8(d). We will see in the next chapter that the unimodal geometry also opens the way to very unusual wave physics. The central objective of the design method introduced in this chapter is to go beyond this isolated example of global zero-mode to create other geometries with an intensive number of zero modes, which we will call *oligomodal*. Crucially, we will show that such geometries can exhibit more that one global zero mode.

The first example of such a geometry is depicted in Fig.2.9(a). Playing our combinatorial arrow game again, we see that fixing arrows on four edges is necessary to fully determine the arrow content of the graph. One such arrow configuration is depicted in Fig.2.9(b), while the three others can be obtained by rotating it by steps of $\pi/2$. As for the counterrotating squares mode, it can be obtained as a linear combination of these four zero-modes. In contrast with the counterrotating squares case, the deformation pattern of Fig.2.9(bc) does not fill the plane uniformly; instead, the amount of deformation increases linearly along one diagonal and remains constant along the other diagonal. We will discuss the impact of this peculiar behaviour on the vibration spectrum in Chapter 6, and also address the tension between the linear increase and the small-angles assumption in Chapter 4. In mechanical terms, such structures are extremely interesting, because of their ability to deform into multiple global shapes without being entirely floppy. In Fig.2.9(d), we contrast the various scaling behaviours observed up to now, as well as an average over random tilings. It turns out that most tilings quickly become frustrated, only allowing for the counterrotating squares modes, which must be present by design. On the other hand, most periodic tilings host an extensive number of modes (See Appendix). Oligomodal geometries therefore reach a fine equilibrium between frustration and mechanical floppiness by exhibiting a finite number of global deformation modes.

To close the chapter, we consider one last class of tilings: nonrandom aperiodic tilings. Quasicrystals provide a famous example of order without periodicity [216–219]. In Fig.2.10(ab), we

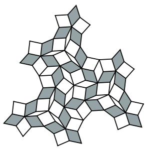

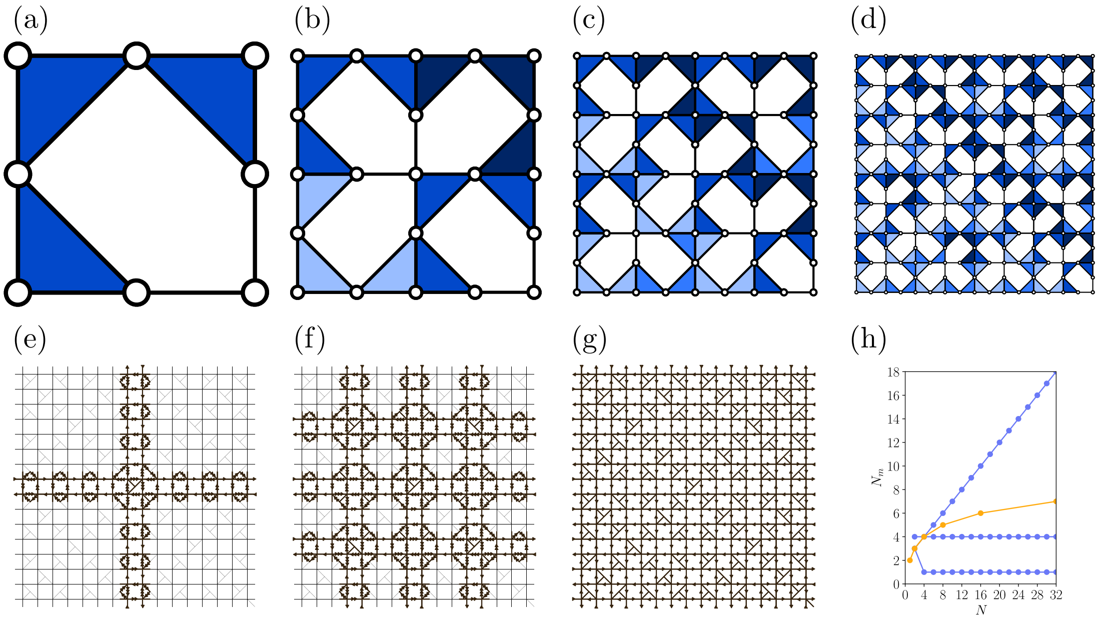

Figure 2.10: Quasicrystalline geometry with logarithmically scaling number of mechanisms. (a-d) First four iterations of the fractal substitution rule. (e-g) Graph representation of the fifth iteration of the substitution rule, with three zero-modes associated to increasingly finer spatial scales. The actuated edges are drawn in a darker shade to emphasise their spatial patterns. (h) Number of zero modes as a function of system size in yellow, with previous mode scalings in blue.

show a fractal substitution rule, in which a square unit-cell is substituted with four smaller copies placed in various orientations. Applying this substitution rule iteratively, as shown in Fig.2.10(cd), yields a quasicrystalline tiling. Interestingly, when analysed in the vertex model formalism, this tiling is shown to host a limited number of zero-modes, at finer and finer spatial scales. These modes are shown in Fig.2.10(e-g). A new mode is introduced every time we apply the fractal substitution rule. This has the effect of doubling the system size, which leads to a logarithmically scaling number of zero modes, as shown in Fig.2.10(h). Quasicrystal order therefore offers an intriguing intermediate case between oligomodality and plurimodality.

In this chapter, we introduced a visual design method for flexible metamaterials based on directed graphs, turning a complex kinematic problem into a combinatorial game. We then leveraged this method to classify mechanical metamaterials based on the scaling behaviour of their zero-mode content. When too many constraints are present, the material is rigid: it does not host nontrivial zero-modes. This is the case of most elastic media. The opposing limit in which there are too few constraints leads to the plurimodal class. Metamaterials in this class are quite floppy: they can accommodate a wide set of deformations. Most flexible metamaterials belong to this class.

Most interestingly, we uncovered the existence of an intermediate scaling class, the *oligomodal* class. Oligomodal metamaterials host a number of global zero-modes that does not increase with system size. Such metamaterials walk a fine line between controlled behaviour and floppiness. These characteristics are promising for our quest of elastic nonlocal resonances, because the latter also rely on a limited number of global degrees of freedom. In the following chapter, we will make this connection concrete and use it to design nonlocally-resonant metamaterials.

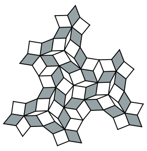

3 Anomalous Dispersion Cones

> *"Bon ça veut rien dire, mais je trouve que ça sonne bien."*
>
> — B. Apffel, citing R. Loth

As promised, we will now leverage the graphical method developed in the previous chapter to design the low-frequency spectrum of flexible metamaterials. Our ambition in this chapter is to describe the spectral signatures of nonlocal resonances, as well as their impact on wave propagation. To that end, we relax our assumption of infinitely rigid bars, turning to dynamical models. We will focus on a subclass of oligomodal geometries which host zero-energy Bloch waves with nonzero wave-vectors, *i.e.* nonolocal resonances. Crucially, we will see that this particular class of metamaterials fulfills our hopes: it exhibits anomalous dispersion cones, like interlaced wire media.

In Sec.3.1, we introduce a minimal 1D model of anomalous cones, which we use to investigate some of their 1D properties. Then, in Sec.3.2, we introduce a 2D oligomodal geometry hosting two anomalous cones, which we use in Sec.3.3 to investigate the essentially 2D phenomenon of negative refraction, demonstrating that nonlocally-resonant metamaterials are not subject to the same limitations as phononic crystals and locally-resonant metamaterials. Finally, we conclude the chapter with Sec.3.4, in which we discuss three more examples of nonlocally-resonant metamaterials designed with our graphical method. We use these examples to show that the location and number of anomalous cones is controlled by our kinematic-graph theory.

3.1 Anomalous cone in a one-dimensional chain.

As a warm-up, we will first consider a minimal 1D model inspired by the counter-rotating squares mechanism. We start by considering a single column of the counter-rotating squares metamaterial, depicted in Fig.3.1(a). A kinematic graph analysis (Fig.3.1(b)) reveals that this 1D chain hosts a single nontrivial mechanism, like its parent structure. We then seek to simplify it further, to obtain a model that exhibits the essential properties of interest while remaining

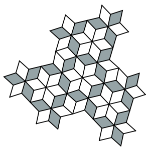

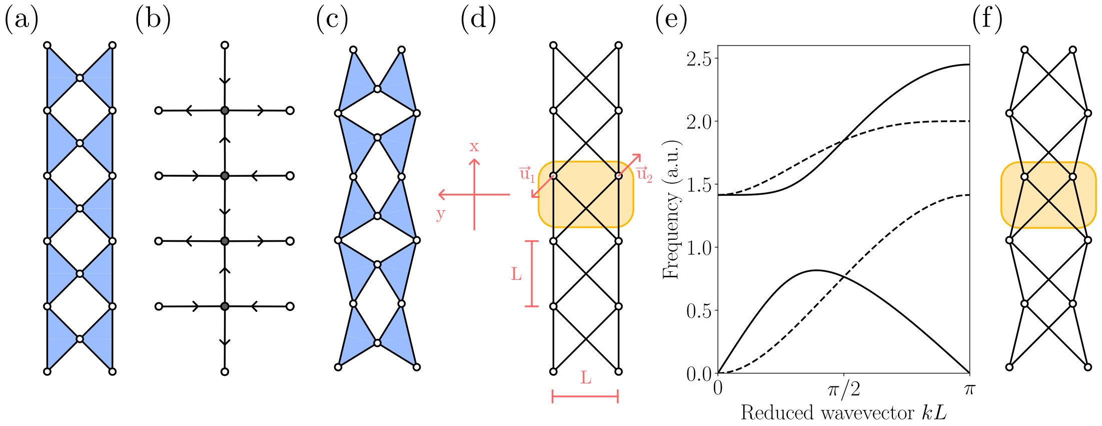

Figure 3.1: Minimal 1D model exhibiting a single anomalous cone. (a) 1D version of the counter-rotating squares metamaterial, with hinges as white dots and rigid bars as black lines. Rigid triangles are highlighted in blue. (b) Graph description of the single nontrivial zero-mode of this chain. (c) Real-space representation of this zero-mode. (d) An even simpler chain with only two hinges per unit cell (highlighted in yellow). (e) Vibrational spectrum of the chain in (d), with hinges replaced by point masses and rigid bars replaced by springs. The solid lines correspond to modes that are symmetric under reflection accross the x axis, wheras the dashed lines correspond to antisymmetric modes. (f) Real-space representation of the $kL = \pi$ zero-mode lying at the edge of the Brillouin zone.

analytically tractable. The geometry of this minimal chain, which involves only two point masses per unit cell, is depicted in Fig.3.1(d). It relies on an inverted four-bar mechanism which captures the essence of the counter-rotating squares mode with a unit cell of even lower complexity. It is apparent both from the graph of Fig.3.1(b) and from the real deformation of Fig.3.1(c) that the displacement pattern within neighbouring cells is reversed, picking up a phase of π. We therefore expect the frequency associated to Bloch waves whose wavenumber approaches π/L to tend to zero.

In order to investigate this prediction, we need a way to model finite frequency vibrations in our metamaterials. A straightforward approach is to promote one of the main characters of the last chapter, namely the rigid bar, to a spring of finite stiffness. We also confer more gravitas to the hinge by making it massive. Other choices of mass repartition will be made as we refine our models to get closer to realistic geometries, but this massive-hinge Ansatz has the benefit of fully capturing the zero-frequency content of the spectrum, which does not depend on mass repartition, for a low cost in complexity.

In this setting, the zero-modes studied in Ch.2 simply correspond to motions of the point masses (collected in a displacement vector $\vec{u}$) that do not stretch any spring. In Eq.(2.7), we already introduced a compatibility matrix C to compute the bar extension vector $\vec{b}$ from the displacement vector $\vec{u}$, taking us halfway to the vibration spectrum. We keep going and compute the tensions $\vec{t}$ by applying Hooke's law, multiplying $\vec{b}$ with a diagonal stiffness matrix K. Then, we apply the equilibrium matrix Q, which restitutes the directions in which the

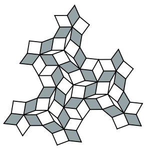

forces apply. The resulting matrix is the dynamical matrix, noted $\mathscr{D}$,

$$M\ddot{\vec{u}} = \vec{f} = -Q\vec{t} = -QK\vec{b} = -QKC\vec{u} = -\mathscr{D}\vec{u}. \tag{3.1}$$

In the following, unless otherwise specified, we will set all the masses and the spring stiffnesses equal to one, meaning $M = K = \mathbb{1}$. This choice has no impact whatsoever on the zero-frequency content of the spectrum, so we elect to keep things as simple as possible for as long as we can. We also leverage a convenient relation [200] between the compatibility and equilibrium matrices, namely $Q = C^T$. This implies that the dynamical matrix simply becomes $\mathscr{D} = C^T C$. To give a concrete example, we apply this approach to our 1D chain model. Collecting the displacements of the two point masses as $\vec{u} = (u_{1x}, u_{1y}, u_{2x}, u_{2y})^T$ and noting that there are four bars, we can then write the compatibility matrix as a four-by-four matrix acting on $\vec{u}$,

$$C = \begin{pmatrix} 1-e^{-ikL} & 0 & 0 & 0 \\ 0 & 0 & 1-e^{-ikL} & 0 \\ \frac{1}{\sqrt{2}} & \frac{1}{\sqrt{2}} & -\frac{e^{-ikL}}{\sqrt{2}} & -\frac{e^{-ikL}}{\sqrt{2}} \\ -\frac{e^{-ikL}}{\sqrt{2}} & \frac{e^{-ikL}}{\sqrt{2}} & \frac{1}{\sqrt{2}} & -\frac{1}{\sqrt{2}} \end{pmatrix}, \tag{3.2}$$

which we obtained by computing the euclidean distance between the ends of each bond, and then linearising these expressions for small displacements, as in Ch.2. Note that we also made use of Bloch's theorem by assuming that the displacement of neighbouring unit cells in our infinite chain are related by a phase e^{ikL}. The symmetries of this chain go beyond translation symmetry; for instance, it is also invariant under reflections across the x-axis, reflections across the y-axis and π rotations around the origin[I]. We will discuss the consequences of such symmetries in Ch.7 in detail; for now, we only leverage a particularly convenient aspect of symmetry to simplify our discussion of the band structure. Consider in particular the reflection across the x-axis, denoted as M_x; since it commutes with both the dynamical matrix and the translation operator, we can go over to a basis of displacements that are either symmetric or antisymmetric under this reflection using the matrix

$$P = \frac{1}{\sqrt{2}} \begin{pmatrix} 1 & & -1 & \\ & 1 & & 1 \\ 1 & & 1 & \\ & -1 & & 1 \end{pmatrix}. \tag{3.3}$$

[I] In fact, if we include all such operations, including the ones centered around symmetry points away from the origin, they form the frieze group $p2mm$.

One can directly verify that the new basis vectors are eigenvectors of M_x; they are given by

$$\left|\begin{matrix}\rightarrow\\ \rightarrow\end{matrix}\right\rangle = \begin{pmatrix}1/\sqrt{2}\\ 0\\ 1/\sqrt{2}\\ 0\end{pmatrix} \quad \left|\begin{matrix}\uparrow\\ \downarrow\end{matrix}\right\rangle = \begin{pmatrix}0\\ 1/\sqrt{2}\\ 0\\ -1/\sqrt{2}\end{pmatrix} \quad \left|\begin{matrix}\leftarrow\\ \rightarrow\end{matrix}\right\rangle = \begin{pmatrix}-1/\sqrt{2}\\ 0\\ 1/\sqrt{2}\\ 0\end{pmatrix} \quad \left|\begin{matrix}\uparrow\\ \uparrow\end{matrix}\right\rangle = \begin{pmatrix}0\\ 1/\sqrt{2}\\ 0\\ 1/\sqrt{2}\end{pmatrix} \tag{3.4}$$

in the original basis. In the new basis, the chain symmetries become manifest and the dynamical matrix takes on a block-diagonal form,

$$\begin{aligned}\mathscr{D}_{chain} &= P^T C^T C P \\ &= \begin{pmatrix}\mathscr{D}_S & \\ & \mathscr{D}_A\end{pmatrix} = \begin{pmatrix} 3-3\cos(kL) & -i\sin(kL) & & \\ i\sin(kL) & 1+\cos(kL) & & \\ & & 3-\cos(kL) & i\sin(kL) \\ & & -i\sin(kL) & 1-\cos(kL)\end{pmatrix},\end{aligned} \tag{3.5}$$

where the subscripts S and A denote the symmetric and antisymmetric sectors. Diagonalising $\mathscr{D}_{chain}(k)$, we obtain the vibration spectrum of our chain, which is depicted in Fig.3.1(e).

Focusing on the lowest bands, we note that two dispersion cones are present at the Γ point[II]; they correspond to the longitudinal and transverse waves present in planar continuum elasticity. Since these two bands intersect the zero-frequency axis, it must be possible to interpret the associated modes in terms of the zero-modes discussed in Ch.2. Indeed, in the infinite-wavelength limit reached at Γ, longitudinal waves turn into a rigid translation along the chain axis, whereas transverse waves turn into a rigid translation perpendicular to the chain axis. In fact, we can even interpret these rigid-body modes as Goldstone modes of the translation symmetry broken by the crystalline arrangement. In other words, the position of the crystal relative to the origin is arbitrary: the Goldstone mode of translation allows one to connect distinct symmetry-breaking choices with one another at no energetic cost. The rotational zero-mode hides in the spectrum in a subtler way, which we will discuss in Chapter 6. These account for the three rigid zero-modes that any planar elastic medium holds.

More strikingly, an additional zero-energy mode appears at the edge of the Brillouin zone. It intersects the zero-frequency axis at a single location, which is consistent with the graph representation of the zero-mode shown in Fig.3.1(b). There, the orientation of the arrows is reversed between neighbouring cells, meaning that we expect a zero-mode at $kL = \pi$. By our definition in Ch.1, this zero-mode constitutes a nonlocal resonance; it should be associated to

---

[II] Γ is a commonly used name for the point at which $k = 0$. Other high-symmetry points of the Brillouin zone are similarly labeled, we point the unfamiliar reader to Ref.[220] for an introduction.

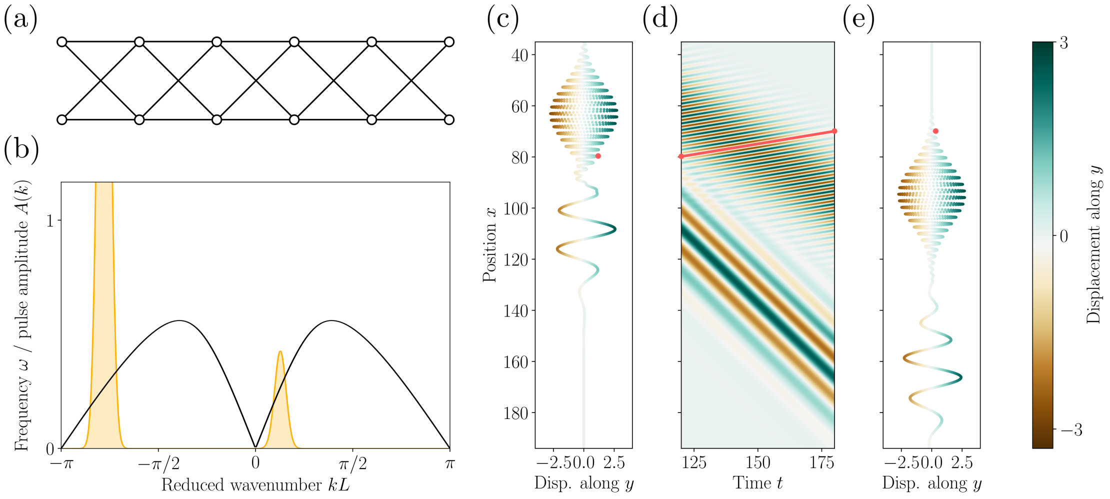

Figure 3.2: Sending pulses through a nonlocally-resonant chain. (a) A six-site version of the elastic chain, with point masses as white dots and springs as black lines. (b) The spatial Fourier transform $A(k)$ of our sum of wave-packets is represented in yellow, with the first band of the spectrum superimposed as a black line. (c) Displacement u_y as a function of position at $t = 120$, with the position of an arbitrary peak singled out with a pink dot. (d) Space-time diagram of u_y; the relative sign of phase and group velocity determines the orientation of the phase fronts. The trajectory of the pink dot is represented as a pink line. (e) Displacement u_y as a function of position at $t = 180$.

a shifted dispersion cone. In Fig.3.1(e), we observe precisely such a shifted cone at the edge of the Brillouin zone. As for the nonlocal resonance, it is depicted in Fig.3.1(f).

We call such shifted dispersion cones *anomalous cones*. In the remainder of the chapter, we will explore their wave physics using several increasingly more realistic examples. Already in the toy model, we note that anomalous cones are associated to a large domain of negative group velocity. Taking a derivative of the analytical expression for the anomalous band

$$\omega = \sqrt{2 - \cos(kL) - \sqrt{3\cos(kL)^2 - 4\cos(kL) + 2}} \tag{3.6}$$

with respect to k, we find that the threshold between positive and negative group velocity lies at $kL = \arccos\left(2/3 - \sqrt{10}/6\right) \approx 0.45\pi$. The eigenmodes associated to this branch transition from being purely longitudinal at $k = 0$ to purely anomalous at $k = \pi/L$, as seen in

$$\vec{u} = i\sin(kL)\left|\begin{matrix}\rightarrow\\ \rightarrow\end{matrix}\right\rangle + \left[1 - 2\cos(kL) + \sqrt{3\cos(kL)^2 - 4\cos(kL) + 2}\right]\left|\begin{matrix}\uparrow\\ \downarrow\end{matrix}\right\rangle. \tag{3.7}$$

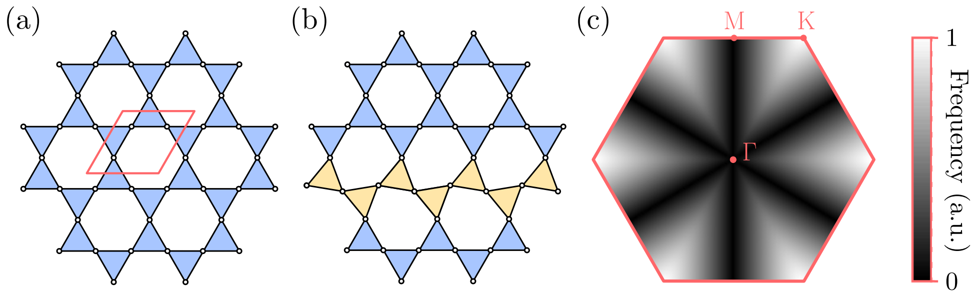

Figure 3.3: The spectral signature of line modes. (a) Kagome metamaterial, with point masses as white disks and springs as black lines. Spring triangles, which become rigid for $\omega = 0$, are highlighted in blue. The unit cell of the network is indicated with a red line. (b) A zero-energy line mode, with rotated triangles shown in yellow. (c) First band of the corresponding vibration spectrum, exhibiting lines of zeroes in directions perpendicular to the line modes.

The presence of anomalous cones has several interesting physical consequences; our minimal model of nonlocally-resonant chain (Fig.3.2(a)) already allows us to probe their impact on pulse propagation. We set up two pulses by summing up the Bloch eigenmodes of Eq.(3.7), with the wave-vector content depicted in Fig.3.2(b). Note that it consists of two gaussian wavepackets with the same temporal frequency content, both lying on the longitudinal-anomalous band. The corresponding displacement field, shown in Fig.3.2(c), is then simply advanced in time by evolving each Bloch eigenmode harmonically, with ω given by Eq.(3.6). As shown in the space-time diagram of Fig.3.2(d), the interval separating the two gaussian pulses increases with time, on account of their differing group velocities.

Should the anomalous pulse not move backwards, due to its negative group velocity ? It does not, because we selected the right-moving solution, as apparent in Fig.3.2(b). This choice is justified by causality: power should flow away fromt the source. The effect of the negative sign is then simply that the right-moving solution is composed of left-moving phase components; the phase and group velocities have opposite signs. This is made clear in the space-time diagram of Fig.3.2(d). There, the standard pulse moves at the same speed as its internal peaks, on account of the largely linear dispersion relation[III]. In contrast, the phase components of the anomalous pulse slope in a direction opposite to its propagation. This can also be seen by comparing the individual time-slices of Fig.3.2(ce), where we tracked the position of an internal phase peak with a pink dot, which shows its backward movement.

Illustrating other features associated to negative group velocity will require us to go over to a two-dimensional setting. We briefly take this opportunity to consider what happens to another class of zero-modes, namely the line modes described in Fig.2.7. To do so, we consider

---

[III] A slight dispersion-induced broadening of the wavepackets is also visible; it would become more important as we move on to higher center frequencies. This ultimately leads to an interesting merging of the anomalous and standard solution into a single wavepacket with vanishing group velocity. The associated quadratic dispersion then means that the propagation process becomes diffusive rather than wave-like. In this situation, care must be exerted in the choice of the right-moving and left-moving parts of the spectrum, particularly if we want to describe the situation at an interface with a standard elastic chain.

the example of the Kagome lattice (Fig3.3(a)) studied in Ref. [152, 200, 211], which incidentally also corresponds to the paper folding held by Resch in Fig.1.7. Its ability to comply to various bending conditions, demonstrated in Fig.1.7(a), hints at plurimodality. A kinematic graph analysis indeed confirms the presence of line modes whose number scales linearly with the perimeter of the metamaterial. This places the Kagome geometry within the plurimodal class described in Fig.2.7. The deformation pattern associated to such a line mode is highlighted in yellow in Fig.3.3(b). Writing the dynamical matrix associated to the unit cell isolated with a pink line in Fig.3.3(a), we can obtain the spectrum associated with this Kagome lattice, already reported in several references [200, 221]. We show the lowest band of the spectrum in Fig.3.3(c) over the first Brillouin zone. The most outstanding features in this picture are clearly the zero-frequency lines crossing the Γ point. Their emergence in plurimodal structures can be understood as follows: since each row is free to move independently, any periodic pattern of row deformations can be realised. This means in particular that any k-vector pointing in the direction perpendicular to these rows is admissible as a zero-mode. Therefore, a zero-frequency line appears along this direction in the first band.

Such plurimodal geometries are discussed extensively in other parts of the litterature, and they host a plethora of interesting physics, in spite (or maybe because) of their general floppiness. Instead of the negative branches we discussed with the help of a 1D elastic chain, they provide directions of zero group velocity. We however note an intriguing possibility here: if one could find plurimodal geometries that somehow exclude the formation of long-wavelength zero-energy deformations, the associated zero-mode lines would not pass through the Γ point and could potentially be perpendicular to the lines of Fig.3.3(c). Such zero-mode lines could conceivably even take on the form of zero-mode rings encircling the Γ point. This in turn would lead to negative-index wave physics. In this thesis, we consider another path: oligomodal geometries and their associated anomalous cones.

3.2 Multiple cones in an oligomodal metamaterial.

Catching two birds with one stone, we now consider a two-dimensional oligomodal structure; this will allow us to show that several anomalous cones can coexist if the structure holds more than one nonlocal resonance. It will also allow us to probe two-dimensional effects such as negative refraction.

This metamaterial is based on the unimodal hexagonal cell first described in Fig.2.5. Covering the plane with this cell, we obtain the geometry depicted in Fig.3.4(a). As a first step, we apply the combinatorial method of Ch.2 to identify the zero-modes in the tiling. In the graph representation of the metamaterial, shown in Fig.3.4(b), we used the equivalent six-legged kinematic node derived in Fig.2.5(k). We can already note that this graph has a novel feature compared to the other tilings considered up to now; indeed, every external hinge node (represented by white disks) is shared between three cells. Since such nodes are only constrained by arrow conservation, this provides a new type of kinematic degree of freedom.

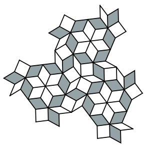

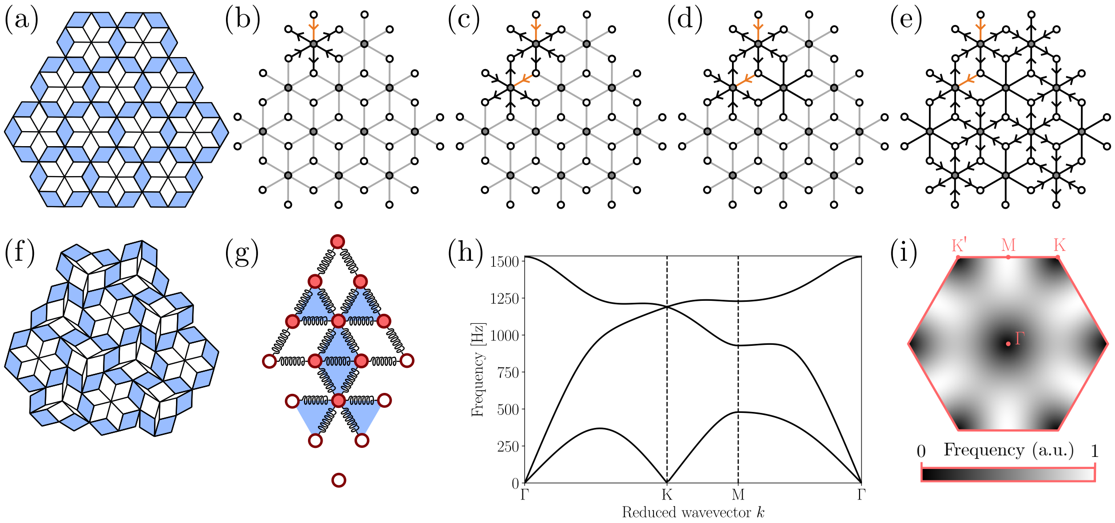

Figure 3.4: Multiple anomalous cones in a two-dimensional nonlocally-resonant metamaterial. (a) Geometry based on the composite cell of Fig.2.5(a), omitting the hinge disks for clarity. The blue diamonds represent rigid areas and the black lines rigid bars. (b) Equivalent graph representation, with hinge nodes as white disks and kinematic nodes as black disks. A single arrow, represented in orange, was fixed as a boundary condition. This determines five further edges through an arrow rule, which we draw in black. Undetermined edges are drawn in grey. (c) Same graph with a second arrow fixed arbitrarily. In (d), we see that this adds enough constraints to determine the arrow pattern of a neighbouring cell. (e) Cascading constraints lead to coherently decorate all the edges with arrows. (f) Associated real-space deformation pattern. (g) Unit-cell of a spring-mass model for this metamaterial. (h) Band structure of the spring-mass model along high-symmetry lines. (i) Frequency of the first band over the first Brillouin zone.

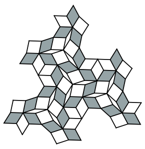

Let us explore the associated combinatorial game: in Fig.3.4(b), we draw an arbitrary arrow, represented in orange. This then determines the arrow content of five further edges through the arrow rule of the kinematic grey node. Because of the three-edge freedom of the hinge nodes, constrained arrow propagation stops there. We try to kick-start it a second time, by fixing an additional edge in Fig.3.4(c). This determines five more edges; in particular, two hinge nodes are shared between the arrow-filled cells. Since these hinge nodes now only have a single edge whose arrow content was not fixed, the arrow conservation constraint becomes sufficient for arrow propagation. We can therefore fix one more cell through its kinematic node, as shown in Fig.3.4(d). The arrow-drawing process then starts cascading, because additional hinge nodes now have two fixed edges; the arrow content of the entire graph is determined (Fig.3.4(e)). Since we needed to fix two arrows and obtained a directed graph without internal contradictions, we can conclude that the metamaterial hosts two nontrivial zero-modes. The real-space deformation associated to one of these modes is represented in Fig.3.4(f). We note that a triangular pattern of undeformed cells emerges, with the second mode simply corresponding to a shifted pattern of undeformed cells. Of course, as long as the resulting mode respects the assumption of infinitesimal deformations, any linear combination of these two modes is also admissible.

The spatial periodicity of these zero-modes is particularly interesting: like their undeformed counterparts, the deformed cells also arrange themselves on triangular lattices. One of these sets only contains cells that tend to acquire the shape of an upward-pointing triangle, whereas the other set contains cells with the exactly opposite internal deformation state. In other words, the upper arrow of one of the deformed cell sets points down, whereas the upper arrows of the other cell set point up. Since the overall mode repeats itself every third cell, this kinematic graph analysis predicts the presence of two zero-modes in the spectrum, one located at the K point and the other at the K' point. To verify whether this prediction holds and to see how a finite number of zero modes influences the spectrum, we compute the dynamical matrix associated to the unit cell of Fig.3.4(g), finding

$$\mathscr{D}_h = \begin{pmatrix}
12 & & -4 & & -4\Upsilon & & -1 & -\sqrt{3} & & & -\Upsilon & \sqrt{3}\Upsilon & -\Lambda & -\sqrt{3}\Lambda & -\Lambda & \sqrt{3}\Lambda & & \\
 & 12 & & & & & -\sqrt{3} & -3 & & & \sqrt{3}\Upsilon & -3\Upsilon & -\sqrt{3}\Lambda & -3\Lambda & \sqrt{3}\Lambda & -3\Lambda & & \\
-4 & & 10 & & -4 & & & & -1 & -\sqrt{3} & & & & & & & -\Lambda & \sqrt{3}\Lambda \\
 & & & 6 & & & & & -\sqrt{3} & -3 & & & & & & & \sqrt{3}\Lambda & -3\Lambda \\
-4\bar{\Upsilon} & & -4 & & 10 & & & & -1 & \sqrt{3} & & & & & & & -\Lambda & -\sqrt{3}\Lambda \\
 & & & & & 6 & & & \sqrt{3} & -3 & & & & & & & -\sqrt{3}\Lambda & -3\Lambda \\
-1 & -\sqrt{3} & & & & & 7 & \sqrt{3} & -4 & & & & -1 & -\sqrt{3} & & & -\Upsilon & \sqrt{3}\Upsilon \\
-\sqrt{3} & -3 & & & & & \sqrt{3} & 9 & & & & & -\sqrt{3} & -3 & & & \sqrt{3}\Upsilon & -3\Upsilon \\
 & & -1 & -\sqrt{3} & -1 & \sqrt{3} & -4 & & 12 & & -4 & & -1 & \sqrt{3} & -1 & -\sqrt{3} & & \\
 & & -\sqrt{3} & -3 & \sqrt{3} & -3 & & & & 12 & & & \sqrt{3} & -3 & -\sqrt{3} & -3 & & \\
-\bar{\Upsilon} & \sqrt{3}\bar{\Upsilon} & & & & & & & -4 & & 7 & -\sqrt{3} & & & -1 & \sqrt{3} & -1 & -\sqrt{3} \\
\sqrt{3}\bar{\Upsilon} & -3\bar{\Upsilon} & & & & & & & & & -\sqrt{3} & 9 & & & \sqrt{3} & -3 & -\sqrt{3} & -3 \\
-\bar{\Lambda} & -\sqrt{3}\bar{\Lambda} & & & & & -1 & -\sqrt{3} & -1 & \sqrt{3} & & & 7 & \sqrt{3} & & & -4\Upsilon & \\
-\sqrt{3}\bar{\Lambda} & -3\bar{\Lambda} & & & & & -\sqrt{3} & -3 & \sqrt{3} & -3 & & & \sqrt{3} & 9 & & & & \\
-\bar{\Lambda} & \sqrt{3}\bar{\Lambda} & & & & & & & -1 & -\sqrt{3} & -1 & \sqrt{3} & & & 7 & -\sqrt{3} & -4 & \\
\sqrt{3}\bar{\Lambda} & -3\bar{\Lambda} & & & & & & & -\sqrt{3} & -3 & \sqrt{3} & -3 & & & -\sqrt{3} & 9 & & \\
 & & -\bar{\Lambda} & \sqrt{3}\bar{\Lambda} & -\bar{\Lambda} & -\sqrt{3}\bar{\Lambda} & -\bar{\Upsilon} & \sqrt{3}\bar{\Upsilon} & & & -1 & -\sqrt{3} & -4\bar{\Upsilon} & & -4 & & 12 & \\
 & & \sqrt{3}\bar{\Lambda} & -3\bar{\Lambda} & -\sqrt{3}\bar{\Lambda} & -3\bar{\Lambda} & \sqrt{3}\bar{\Upsilon} & -3\bar{\Upsilon} & & & -\sqrt{3} & -3 & & & & & & 12
\end{pmatrix}$$

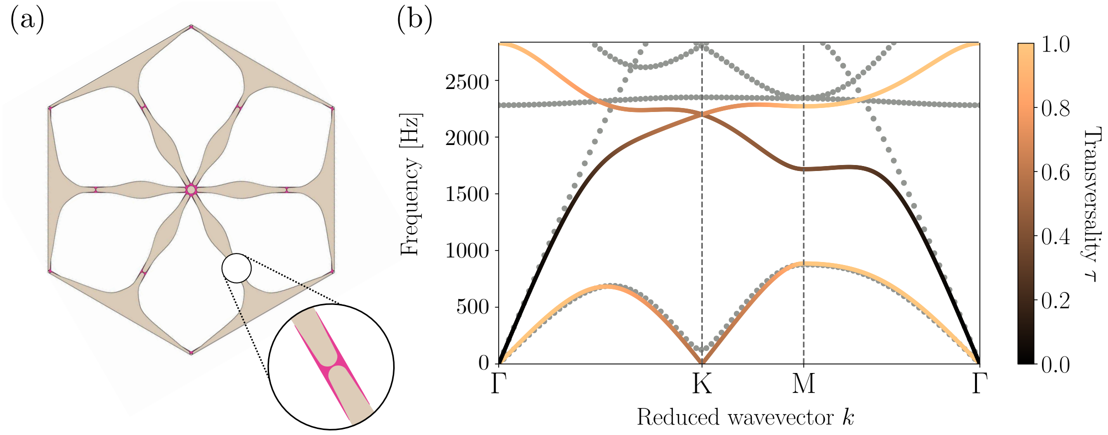

Figure 3.5: Comparison between spring-mass and FEM spectra. (a) Geometry of the unit cell used in the FEM simulation. Brown areas correspond to a rigid material, and pink ones to a very soft material. (b) Grey dots were obtained by FEM, while the superimposed coloured curve was obtained with a spring-mass model.

(3.8)

where we defined $\Lambda := e^{-3i(k_x+\sqrt{3}k_y)}$ and $\Upsilon := e^{-6i\mathrm{kx}}$ for readability. The spectrum of this matrix along high symmetry lines is shown in Fig.3.4(h), while the full first band is represented in Fig.3.4(i). As predicted, it presents two standard cones at the origin, as well as two anomalous cones, one at K and one at K'. How much can we trust this result ? Does it also hold for realistic geometries ? After all, we used many simplifying assumptions along the way. Let us recall a few of these: we considered mass and stiffness matrices equal to the identity, and we concentrated the mass precisely on the hinges. Even more importantly, we implicitely assumed hinges of vanishing width, which is of course not possible in practice. To address these potential issues, we now turn to full-wave simulations using the finite-element method (FEM), which will allow us to simulate more realistic systems.

In these simulations, the springs and masses give way to continuous elastic domains, yielding the unit cell depicted in Fig.3.5(a). The mass is no longer concentrated on the hinges, and the hinges can no longer be point-like. To mimic the behaviour of the ideal hinges we employed up to now, we construct them out of a soft material, with a Young's modulus of 12 MPa and a density of 1190 kg/m^3. With this choice, we anticipate the fact that the 3D-printed hinges of Sec.4.2 consist of thermoplastic polyurethane (TPU). We also equip them with a geometry that favours bending over stretching, depicted in the inset of Fig.3.5(a). As for the rigid bars of our kinematic models, they become elastic domains with a higher Young's modulus of $E = 3500$ Mpa, as well as a geometry that disfavours bending. The rationale here is simply to make the central part of these beam-like domains wider, to make the energetic cost of bending higher. For these rigid regions, the values $E = 3500$ MPa and $\rho = 1240$ kg/m^3 were chosen to approximate the elastic constants of polyactic acid (PLA), also in anticipation of

3D-printing. Enforcing Floquet-Bloch boundary conditions between opposing edges of the unit-cell, we then conduct an eigenfrequency FEM study (in COMSOL) in which we sweep the Bloch wave-vector along high-symmetry lines of the first Brillouin zone. The resulting eigenfrequencies are shown as grey points in Fig.3.5(b). The superimposed coloured lines come from the spring-mass model.

Given their widely different stiffness and mass distributions, the two approaches agree surprisingly well in their low-frequency spectrum. For instance, the longitudinal (light colour) waves and the transverse (dark colour) waves in the spring-mass model fall on top of their FEM counterparts over a large range [IV]. The colour-coding of the spring-mass spectrum refers to the average inner product of the normalised displacement and the wavevector, providing a measure of mode transversality. Now is a good time to remember that until Ch.7, we only consider the in-plane displacement sector: out-of-plane motion is decoupled by the 2D character of the considered geometries. When we talk about transverse waves, we do so with a purely two-dimensional notion of transversality.

Using this transversality measure reveals that the anomalous-cone modes are neither purely transverse nor longitudinal, but they hybridise with the transverse modes. A notable difference is the mass gap that opens up at the K point in the FEM simulation; this is simply the consequence of the non-ideality of the hinges in this model. These more realistic hinges ask for a toll in terms of elastic energy, which is reflected by this gap at the basis of the anomalous cone. It is then a matter of hinge design, in terms of geometry and choice of materials, to lower this cost as needed. A bigger discrepancy occurs in the upper part of the spectrum: there, the internal springs and the rigid elements stretch appreciably, and the differences in internal structure between the two models start to matter. At these higher frequencies, we leave the realm of low-frequency modes controlled by the kinematic graph theory to enter a regime dominated by the internal mass and stiffness structure and local resonances.

3.3 Broadband negative refraction

With the realistic geometry of Fig.3.5(a) at our disposal, we can start probing an essentially two-dimensional property of anomalous cones, namely broadband negative refraction. As shown in Fig.3.6(a), we set up a metamaterial domain comprising $29 \times 42 = 1218$ unit cells of the type depicted in Fig.3.5(a) next to an isotropic elastic domain. The latter domain is filled with an elastomer-like compound with density $\rho = 1020 kg/m^3$, and Young's modulus $E = 0.26$ MPa. Next, we surround the domains with partially matched layers, shown in Fig.3.6(b), and impose a monochromatic gaussian beam with $f = 48$ Hz boundary condition in the bottom left corner. The resulting frequency domain study yields the field distribution of Fig.3.6(a), in

---

[IV] A potential explanation for this unexpected agreement is that the ratio between the two speeds of sound is controlled by Poisson's ratio, which is in turn determined by the essentially identical kinematics of the two media. To fully hold water, this explanation should be generalized to account for the fact that anisotropic elastic media can have up to six independent elastic constants in 2D. It might even be necessary to consider Cosserat elasticity, given that internal elements rotate as we press.

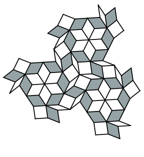

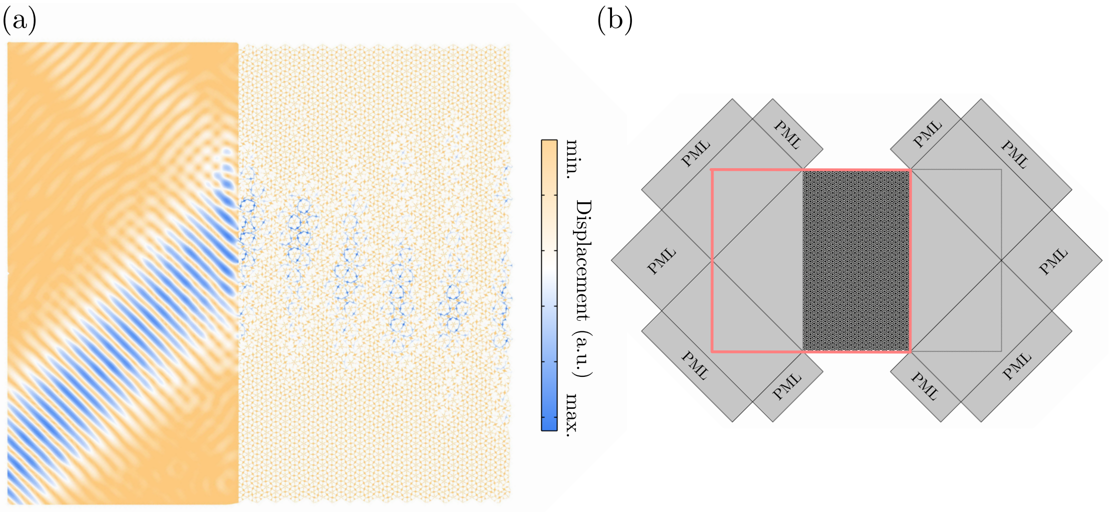

Figure 3.6: (a) Negative refraction of a Gaussian beam. The left domain is defined as an isotropic elastic medium, whereas the right one is a large array of the unit cell of Fig.3.5(a). The Gaussian beam is imposed as a boundary condition of the bottom left corner. (b) Additional domains used to define partially-matched layers. The field of view depicted in (a) is shown as a pink rectangle.

which a negatively-refracted beam is clearly apparent.

To back our claims of broad bandwidth, which are for now based on the large frequency range over which negative group velocity is present, we conduct additional studies at different frequencies. In order to be able to exclude the positively-refracted longitudinal and transverse waves, we use a trick and pin the center of the unit cell to an idealised motionless background, thereby forbidding global translation modes. This procedure leaves the anomalous cone in place, as shown in Fig.3.7(a), allowing us to unambiguously assign any low-frequency wave that crossed an appreciable length of our metamaterial to the anomalous cone. The setup of this series of numerical experiments is depicted in Fig.3.7(c): a slanted metamaterial slab is inserted between two domains of an isotropic elastic medium, which in turn are surrounded by perfectly-matched layers. We impose a monochromatic gaussian beam on the left edge (Fig.3.7(b)), and sweep over frequency.

The beam incoming from the left is refracted at the two metamaterial interfaces, with the beam exiting through the right edge shown in Fig.3.7(d). We then estimate the center of this outgoing beam and plot it for various frequencies in Fig.3.7(e). The only way in which the center position can fall below the dashed line is by being negatively refracted twice. For reference, we repeat the whole process for an elastic locally-resonant metamaterial taken from the negative refraction literature [75], whose band structure is shown in Fig.3.7(f). The corresponding unit-cell geometry, shown as an inset in the same panel, relies on heavy local inclusions that act as the hidden mass mechanism of Fig.1.4(d) to provide effective negative density. The chirality of the couplings connecting this mass to the surrounding matrix provides

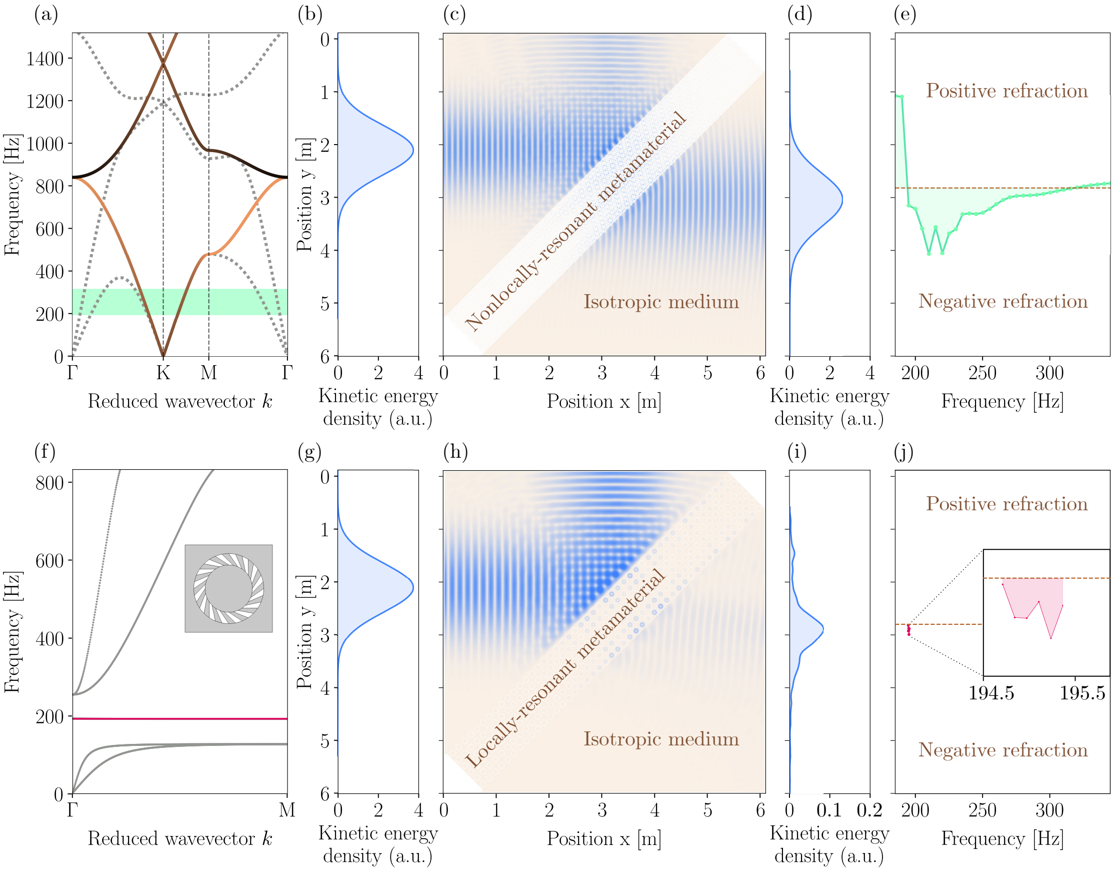

Figure 3.7: Bandwidth of negative refraction for nonlocally-resonant and locally-resonant approaches. (a) Band structure of pinned metamaterial (solid lines) with the unpinned version for reference (grey dashed lines). The negative refraction region for the chosen isotropic material is highlighted in green. (b) Shape of a gaussian beam incoming from the left. (c) Kinetic energy density in an FEM simulation of an istropic medium with density $\rho = 1300$ kg/m^3 and Young's modulus $E = 11$ MPa. (d) Shape of the outgoing beam. (e) Beam center as a function of frequency, with the threshold between negative and positive refraction indicated with a brown dashed line. (f-j) Equivalent panels for a locally-resonant metamaterial, with the negative refraction range indicated in pink and zoomed in in the inset of (j).

Table 3.1: Effective range of negative refraction for various choices of elastic constants of the interfaced isotropic medium.

E [MPa]	18	13	11	10	8	6	5
ρ $[kg/m^3]$	793	1133	1300	1473	1813	2266	2946
$\Delta\omega/\omega_c$ (adim.)	69%	51%	48%	38%	32%	21%	18%

the second ingredient required in doubly-negative metamaterials, namely negative stiffness. The central mass has density $\rho = 8950 kg/m^3$, Young's modulus $E = 211$ GPa and Poisson's ratio $\nu = 0.49$. The surrounding matrix consists of idealised PLA, while the material that connects the internal mass to the surrounding matrix uses the same idealised TPU as the hinges of our nonlocally-resonant metamaterial. We also selected the same width for the locally-resonant and nonlocally-resonant metamaterial slabs.

Comparing the results of these two series of simulations confirms what we expected from the respective band structures of these two metamaterials, namely that our nonlocally-resonant metamaterial exhibits negative refraction over a much larger bandwidth of 48%, compared to the 0.33% of the locally-resonant metamaterial. In the nonlocally-resonant case, other effects start to take over as the limiting factor for negative refraction bandwidth. Indeed, we conducted the same study while varying the elastic constants of the isotropic medium and collected the results in Table 3.1. This shows that the interfaced isotropic medium matters and that the effective negative refraction range does not cover the entire frequency range over which the anomalous cone extends. In our original example, the effective range of negative refraction is highlighted in green over the band structure of Fig.3.7(a). The entire anomalous cone can lead to negative refraction behaviour when interfaced with an appropriate isotropic medium; the choice of the latter simply shifts the effective range of negative refraction. Comparing the outgoing beams of Fig.3.7(d) and Fig.3.7(i), it is apparent that the locally-resonant metamaterial also leads to a higher distortion of the beam profile; we surmise that this is related to its having larger unit-cells.

3.4 Anomalous cones on a field trip in k-space

The highly symmetrical geometries we considered above hosted anomalous cones at the corners of their first Brillouin zones. Must anomalous cones always sit in the corner ? In this section, we prove the opposite with additional examples of anomalous cones at other locations of k-space. We then discuss an inverse design method to shift anomalous cones at target positions.

We begin with another bimodal geometry, whose kinematic graph is shown in Fig.3.8(a), with the corresponding zero-mode shown in Fig.3.8(b). Note that we show a deformed configuration in this figure, with the reference geometry only containing symmetrical, undeformed rosettes like the one in the upper right corner. As earlier, we can deduce the bimodality of

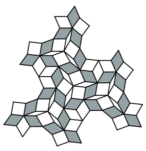

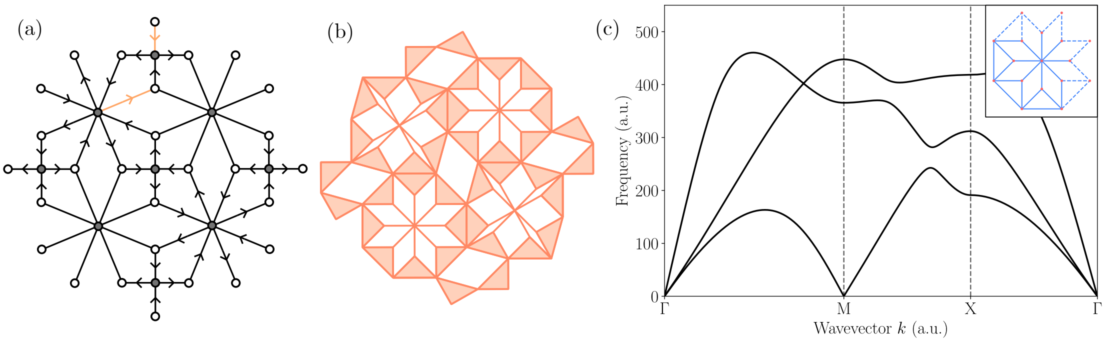

Figure 3.8: Oligomodal geometry with anomalous cones at Γ and M. (a) Graph representation showing that two zero-modes are present. (b) Corresponding real-space deformation. (c) Associated spectrum along high-symmetry lines of the Brillouin zone, computed using a spring-mass model with the unit cell shown in the inset.

the metamaterial from a kinematic graph analysis: fixing two arrows, shown in orange in Fig.3.8(a), is enough to attain a coherent arrow configuration covering the entire plane. We can extract more information from these kinematic graphs: we encourage the reader to try drawing an arrow configuration in which the four-legged kinematic nodes carry no arrow, which we will call configuration Γ. In another compatible configuration, which we will call M, the four-legged kinematic nodes have twice as many arrows per edge than their eight-legged counterparts. As a hint, note that the configuration shown in Fig.3.8(a) is neither the Γ nor the M configuration, but a linear combination of the two.

Our choice of names for these arrow configurations is not innocent: indeed, the M arrow pattern repeats itself every second unit cell in both directions, which corresponds exactly with the Bloch wavevector at the M point. As for the Γ arrow pattern, it has a periodicity of a single unit cell, meaning that the inter-cell phase is zero. This is compatible with the Γ point. The kinematic graph analysis therefore predicts two anomalous cones, one at the corner of the first Brillouin zone and the other at its center. The band structure shown in Fig.3.8(c), which we obtained from a spring-mass model, confirms this insight: anomalous cones can also occur at other symmetric points of the Brillouin zone.

Can we go away from symmetry points ? In Fig.3.9(a), we show another oligomodal tiling. One of the associated arrow configurations, shown in Fig.3.9(b), has a periodicity compatible with the wavevector $\vec{k}L = (0, 2\pi/3)^T$. Computing the spectrum confirms the presence of an anomalous cone at this location, as can be seen in the first band depicted in Fig.3.9(c). This time, we have eight independent modes: two at K and K', and six along the symmetry lines connecting Γ to the M points. This time, we broke free from symmetric points but stayed on a symmetry line.

In the last example of this chapter, we modify the geometry given in Fig.3.8 to shift the M-point anomalous cone to a non-symmetric target location, here $\vec{k}_{targ} = (3\pi/4, \pi/2)^T$. The computational details of this inverse design procedure are presented in Appendix B; here,

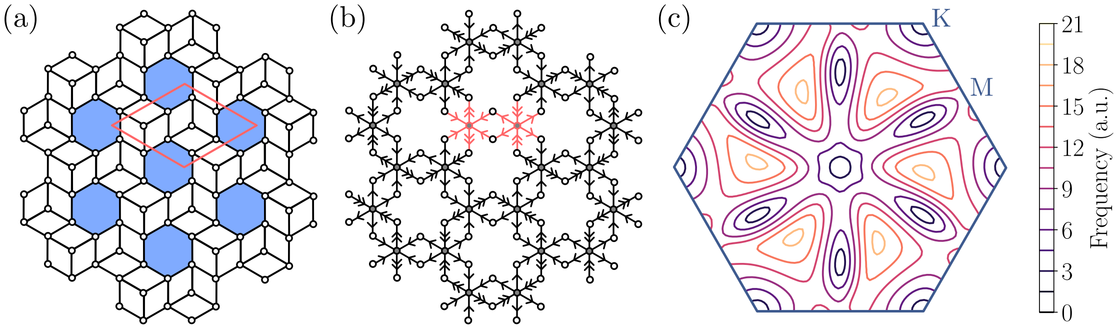

Figure 3.9: A geometry exhibiting anomalous cones away from the points of highest symmetry. (a) Idealised mechanism, with rigid bars in black, hinges as white disks and rigid domains in blue. The pink quadrilateral corresponds to a possible choice of unit cell. (b) Corresponding kinematic graph, with the edges associated to the unit cell highlighted in pink. (c) Isofrequency contours of the first band over the first Brillouin zone.

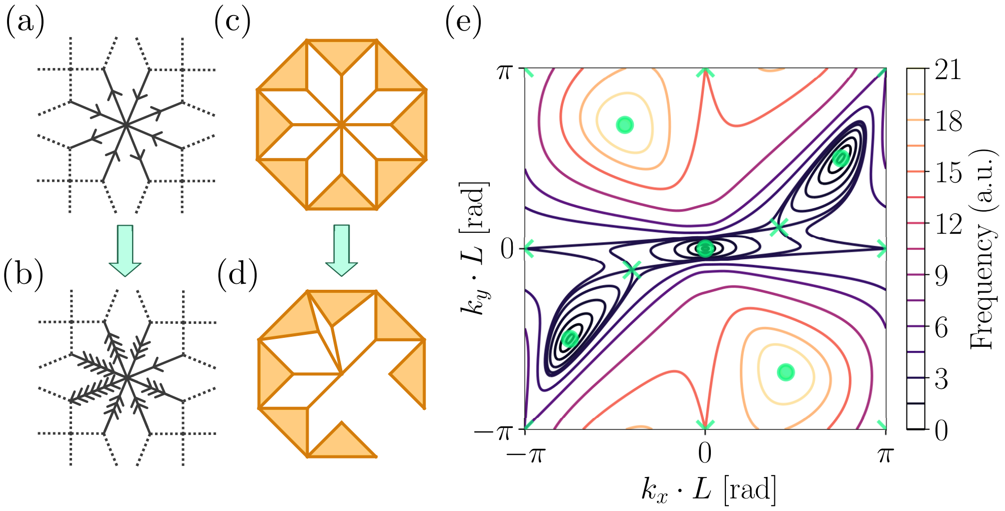

Figure 3.10: Moving an anomalous cone to an arbitrary location in k-space. (a) Initial oligomodal geometry. (b) Graph representation of corresponding zero-mode. (c) Modified geometry and (d) representation of one of the associated mechanical degrees of freedom. (e) Isofrequency contours of the first band over the first Brillouin zone, with critical points indicated in green.

we present the logical flow of the inverse design process. This inverse design method works as follows: in order to have an anomalous cone at the desired k-space location, we need a kinematic node whose arrow-drawing rule is compatible with the specified Floquet-Bloch boundary conditions, which must also apply at the graph level. Concretely, instead of the original arrow rule of Fig.3.10(a), we need the arrow rule of of Fig.3.10(b)[V]. Having found this abstract graph representation from the Bloch condition, we still need to find a concrete geometry whith the same arrow rule.

We start from the initial geometry of Fig.3.10(c) and allow ourselves to modify internal geometric parameters of the unit cell. We need to modify at least two, since our hope is to move the anomalous cone within a two-dimensional k-space. Using the area law and kinematic graph rules exposed in Ch.2, we can then compute the arrow rule *as a function of the free geometric parameters*. So far, so good, but there is a slight problem with this approach, relating to the states of self-stress that muddled the Maxwell count of the zero-modes in Eq.(2.2). Indeed, the high symmetry of the initial geometry (Fig.3.10(a)) makes some of the bar constraints redundant; a naïve Maxwell count would deduce that no zero-modes are present. However, symmetry-induced states of self-stress (such as the one depicted in Fig.2.1(d)) appear, correcting the modal count and allowing zero-modes to exist. Generic modifications of the internal geometry of the cell then frustrate the mechanism, removing both the states of self-stress and the zero-modes. In Ch.5, we will discuss the spectral signature of such frustrated mechanisms, among other gap-related topics.

We therefore remove some rigid links, to relax the constraints and avoid mechanical frustration. One way to to this is depicted in Fig.3.10(d); note this crescent-shaped unit cell has irregular internal angles between its central bars. These angles are the free geometric parameters used in the inverse design procedure. We can then conduct the final step of the procedure: we invert the map between the geometric parameters and the arrow weights, which allows us to compute internal angles compatible with the arrow weights of Fig.3.10(b). Remembering that these weights were in turn determined through the Floquet-Bloch boundary condition, the resulting geometry should host an anomalous cone at the target location. To confirm this, we compute the spectrum associated to a spring-mass model with the same geometry. Plotting equifrequency contours of the lowest branch of the spectrum over the first Brillouin zone (Fig.3.10(e)) indeed reveals an anomalous cone at the desired location of k-space. Naturally, its time-reversed twin at $-\vec{k}_{targ}$ must also be present [VI].

In this chapter, we used our kinematic graph theory to design flexible metamaterials that host nonlocal resonances. We demonstrated that such nonlocal resonances are associated to anomalous dispersion cones, and explored the unusual physical effects associated to these cones with a combination of spring-mass models and full-wave simulations. Finally, we

---

[V] Note that for a generic choice of Bloch wavevector, the required arrows no longer come in integer numbers; we would need to write these non-integer weights next to the arrows to keep track.

[VI] We note in passing that the critical points respect the Poincaré-Hopf theorem on a torus: there are $N_{min} = 3$ minima, $N_{max} = 2$ maxima and $N_{sad} = 5$ saddle points, which indeed yields $N_{min} + N_{max} - N_{sad} = 0$.

provided several examples of anomalous cones at increasingly less symmetrical locations, culminating in an inverse design method that allows us to move cones around in k-space by deforming geometries in a rational way.

4 Experimental Validation

> *"I am never content until I have constructed a mechanical model of the subject I am studying. If I succeed in making one, I understand; otherwise I do not."*
> — William Thomson (Lord Kelvin).

Our dynamical models and full-wave simulations in Ch.3 brought the sudoku-like drawings of Ch.2 a few steps closer to reality. Here, we go further and dip our metaphorical toes in the experimental pool. We begin by experimentally validating the presence of global deformation modes in 3D-printed flexible metamaterials by means of uniaxial compression experiments. In these experiments, we consider a bimodal geometry and a quasicrystalline one. We then discuss the possibility to use oligomodal metamaterials to achieve mechanical multifunctionality, illustrating it with a material whose Poisson's ratio can switch from positive to negative under varying strain rate.

Having confirmed that the kinematic underpinnings of our theory are reasonable, we will then turn to its dynamical aspects. In the second part of this chapter, we seek to confirm the presence of the anomalous cones predicted by our kinematic graph theory. To that end, we conduct vibration experiments on a 3D-printed nonlocally-resonant metamaterial. We scan this 3D-printed sample with a laser Doppler vibrometer and process the measured velocity fields to obtain experimental equifrequency contours, which indeed indicate the presence of the anomalous dispersion cones predicted by our kinematic graphs and subsequent spring-mass models.

4.1 Actuating soft modes through uniaxial compression

We now seek to implement the idealised geometries of Ch.2 in practice. As we discussed previously in the context of FEM simulations, realistic oligomodal metamaterials require hinges of finite size. The design of these hinges is crucial; they should provide close approximations[I] of

---

[I] Consult [222] for the impact that non-ideal hinges have on flexible metamaterials.

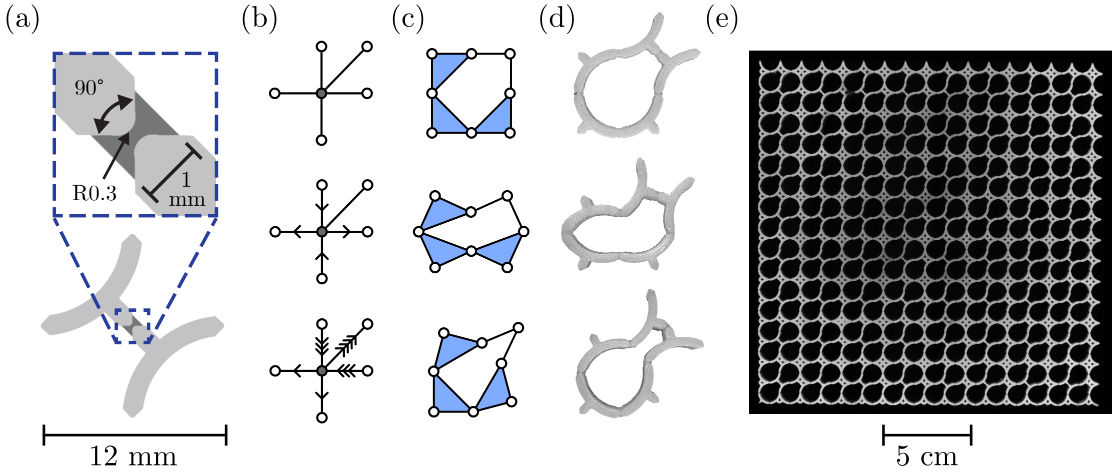

Figure 4.1: 3D-printing oligomodal metamaterials. (a) Geometry of the building blocks, with details of the flexible hinges in the inset. The dark areas are 3D-printed with a soft viscoelastic resin (Stratasys Agilus 30), whereas the lighter areas are printed with a rigid material (Stratasys VeroWhitePlus). (b) Shape of the abstract hinge node we seek to implement, with two mechanical degrees of freedom. (c) Corresponding ideal geometry. (d) 3D-printed implementation with the blocks depicted in (a). (e) Complete 3D-printed oligomodal tiling.

the idealised hinges employed in the kinematic graph theory. The two main design requirements are that these hinges should bend for a minimal cost in elastic energy, while also not stretching easily in either direction. In Fig.4.1(a), we present such a hinge design. It relies on a combination of two materials to achieve low bending energy: a soft material (Stratasys Agilus 30) is inserted between more rigid domains (Stratasys VeroWhitePlus). Stretching motions are made more costly by adding lateral tapering of the soft material.

Using these hinge elements, we then seek to implement the abstract kinematic graphs of Fig.4.1(b) in a 3D-printed unit-cell. Such a cell is represented in Fig.4.1(d); it indeed admits bending motions that closely match those of our idealised unit cell, represented in Fig.4.1(c). We then 3D-print a 16 × 16 cells metamaterial using a Stratasys Objet500 Connex3 3D printer. The result is shown in Fig.4.1(e). For this first realisation of an oligomodal metamaterial, we experiment with a slightly frustrated variant of the quadrimodal structure shown in Fig.2.9. This variant hosts two global zero-modes instead of four. In the quadrimodal version depicted in Fig.2.9, two sets of hourglass-shaped elements are visible, with differing orientations. Compare this with Fig.4.1(e), wherein only one hourglass orientation remains. Frustrating the motion of one of these sets of mechanical elements reduces the zero-mode count from four to two.

Having successfully manufactured our metamaterial sample, we place it vertically between two laser-cut Plexiglas textured boundaries, with indenters spaced by two lattice constants. We then compress the sample uniaxially using an Instron 5943 with a 500-N load cell. The resulting deformation mode depends on whether the textured boundaries are aligned or

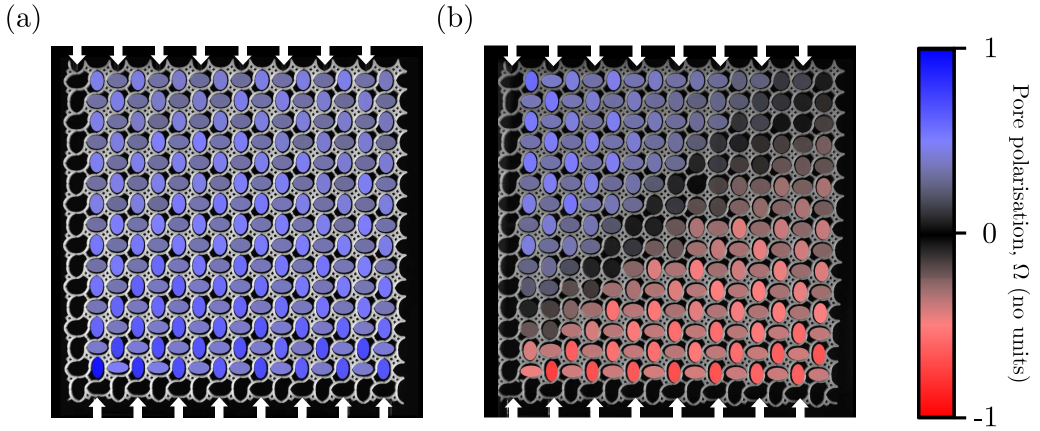

Figure 4.2: Textured compression revealing the two independent soft modes, with the indentation points indicated by white arrows. (a) Counter-rotating squares mode, with its alternating elliptic pores. (b) A nontrivial second zero mode, with two domains of opposite pore polarisation separated by a neutral layer.

anti-aligned; indeed, for an even number of cells, anti-aligned indenters correspond to the kinematic graph of Fig.2.8(c). On the other hand, aligned indenters favor the kinematic graph of Fig.2.9(c).

To obtain quantitative results, we film the compression process with a 3858×2748 monochrome CMOS camera (Basler acA3800-14um), equipped with a 75 mm lens (Fuji-non). This results in a spatial resolution of 0.07 mm. The filmed deformation patterns, shown in Fig.4.2, are then quantified using a Python image processing library (OpenCV). First, we fit an ellipse to every pore. Then, we extract the associated ellipticities to construct a measure of pore polarisation, $\Omega := (-1)^{n_x+n_y} f \cos 2\phi$ [223]. Ω measures the alignment of every ellipse with the counter-rotating squares pattern, in which pores alternate between two opposite ellipticities. In Fig.4.2(a), we see that anti-aligned textured compression leads to a good agreement with the predicted counter-rotating squares pattern. In Fig.4.2(b), the aligned textured indenters instead favour the second soft-mode of the metamaterial, leading to two domains with opposing pore polarisations separated by a low-deformation diagonal layer. For large deformations, a geometric nonlinearity kicks in, and the profile saturates at a constant value, leading to counter-rotating squares domains separated by a linear-gradient region in which the kinematic graph analysis remains valid.

We then turn to another intriguing geometry, namely the quasicrystalline one of Fig.2.10. We 3D-print and characterise it with the methods described above. In order to make the mode hierarchy predicted by kinematic graph theory visible, we simply change the orientation of the sample by 45° and laser-cut a different set of Plexiglas indenters, corresponding to the white arrows of Fig.4.3. Again, the observed deformations are consistent with the predictions of kinematic graph theory: compare Figures 2.10 and 4.3. The two compression experiments we discussed above confirm that the two new zero-mode scaling classes we uncovered in Ch.2,

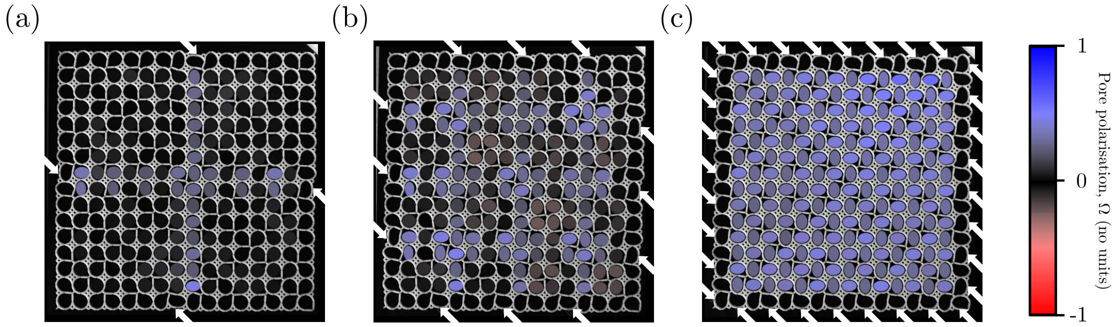

Figure 4.3: Textured compression confirming the presence of three soft modes at different spatial scales in a 16 × 16 quasicrystalline flexible metamaterial, with the indentation points and directions indicated by white arrows. (a) The largest-scale cross mode. (b) An intermediate-scale mode. (c) The counter-rotating squares mode.

namely the logarithmic and oligomodal classes, can be realised in practice.

From a mechanical perspective, such oligomodal geometries provide an interesting middle-ground between controlled motion and floppiness. The presence of a limited number of global deformation patterns could be leveraged to achieve mechanical multifunctionality. One strategy towards this goal is to turn the unavoidable actuation cost of real hinges to our advantage. We can start by identifiying a subset of the hinges that is actuated to a lesser degree (ideally not at all) in one of the modes. We might call these hinges the discriminant hinges. In the structure of Fig.4.1(e), these would be the hourglass hinges, which are not actuated at all in the counter-rotating squares mode. In this mode, the hourglasses behave as rigid squares. Our design path to multifunctionality is then to make the actuation cost of discriminant hinges dependent on some external property: this could be a magnetic field, temperature, basically any external condition in which we want our material to behave differently. Multiple studies sought to create metamaterials with reconfigurable properties [224–227]. Oligomodal geometries could prove to be a useful tool in that line of research, by more finely constraining the set of global DOFs among which reconfiguration takes place.

To validate this design strategy, my collaborator D. Dykstra and I decided to use the strain rate as a mode-selection parameter. To selectively actuate the discriminant hinges and therefore choose the deformation mode, we set out to leverage the strain-rate dependency of viscoelasticity [223, 228, 229]. To properly model the mechanical responses of viscoleastic materials, Hooke's law must be extended by including viscous elements governed by the equation $\sigma = \eta\dot{\epsilon}$.

After learning from our mistakes in some common initial experiments, David conducted a definitive series of simulations and experiments validating this approach to mechanical multifunctionality, which I report in here in Fig.4.4 as a further vindication of kinematic graph design. The manufacturing step required three different materials: as shown in Fig.4.4(a), the rigid elements (Stratasys VeroWhitePlus) and viscoelastic hinges (Stratasys Agilus 30) were 3D-printed simultaneously with a Stratasys Objet500 Connex3 3D printer. The discriminant hinges

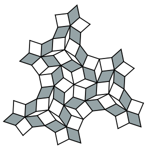

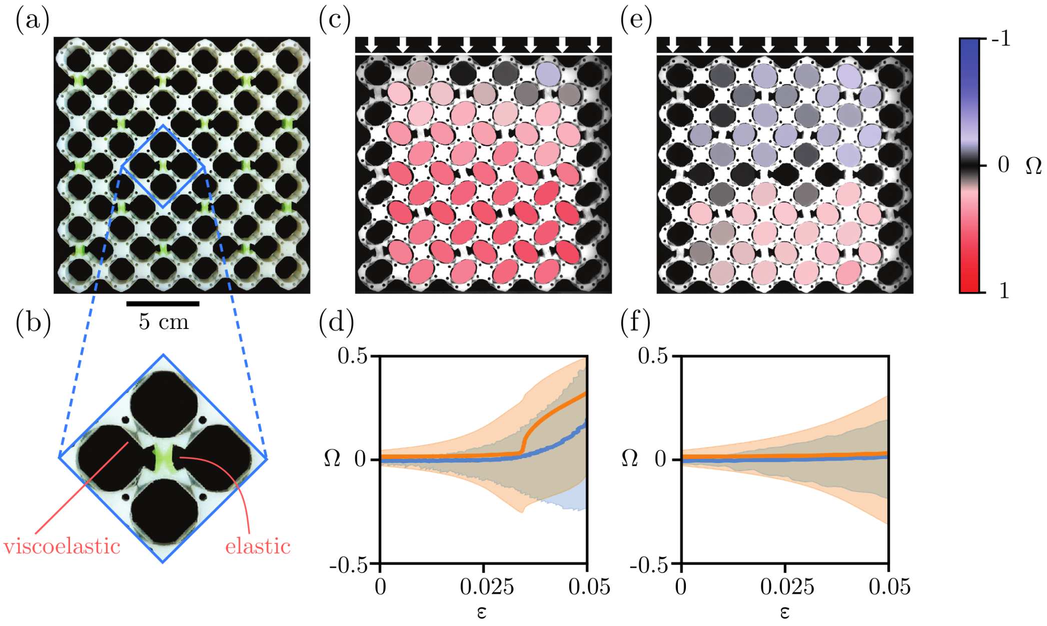

Figure 4.4: Mode selection by strain rate (Experiment by D. Dykstra). (a) 61-cell oligomodal metamaterial obtained by a combination of 3D-printing and resin curing. (b) Detail of the hinge geometry, with the different materials labeled. (c) Slow uniaxial compression (with $\epsilon = 0.056$ and $\dot{\epsilon} = 9.3{\cdot}10^{-6}$ Hz) with a non-textured surface, with the pore polarisation Ω colored. (d) Evolution of the average pore polarisation Ω as a function of strain ϵ, with experimental results in orange and numerical results in blue. The average is taken over all the pores at a given strain value. The shaded areas indicate the variance of pore polarisation. (ef) Same experiment at a faster strain rate ($\dot{\epsilon} = 0.11$ Hz).

added later, by curing an elastic rubber (Zermack Elite Double 32). David then conducted uniaxial compression experiments in an Instron 5943 testing device, without using a textured indenter.

A slow compression at strain rate $\dot{\epsilon} = 9.3 \cdot 10^{-6}$ Hz resulted in the domination of the counter-rotating squares mode, as shown in Fig.4.4(c). Probing this qualitatively with the average pore polarisation $<\Omega>$ resulted in Fig.4.4(d), which indicates that alignment with the counter-rotating squares pattern dominates. In this situation, the metamaterial behaves as an auxetic, since its lateral dimension decreases as we compress it: we have $\nu < 0$.

Repeating the experiment at a faster rate of $\dot{\epsilon} =$ yielded the results of Fig.4.4(ef), which are dominated by the second zero-mode of the kinematic graph theory (note that the geometry has been turned by 45° in these experiments). This is also reflected in the vanishing average pore polarisation. Indeed, we have $<\Omega>= 0$ when the second mode dominates, because the two domains of opposing polarities compensate each other. Crucially, the presence of a zero-deformation band in the center prevents auxetic behaviour. Non-ideal hinge deformations take over as the dominant Poisson's ratio mechanism, and we reach a positive Poisson's ratio. Hence, we can effectively switch the sign of Poisson's ratio based on strain-rate, which constitutes a form of mechanical multifunctionality enabled by oligomodality.

In this section, we saw that current 3D-printing technology allows us to build oligomodal metamaterials with hinges flexible enough to observe the kinematic DOFs discussed at length in Ch.2. We demonstrated that our kinematic graph theory correctly predicted the deformation patterns in an oligomodal metamaterial and the hierachical deformation patterns of a quasicrystalline geometry. We also introduced a design path towards mechanical multifunctionality, in which the sparsity of global DOFs that characterises oligomodal geometries is leveraged to obtain well-defined but still reconfigurable mechanical responses. Concretely, we could use strain-rate to selectively actuate different modes, which were in turn associated to different Poisson's ratios. In other words, we could select the sign of Poisson's ratio depending on how fast we compressed our oligomodal metamaterial.

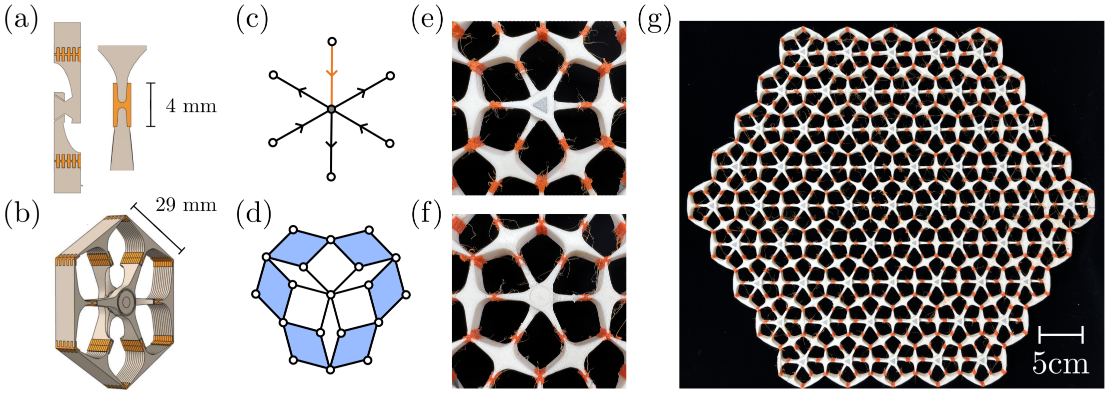

Figure 4.5: 3D-printed nonlocally-resonant metamaterial. (a) Detail of the hinge geometry as seen from an in-plane and an out-of-plane direction. Orange sections are printed with a soft material (TPU) whereas the brown sections are printed using a rigid material (PLA). (b) 3/4 view of the unit cell. (c) Corresponding abstract DOF. (d) The same DOF on an idealised geometry. (ef) Actual 3D-printed cell, seen from above and below. (g) Complete 61-cell 3D-printed sample.

4.2 Catching nonlocal resonances through vibrometry

We now feel confident enough to try capturing some anomalous cones in the wild. For this endeavour to be successful, we again need a good hinge design; we use another variant of tapered soft hinge (orange), shown from the side and the top Fig.4.5(a). In the side view, we note that we used a layered design to increase the contact surface with the rigid material (beige). This choice was made to increase adhesion between the two materials. In Fig.4.5(b), we show the full unit-cell, which slightly differs from the one employed in the numerical simulations of Ch.3 with the introduction of a central, freely-rotating hub element replacing the six-legged central hinge. This helps in limiting the mechanical degrees of freedom of the cell to the ideal case represented in graph form in Fig.4.5(c) and in mechanism form in Fig.4.5(d). We then 3D-print a 61-cell sample using a dual-extruder 3D-printer (Raise3D Pro2).

Figures 4.5(e) and (f) show close-up top and bottom view of a single unit cell. The white elements were printed using a rigid polyactic acid (Raise3D PLA), with a Young's modulus of $E = 2636 \pm 330$ Mpa (value provided by manufacturer). As for the orange elements in the hinges, they were printed using a much softer elastic filament, namely a thermoplastic polyurethane (NinjaFlex TPU) with a Young's modulus of $E = 12$ MPa (value provided by manufacturer). In Fig.4.5(e), a small triangular patch of retroreflective tape is also visible. Three such patches were added to every unit cell to help with the signal-to-noise ratio of the laser vibrometry measurements.

The full 61-cell lattice is shown in Fig.4.5(g). Because the dimensions of the printing bed of the Raise3D Pro2 are 30 × 30cm, we had to assemble three diamond-shaped 20-cell patches manually. The assembly points all lie within rigid elements. We aligned the PLA faces that had to be joined by inserting small metallic wires as guides, which allowed the sample to hold together. Droplets of epoxy resin were then inserted between the faces. The epoxy filled the small interstitial space between the PLA faces by capillarity; after it cured, we sanded down potential excess to limit the amount of additional mass.

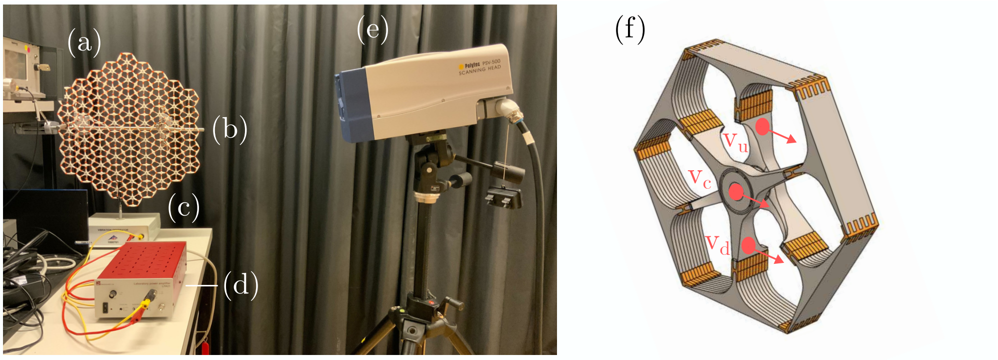

Figure 4.6: Experimental setup of the laser vibrometry measurement. (a) 61-cell 3D-printed metamaterial sample. (b) Bars holding the sample in a vertical position. (c) Shaker (3B), attached to a cell on the edge. (d) Amplifier (Newtons4th LPA01) feeding the vibrometer signal to the shaker. (e) Scanning laser vibrometer (Polytec PSV 500) placed at a grazing angle of 26°. (f) Locations of the three velocity measurement points on the unit cell.

For the ensuing vibrometry experiments, we used the setup pictured in Fig.4.6. The metamaterial sample (Fig.4.6(a)) was held vertically by introducing metallic bars through two pores and then securing a rigid element to the bar of Fig.4.6(b) with a zip tie. The scanning laser vibrometer (Polytec PSV 500, Fig.4.6(e)) was placed next to the sample, with a line of sight almost parallel to the sample, in order to measure in-plane velocities. This line of sight formed a grazing angle of 26° with the plane of the metamaterial, in order to be still be able to scan the surface of the sample. Vibrations in the sample were excited with a shaker (Fig.4.6(c)) placed directly underneath and rigidly fastened to a rigid part of the metamaterial. The input signal was provided to the shaker by the vibrometer, with an intermediate amplifier stage (Newtons4th LPA01, Fig.4.6(d)). This signal consisted in pseudorandom noise involving 1250 frequency lines between 10 Hz and 1250 Hz. We defined 183 scanning points, *i.e.* three per unit cell, positioned on retroreflective patches at the locations indicated in Fig.4.6(f).

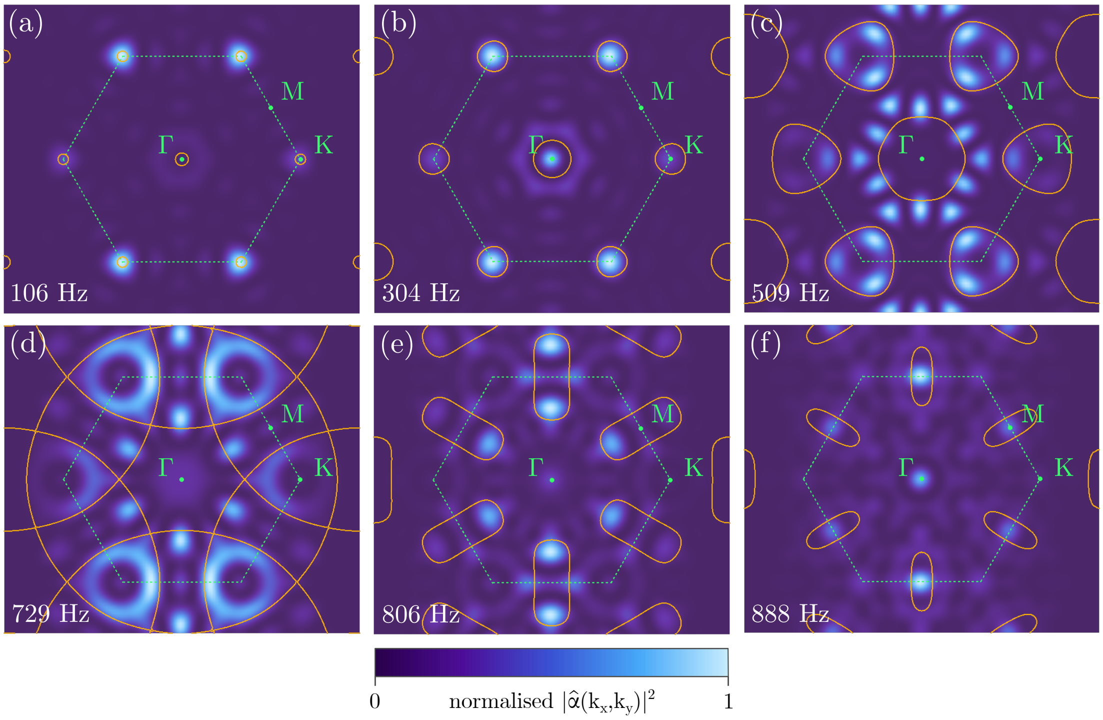

Figure 4.7: FFT of experimentally obtained $|\alpha|^2$ (blue colours) with superimposed theoretical isofrequency contours of the first band (orange lines) at (a) 106 Hz, (b) 304 Hz, (c) 509 Hz, (d) 729 Hz, (e) 806 Hz and (f) 888 Hz. The boundaries of the first Brillouin zone are indicated with a dotted green line, with some symmetry points labeled.

These three velocities allow us to construct a proxy measuring the degree of actuation of the internal mechanism of each cell, $\alpha := 2v_c - v_u - v_d$. For three equal velocities, the mechanism is not actuated and we have $\alpha = 2 \times v - v - v = 0$. If the cell is rigidly rotating, we also have $\alpha = 2 \times 0 - v + v = 0$. The only remaining possibility is that the central patch moves out of phase with the upper and lower patch, meaning that α indeed constitutes a proxy of cell mechanism actuation[II]. We therefore obtain 61 data points representing mechanism actuation accross the lattice at each measured frequency. In order to excite a large variety of k-vectors, we then repeated the experiment for multiple attachment points of the shaker. Padding the resulting image with zeroes and conducting a 2D fast Fourier transform (FFT) yields the blue density maps depicted in Fig.4.7, on which we superimposed the isofrequency contours predicted by the spring-mass model of Eq.(3.8), which we now discuss.

In Fig.4.7(ab), we observe a clear concentration of energy at the K and K' points at 106 and 304 Hz, as expected from the dynamical models and graph prediction. As in the FEM simulations, a mass gap is present: for frequencies below 106 Hz, energy does not accumulate at the Brillouin zone corners.

[II] The two remaining independent degrees of freedom could similarly be captured in a translation and a rotation proxy.

Going up in frequency, we consider the f = 509 Hz isofrequency contours presented in Fig.4.7(c). There, we see the anomalous cones opening up into triangular contours. The same anisotropy is present in our simple spring-mass model. If we keep going, we reach a point (at f = 729 Hz) at which the anomalous cones merge with the central transverse cone, as shown in Fig.4.7(d). In terms of negative-index relative bandwidth, we note in passing that this yields $\Delta\omega/\omega_c$ = 149%, a number higher than any point we collected in our state-of-the-art of Fig.1.5. Past that point, we get the elliptical contours that characterise the higher-frequency parts of the first dispersion branch of our nonlocally-resonant metamaterial. This can be seen in 4.7(e), where elliptical contours progressively enclose the M points of the Brillouin zone. In Fig.4.7(f), in f = 888 Hz, the energy finally accumulates onto the M points; we reached the top of the transverse-anomalous branch.

The agreement between the spring-mass contours and the experimental results remains surprisingly good up until the upper end of the anomalous branch, given the wildly different internal structures of the ideal and real versions of our nonlocally-resonant metamaterial. It is consistent with the presence of anomalous cones in the vibration spectrum of our 3D-printed metamaterial, in line with the simulation results discussed in Ch3. As was the case with FEM simulations, the main difference between the spring-mass model and the experimental results consists in the emergence of a mass-gap: the band accumulates at the K points at a finite frequency of 106 Hz. The ubiquity of these small gaps practically imposes the theme of the next chapter, which will be dedicated to gaps in nonlocally-resonant metamaterials and the various ways in which they can arise.

5 Opening Gaps

"Und wenn du lange in einen Abgrund blickst, blickt der Abgrund auch in dich hinein."
— F. Nietzsche
"And when you gaze into a gap for too long, the gap also gazes into you."
— Own translation

In the previous chapters, we got acquainted with anomalous cones and their peculiar physical properties. We also gained confidence in their physical relevance, on the basis of full-wave simulations and experimental data. The next logical step to deepen our understanding of these objects is to follow an age-old scientific methodology; in this chapter, we break anomalous cones apart.

In Sec.5.1, we do so by introducing additional couplings that either frustrate or favour the nonlocal resonance. Such couplings respectively induce mass gaps and momentum gaps at the basis of the anomalous cone. In Sec.5.2, we frustrate the nonlocal resonance even earlier, at the kinematic graph level. Finally, in Sec.5.3, we investigate the upper ends of the anomalous cones, by looking at their hybridisation properties and the resulting higher-frequency bandgaps. In doing so, we also learn how to deform anomalous cones.

5.1 Gaps induced by additional couplings

In the full-wave simulations of Ch.3 and the 3D-printed samples of Ch.4, we saw that introducing realistic hinge geometries led to the emergence of mass gaps at the basis of anomalous cones. The shape of the hinge and the materials composing it determine the energetic cost associated with its actuation, which in turn determine the height of the mass gap. Here, we model this phenomenon by inserting additional springs that frustrate the mechanism; in our minimal chain model, the vertical grey springs depicted in Fig.5.1(a) play this role. As shown with yellow arrows in Fig.5.1(b), these springs induce restoring forces that oppose the zero-mode; accordingly, this zero-mode becomes a soft mode. The original anomalous

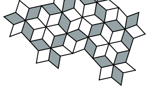

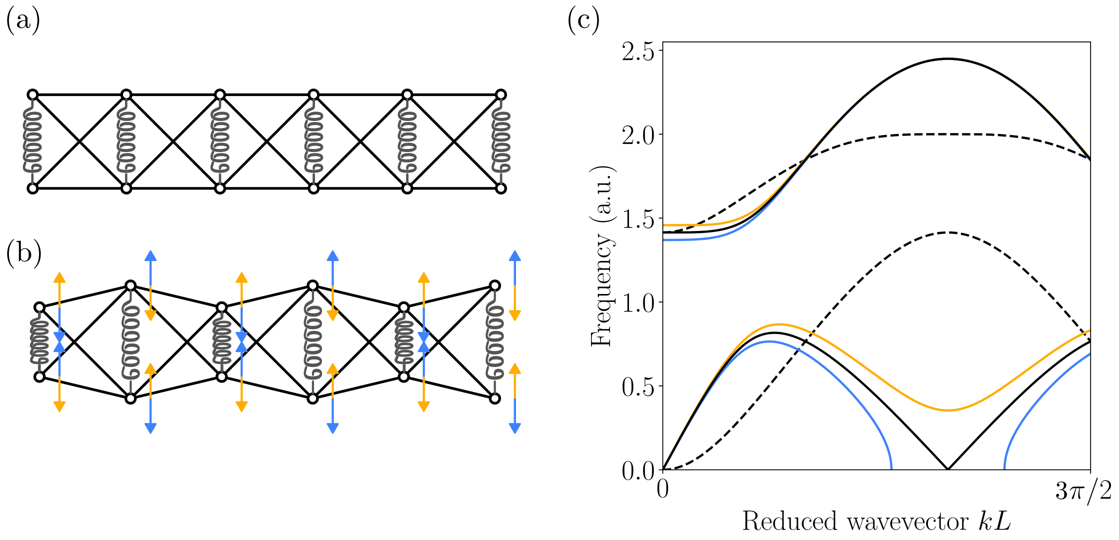

Figure 5.1: Anomalous cones as mass-gap to momentum-gap transition. (a) Minimal chain model with an additional weak springs lifting the zero mode. (b) Corresponding spectrum, with asymmetric branches as dashed lines and symmetric branches as solid lines. The black lines correspond to a model without the frustrating spring. The yellow line corresponds to a frustrating spring with positive stiffness, whereas the blue lines correspond to an instability-inducing negative stiffness. (c) Representation of the zero-mode at the edge of the Brillouin zone, with the restoring forces induced by a positive spring in yellow and the instability-driving forces of a negative spring in blue.

cone, drawn in black in Fig.5.1(c), becomes gapped, yielding the yellow curve instead. The symmetrical sector of the dynamical matrix is now given by

$$\mathscr{D}_S(\phi) = \begin{pmatrix} 3-\cos(\phi) & -i\sin(\phi) \\ i\sin(\phi) & 1+\cos(\phi)+2\zeta \end{pmatrix}, \tag{5.1}$$

where ζ denotes the stiffness of the additional frustration spring. Since $\mathscr{D}_S$ becomes diagonal at $\zeta = 0$, it is immediately apparent that the height of the mass-gap is simply proportional to ζ. This provides a first hint of connection to the roton concept: by frustrating nonlocal resonances, one can get roton-like dispersions of any depth. However, the underlying mechanism is quite different: the long-range couplings that are central to the roton metamaterial approach require three spatial dimensions, so they cannot be realised in a planar setting. We need to wait until the introduction of elastic IWMs in Ch.7 to pursue the connection of rotons and nonlocal resonances further.

We can also reverse the logic and consider a perturbation that favours the mechanism, in the form of springs with negative stiffness $\zeta < 0$. This could arise through other physical phenomena present in the system, for instance through an electromagnetic instability. Alternatively, such active elements could be introduced by design, following the logic of active media [230–233]. Temporarily straying from our main narrative, we now provide a few bibliographical leads to readers that would like to pursue that research line. Active media were first motivated by considerations rooted in non-hermitian quantum mechanics [234–239], following a realisation that the hermiticity axiom was not necessary to obtain real spectra. Instead, a certain balance between gain and loss elements is required. Subsequent studies clarified the interplay of gain and loss with causality, locality [240–243] and nonreciprocity [244–247]. As it matured, this subfield also started exploring its interactions with other wave phenomena, such as negative refraction [232, 248] and topological edge states [249, 250]. The most recent avatars of active media arguably consist in continuum field theories that forgo energy conservation [251–253]. Such theories include odd viscosity and odd elasticity, which provide tools to describe a large variety of situations ranging from the motion of starling flocks to elastic media with active inclusions, like the negative-stiffness springs of Figures 5.1 and 5.2.

Such active springs induce forces that favour the zero-mode, shown as blue arrows in Fig.5.1(b); the anomalous cone breaks down in a different way, shown as a blue curve in Fig.5.1(c). The cone is now replaced by another type of gap typical of active and time-modulated media, namely a *momentum gap*. In this case, a range of wavevectors centered around the basis of the original anomalous cone are no longer associated to propagating oscillatory eigenmodes. There, the frequency becomes purely imaginary; the associated modes have a fixed spatial profile whose amplitude grows or decays exponentially in time. Modes are also no longer exactly orthogonal.

At the edge of the momentum gap, these two eigenmodes even collapse in a type of non-hermitian degeneracy known as an exceptional point. Solving $|\mathscr{D}_S(\phi)| = 0$ yields the condition $\cos\big(\phi\big) = -3\zeta - 1$[I]. Inserting this in Eq.(5.1), we get

$$\mathscr{D}_{S,0} := \mathscr{D}_S(\arccos(-1-3\zeta)) = \begin{pmatrix} 9\zeta+6 & \sqrt{9\zeta+6}\sqrt{\zeta} \\ -\sqrt{9\zeta+6}\sqrt{\zeta} & -\zeta \end{pmatrix}. \tag{5.2}$$

To see the exceptional point, let us go over to a first-order formulation of the dynamics by defining $\vec{v} = \partial_t \vec{u}$ and rewriting the equation of motion as

$$\partial_t \begin{pmatrix} \vec{u} \\ \vec{v} \end{pmatrix} = H \begin{pmatrix} \vec{u} \\ \vec{v} \end{pmatrix} := \begin{pmatrix} & \mathbb{1} \\ -\mathscr{D}_{S,0} & \end{pmatrix} \begin{pmatrix} \vec{u} \\ \vec{v} \end{pmatrix}. \tag{5.3}$$

This extended dynamical matrix is not diagonalisable! Indeed, it has the eigenvalue zero

---

[I] In particular, this implies that for small ϕ, the width of the momentum gap scales as $\sqrt{\zeta}$.

with an algebraic multiplicity of two, but a geometric multiplicity of one. We can see this explicitly by building the associated Jordan chain: first, note that the zero-mode is given by $\vec{u}_0 := (\sqrt{\zeta}, -\sqrt{9\zeta+6})$. This directly provides an eigenvector $\vec{q}_0 = (\vec{u}_0, \vec{0})^T$ of H such that $H\vec{q}_0 = 0$. As an extended eigenvector, we can then pick $\vec{p}_0 = (\vec{0}, \vec{u}_0)^T$, which satisfies $H\vec{p}_0 = \vec{q}_0$. We will refer to the subspace spanned by this Jordan chain as the zero-mode sector. Since H has two other distinct nonzero eigenvalues, our Jordan chain stops there: the zero-mode sector is two-dimensional, but contains a single eigenmode.

This particular type of degeneracy, in which the eigenvectors collapse as well, is known as an exceptional point. Temporal evolution at such points has interesting features: restricting our analysis to the zero-mode sector and going over to the Jordan basis, we can easily compute the time evolution operator as

$$H_J = \begin{pmatrix} 0 & 1 \\ 0 & 0 \end{pmatrix} \to U_J(t) = e^{H_J t} = \mathbb{1} + H_J t, \tag{5.4}$$

since $H_J^2 = 0$. At this point, the time evolution operator exhibits a slower growth than within the momentum gap. This peculiar growth takes the form of a linear dependency on time: we have $U_J(t)\vec{q}_0 = \vec{q}_0$ and $U_J(t)\vec{p}_0 = \vec{p}_0 + \vec{q}_0 t$. This means that any velocity fluctuation within the zero-mode sector will produce a linearly-growing displacement that aligns with the zero-mode $\vec{u}_0$. If one starts actuating this zero-mode, no restoring force is there to make it spontaneously come back. Modes in the immediate vicinity of the exceptional point behave in a very similar manner, since their modes are also far from being orthogonal[II].

Expanding our discussion to two dimensions, we equip the auxetic metamaterial of Fig.1.7(e) with negative springs favouring the nonlocal resonance. The spring locations and resulting first band are shown in Fig.5.2(a) and Fig.5.2(b-f), respectively. In the latter panels, we observe the emergence of instability pockets with purely imaginary spectrum around the wave-vectors favoured by the negative springs. Like in the one-dimensional case, the edges of these imaginary-frequency pockets consist of exceptional points. As we increase the value of the negative stiffness, more and more wave-vectors are drawn into these islands of instability. At the threshold $\zeta = 1$, they connect, as seen in Fig.5.2(d). At this threshold, two lines of exceptional points cross at a single point. If we keep increasing the negative stiffness, the central domain of stability keeps shrinking, eventually reaching the four-lobed shape of Fig.5.2(f) at $\zeta = \sqrt{2}$. We can clearly see from these last panels that increase in negative stiffness has the

---

[II] A more detailed exposition of non-hermitian time evolution is presented in another paper [205], which we did not include in this thesis for the sake of thematic unity. In a twist of irony, we realised only after writing the thesis that all zero-modes are associated to an exceptional point in the first-order dynamics. Indeed, the above analysis does not depend on the particular form of $\vec{u}_0$, nor on the introduction of active elements in the system. It only requires $\vec{u}_0$ to be in the kernel of the dynamical matrix. In particular, it means that nonlocal resonances are also subject to exceptional point dynamics in the absence of active elements. This makes them a potential platform to explore the interplay of non-hermiticity and temporal modulation theoretically investigated in [205].

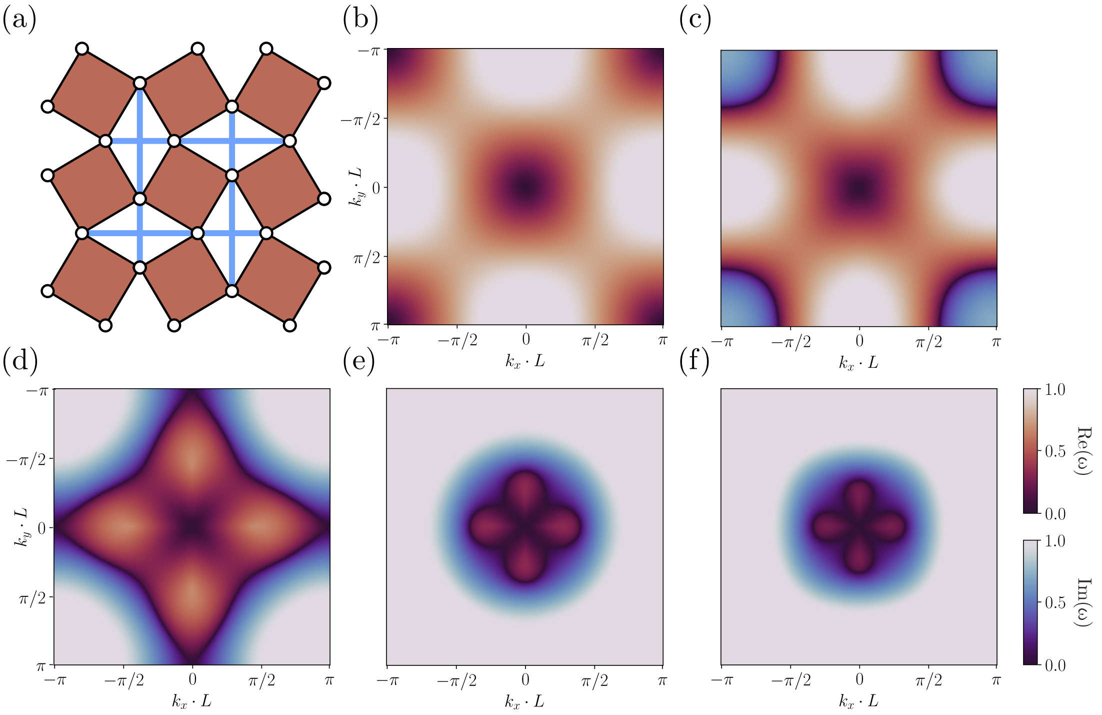

Figure 5.2: Emergence of momentum gaps in the counter-rotating squares metamaterial. (a) Counter-rotating squares mode, with additional negative-stiffness springs depicted as blue lines. (b) Lowest band of the spectrum in the passive case of $\zeta = 0$. (c) Lowest band after the introduction of negative-stiffness springs, with $\zeta = 1/2$. Instability pockets, in which the frequency becomes imaginary, appear in blue. (d) Lowest band at $\zeta = 1$. (e) Lowest band at $\zeta = 4/3$. (f) Lowest band at $\zeta = \sqrt{2}$.

unexpected side effect of increasing the dispersion anisotropy at the Γ point.

To conclude this short detour in the realm of active media, we note that the unstable growth behaviours we discussed above would in practice be stopped at amplitudes where the stabilising nonlinearities become relevant. In the most extreme case, the material fully folds and stays in a new configuration. One could also envision stabilising the metamaterial using the approach of passive PT-symmetric systems, in which the imaginary part of the spectrum is shifted to become purely negative through the introduction of a global damping term. Finally, for realistic geometries, we have seen that anomalous cones are typically gapped. In that context, active elements do not immediately destabilise the system: they start by closing the potentially unwanted mass gaps. This could prove useful in regimes in which improving the hinge design starts hitting diminishing returns.

5.2 Gaps induced at the kinematic graph level

Recall that in Sec.3.4, we introduced an inverse design method that allowed us to shift the reference wavevector of an anomalous cone around by deforming the internal mechanism of the unit-cell. In doing so, we took care to not frustrate this mechanism. Indeed, such frustrations open mass gaps similarly to the additional springs we introduced in Section 5.1, by removing zero modes altogether. We also carefully selected arrow weights that were compatible with Floquet-Bloch boundary conditions. We did so to ensure the emergence of an anomalous cone at the target wavevector, but as a corollary, this choice guaranteed that our local arrow rule would allow for at least one coherent global zero-mode. What happens if we forgo this step, and simply consider a generic local arrow rule ?

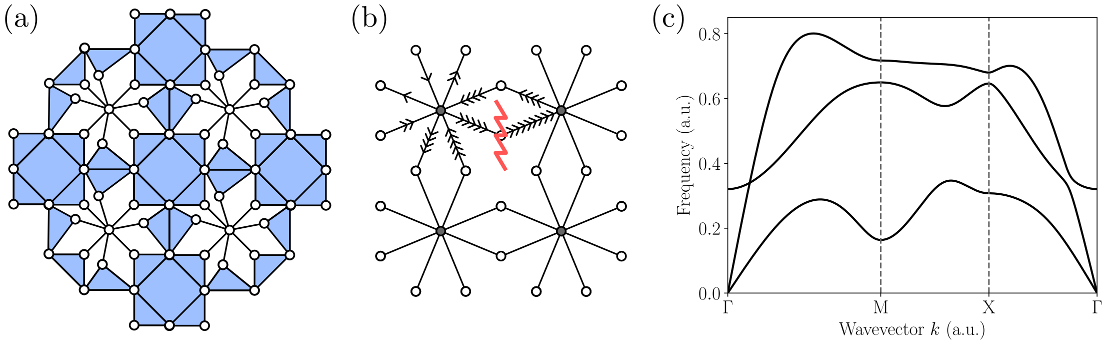

Figure 5.3: Deformed local arrow rule that no longer leads to a global zero-mode. (b) Geometry whose undeformed version hosts a zero-mode with $\vec{k} = \vec{0}$. (b) Attempting to draw the associated kinematic graph immediately leads to a contradiction. (c) A mass-gap arises in the band structure associated to this deformed geometry.

The geometry of Fig.5.3(a) is a deformed version of the one we introduced in Fig.3.8. First, we filled the four-bar linkages between the octagonal units with rigid elements, to simplify the kinematic graph and keep only the zero-mode located at Γ. Then, we rotated six of the central bars in the unit-cell mechanism, in a way that yields the new arrow rule depicted on the top-left cell of Fig.5.3(b). While the original arrow rule, with its equal arrow weights, led to a coherent covering of the kinematic graph, we see in Fig.5.3(b) that the new rule leads to an immediate contradiction. This particular deformation still allows unit cells to individually host nontrivial mechanisms, but our kinematic graph analysis shows that these mechanisms are not compatible with each other and hence that the geometry does not admit any nontrivial zero-mode. This, in turn, leads to the emergence of a mass-gap at the basis of the anomalous cone, as seen in Fig.5.3(c). The effect of our unit-cell deformation appears very similar to the effect of a frustrating spring. The only difference lies in the root cause of the frustration; the height of the gap is now controlled by combinatorial frustration instead of being proportional to the stiffness of a frustrating spring.

This does not mean that local arrow-rules incompatible with Floquet-Bloch boundary conditions inevitably lead to mechanical frustration. To see this, let us use a geometry closely

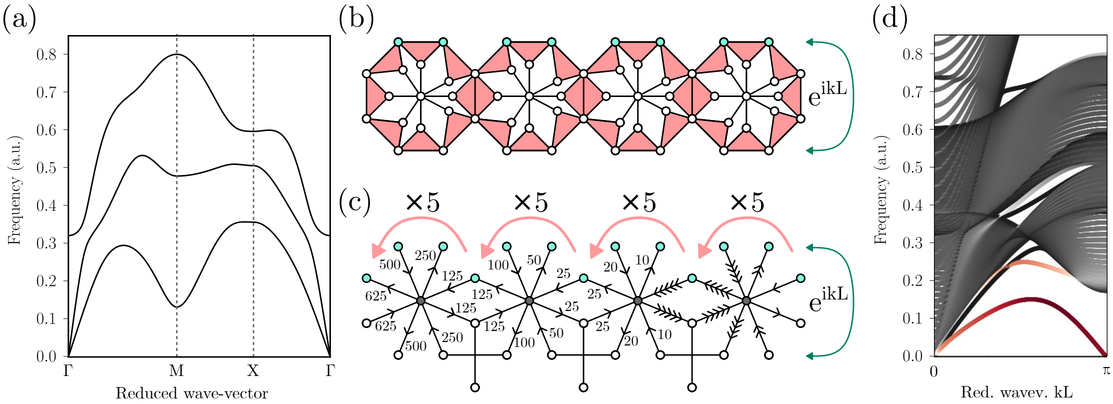

Figure 5.4: Edge states from anomalous cones. (a) Gapped band structure corresponding to the deformed unit-cell of panel (b). (b) Ribbon configuration with Floquet-Bloch boundary condition between the top (indicated in green) and bottom masses. (c) Corresponding graph representation, clarifying the mechanism behind the exponentially decaying spatial profile. (d) Band structure of a ribbon comprising 40 unit cells, with bulk states in grey and states localized to the left edge in red.

related to Fig.5.3(a): we simply free the four-bar linkages again and rotate the octagons by 45°. The local mechanism is preserved by this procedure. In Fig.5.4(a), we see that this again leads to a gapped spectrum; the rotated local arrow rule is still not compatible with Floquet-Bloch boundary conditions. Hence, a mass-gap opens at the basis of the anomalous cone, as in the previous case. This, however, does not imply the total absence of global zero-modes. After all, we still have a local arrow rule at our disposal and should leave it the benefit of the doubt as to whether it can produce a non-contradictory global arrow covering. In fact, such a coherent global arrow configuration can be reached; it is drawn on a four-cell ribbon in Fig.5.4(c). Note that instead of picking up a Bloch phase, the arrow patterns carried by neighbouring cells are multiplied by a real number as we go from right to left. In the top-down direction, we still simply pick up a Bloch phase of -1. The resulting arrow configuration corresponds to a spatial pattern that decays exponentially along one direction and oscillates along the other. Such an edge-localized mode is not directly visible in a band structure with purely real wavevector components. To confirm its presence, we compute the spectrum of a ribbon like the one of Fig.5.4(b), albeit with 40 cells along the horizontal direction instead of four. The top and bottom masses in the ribbon are related with a Floquet-Bloch boundary condition, reflecting our expectation of oscillatory behaviour along that direction.

The resulting spectrum is depicted in Fig.5.4(d), with a colour-coding corresponding to the degree of edge localisation of the modes. The bulk modes, represented as solid black lines, behave as expected from the band structure, with a mass-gap at the edge of the Brillouin zone. Additionally, the edge states predicted from the directed-graph approach leave a ghost imprint (solid red lines) of the former anomalous cone[III].

[III] These edge states can probably be understood within the topological paradigm of Kane and Lubensky, which they applied to the Kagome lattice in [199, 200]. This approach ties nicely with Ch.2 by interpreting the Maxwell-

5.3 Higher-frequency gaps and hybridisation

In this last section, we consider gaps that open directly above the first band. A necessary condition for such gaps to arise is the hybridisation of the lowest dispersion branches. Anomalous cones provide more hybridisation opportunities: for instance, we saw in Fig.3.5(b) that the cone associated to transverse waves connected with the anomalous cones at the corners of the first Brillouin zone, thereby opening a partial band-gap in which only longitudinal elastic waves are allowed. Similarly, the anomalous cones at Γ and M in Fig.3.8(c) respectively hybridised with the longitudinal and transverse cones, thereby opening a complete band-gap. On this basis, one could be tempted to conjecture a connection between anomalous cones at the edge of the Brillouin zone and transverse waves, also motivated by the lower frequencies associated to the latter, which might make such an hybridisation more likely.

However, the 1D chain model of Fig.5.1 immediately dispels such conjectures by providing a counter-example in which an anomalous cone sitting in the corner of the Brillouin zone hybridises with longitudinal waves. This can be explained by using the symmetry decomposition of Eq.(3.5); since longitudinal and anomalous waves are both invariant under reflections across the chain axis, they both belong to the symmetric sector. They are therefore both decoupled from transverse waves, which belong to the antisymmetric sector.

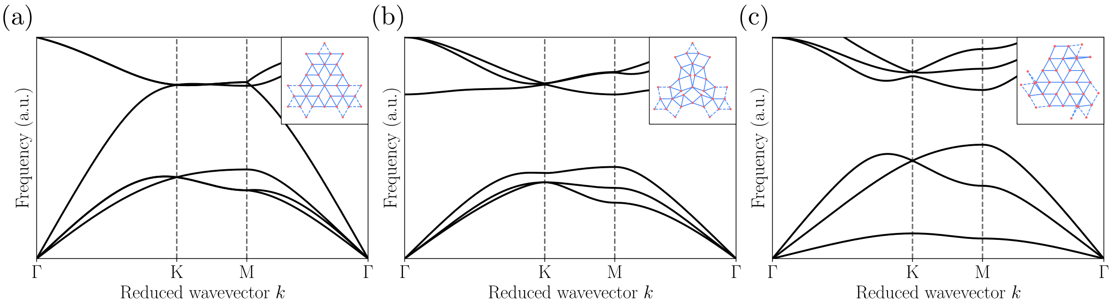

Figure 5.5: Spectra of pre-twisted isograph geometries, with the unit-cells shown in insets. (a) Folded spectrum of an untwisted unit-cell, for reference. (b) Band-gap opened by achiral pre-twisting. (c) Band-gap and slow anomalous sound associated to chiral pre-twisting.

Could we learn something about hybridisation by looking at the kinematic graphs instead ? After all, they encode the spatial profiles of our zero-modes; this could conceivably determine their hybridisation behaviour. To test this hypothesis, we use a family of nonlocally-resonant metamaterials that share the same kinematic graphs -we call such geometries *isograph* geometries- and compare their band structures. To find such an isograph family, we leverage the fact that the mode depicted in Fig.3.4 is a fully nonlinear mechanism. This means that we can push the mechanism beyond the small-angles approximation that underlies kinematic graph theory. To see this, we first note that every elementary linkage in the mechanical network has four hinges of equal size. This implies that in every possible deformation state, these elementary linkages are symmetrical under reflections across their diagonals. In particu-

---

Calladine count from Eq.(2.2) as an index theorem.

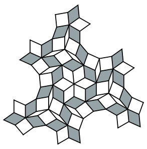

lar, the triangles used in the area law (Eq.(2.5)) must all have the same area. As a consequence, the arrow rule remains valid after we actuate the zero-modes, and we can keep going to larger angular deformations.

A complementary point of view is to explicitely parametrise the allowed configurations of the metamaterial with two angles, without linearising the underlying trigonometric equations. Any member of this two-parameter family of nonlocally-resonant metamaterials then shares the same kinematic graph description by the area law argument presented earlier. In Fig.5.5, we take three different configurations within that family and compute the associated band structures. Because these new configurations are less symmetrical than the original one, a larger unit cell is required in order to still be able to tile the plane periodically. To provide a reference point, we start by re-computing the band structure of the original configuration with this larger unit cell, which yields the spectrum shown in Fig.5.5(a). We note that the two anomalous cones, previously located at the K and K' points, now join the two standard cones at the Γ point. This band folding is simply a change in our mathematical description, since the underlying physical system remains strictly identical[IV].

Having cleared this point, we can now consider twisted geometries. Since their kinematic graphs are identical, our theory predicts that their zero-frequency content should be unchanged. As for the shape of the bands, all bets are off. For the non-chiral configuration of Fig.5.5(b), we observe a surprising result: one cone lifts off and we are left with three cones and a full band-gap. Considering a chiral pre-twisted configuration instead, we obtain the spectrum of Fig.5.5(c), which also exhibits a full band-gap. Another striking feature is the very low speed of sound associated to anomalous waves (the lowest of the three cones). In the unit cell shown in the inset of Fig.5.5(c), three almost entirely folded four-bar mechanisms stand out. If they become entirely folded, the anomalous cone flattens all the way to zero. The resulting flat band means that a zero-mode can be assigned to any wave-vector; we fell back in an extreme locally-resonant situation.

The large differences between these three isograph metamaterials indicates that the kinematic graph is also not enough to determine how the lowest band hybridise. The simplicity of kinematic graph theory is a double-edged sword; while it provides a powerful design tool for nonlocally-resonant metamaterial design, its minimal character also means that it really only fixes the zero-frequency content of the spectrum. Additional dynamical ingredients are then required to sift through the resulting isograph families of nonlocally-resonant metamaterials:

[IV] This raises some apparent paradoxes. For instance, negative group velocity is absent in the folded spectrum. To resolve this tension, note that when a gaussian beam impinges on an interface with the nonlocally-resonant metamaterial, the refracted beam must be expressed in a Bloch wave basis instead of a plane-wave basis. In other words, the refracted beam splits in many components which differ by an integer multiple of the reciprocal lattice vector parallel to the interface. In general, this expansion is dominated by the non-shifted beam, whose behaviour is well described by the dispersion relation in the first Brillouin zone. In our present folded case, a shifted term dominates the Bloch-wave expansion, leading to negative refraction without negative group velocity. Much as in the case of Berry curvature, this example shows that the information contained in the spatially-periodic component of Bloch waves can largely impact wave propagation, and that one cannot in general rely solely on band structure considerations.

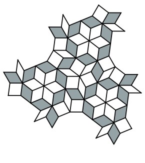

the spatial repartition of mass and stiffness matters.

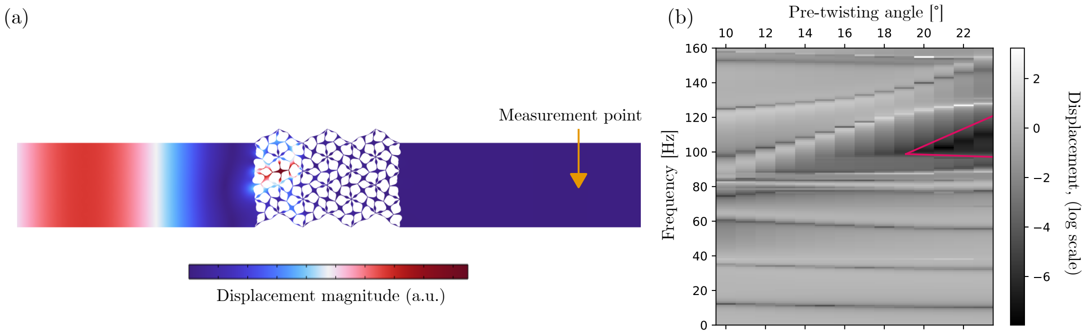

Figure 5.6: Probing the pre-twisting band gaps with an FEM transmission simulation. (a) Simulated geometry, with continuous boundary condition between the bottom and top edges and perfectly-matched layers on left and right edges (not shown). (b) Resulting transmission as a function of pre-twisting angle, with the edges of the theoretical band-gap shown in pink.

In order to gain confidence in the peculiar way in which full band-gaps opened in Fig.5.5(bc), we conclude this section with a series of FEM simulations. The simulation setup is depicted in Fig.5.6(a): we placed a six-cell layer of pre-twisted nonlocally-resonant metamaterial between two isotropic elastic domains, with periodic boundary conditions between the top and bottom edge. Additional perfectly-matched layers (not shown) were placed on the left and right sides to absorb outbound waves. Finally, we imposed a harmonic displacement on the left edge and measured the displacement amplitude at the point indicated by an orange arrow. Sweeping over a range of frequencies and a range of pre-twisting angles resulted in the displacement amplitudes shown in Fig.5.6(b), with a full band-gap opening close to the critical angle predicted by the spring-mass model. This FEM study therefore confirms the predictions of the spring-mass models and also demonstrates that a thin layer of nonlocally-resonant metamaterial is sufficient to provide insulation from vibrations. From an application perspective, isograph families of nonlocally-resonant metamaterials provide an interesting design landscape in which physical properties such as the speed of sound and the width of band-gaps can be finely tuned.

As this chapter comes to an end, let us also recall what we did in the first two sections. We started by adopting a new point of view on nonlocal resonances. Indeed, through the introduction of frustrating springs, we could interpret anomalous cones as intermediaries between mass gaps and momentum gaps. In the process, we noticed an ideal nonlocal resonance behaves as an exceptional point in terms of temporal evolution. Then, we considered the effects of frustrations on the kinematic graph level, uncovering the presence of edge states under certain conditions. This indicates that coherent graphs coverings that do not take on the shape of Bloch waves exist, *i.e.* global zero-modes that do not fit our definition of a nonlocal resonance. In the next chapter, we will study such modes and their spectral signatures.

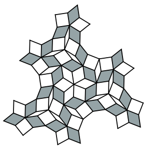

6 Non-Bloch Zero Modes

> *"Using a term like nonlinear science is like referring to*
> *the bulk of zoology as the study of non-elephant animals."*
> — S. Ulam

Some readers might be wondering about a tangle of loose ends left over from Chapters 2, 3 and 4, which we now seek to tidy up. Indeed, as we developed our theory of nonlocal resonances, we encountered various examples of oligomodal geometries whose zero modes do not qualify as nonlocally-resonant. Instead, in these structures, the additional zero-modes exhibited power-law spatial profiles. This class of oligomodal metamaterials does not host anomalous cones; this naturally leads us to wonder where these peculiar non-Bloch modes hide within the spectrum.

6.1 The quadratic spectral signature of the elusive rotational zero-mode.

In our discussion of elastic zero modes in Ch.2, we noted that three global zero modes were always present in two-dimensional structures. In Ch.3, we then interpreted two of these modes, namely the rigid translations, as Goldstone modes of the broken translation symmetry. The global rotation, on the other hand, is still missing from our wave picture; it cannot be interpreted as a Bloch mode. We also encountered other non-Bloch modes in Ch.2 and Ch.4, for instance the two-domain deformation profile of Fig.4.2. In this section, we will incorporate these mysterious modes in the wave picture and identify their spectral signatures.

Consider the two branches emerging from the Γ point in Fig.3.1. They are very reminiscent of Lamb waves in a plate[I], with a symmetric linear branch and an asymmetric quadratic branch. We compute the eigenmodes of the latter using Eq.(3.5), yielding the following displacement

---

[I] The analogy can be explained by interpreting elastic chains of nonzero height as discretised cross-sections of finite-width plates.

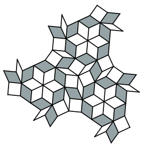

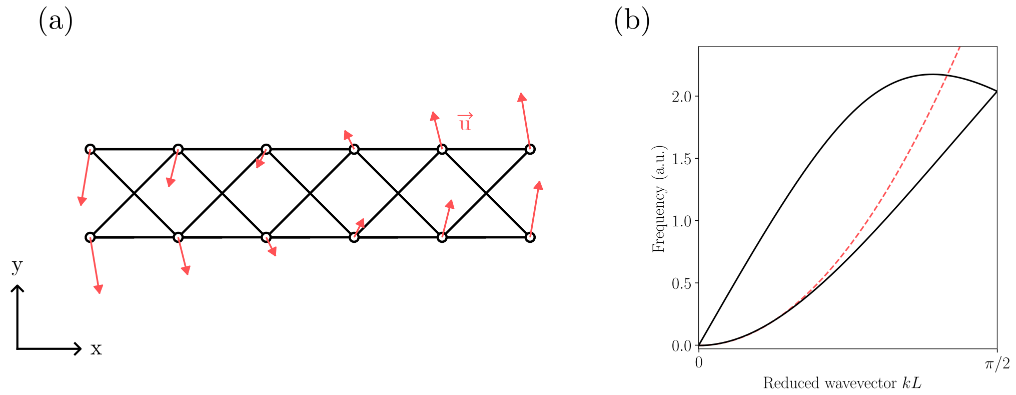

Figure 6.1: Quadratic spectral signature of a non-Bloch zero-mode in an elastic chain. (a) Rigid rotation zero-mode, with the displacement shown in red. (b) Corresponding spectrum, with a dashed red line depicting a reference parabola.

at the nth site,

$$\begin{aligned}\vec{\psi}_{A-}(n,\phi) = e^{in\phi}\vec{u}_{A-}(\phi) &= e^{in\phi}\left(\frac{1+\cos(\phi)}{2i}\left|\begin{matrix}\uparrow\\ \uparrow\end{matrix}\right\rangle - \frac{\sin(\phi)}{2}\left|\begin{matrix}\leftarrow\\ \rightarrow\end{matrix}\right\rangle\right)\\ &\approx (1+in\phi)\left(-i\left|\begin{matrix}\uparrow\\ \uparrow\end{matrix}\right\rangle - \frac{\phi}{2}\left|\begin{matrix}\leftarrow\\ \rightarrow\end{matrix}\right\rangle\right) \approx -i\left|\begin{matrix}\uparrow\\ \uparrow\end{matrix}\right\rangle + n\phi\left|\begin{matrix}\uparrow\\ \uparrow\end{matrix}\right\rangle - \frac{\phi}{2}\left|\begin{matrix}\leftarrow\\ \rightarrow\end{matrix}\right\rangle,\end{aligned} \quad (6.1)$$

where we assumed $n\phi \leq N\phi << 1$, requiring the chain to have a finite number of sites N. The mode's frequency is equal to $\omega_{A-}(\phi) \approx \phi^2/2$; as a consequence, the mode superposition

$$\vec{\psi}_{A0}(n,\phi) - \vec{\psi}_{A-}(n,0) \approx n\phi\left|\begin{matrix}\uparrow\\ \uparrow\end{matrix}\right\rangle - \frac{\phi}{2}\left|\begin{matrix}\leftarrow\\ \rightarrow\end{matrix}\right\rangle \quad (6.2)$$

is a zero-energy state of the chain, to first order in ϕ. As for the elusive rotational rigid mode of the chain, it can be expressed as

$$\begin{aligned}\vec{\psi}^{\pm}_{R}(n,\phi) = R(\phi)\vec{r}^{\,\pm}_{n} - \vec{r}^{\,\pm}_{n} &= \begin{pmatrix}\cos(\phi) & -\sin(\phi)\\ \sin(\phi) & \cos(\phi)\end{pmatrix}\begin{pmatrix}n\\ \pm\frac{1}{2}\end{pmatrix} - \begin{pmatrix}n\\ \pm\frac{1}{2}\end{pmatrix}\\ &\approx \begin{pmatrix} & -\phi\\ \phi & \end{pmatrix}\begin{pmatrix}n\\ \pm\frac{1}{2}\end{pmatrix} = \phi\begin{pmatrix}\mp\frac{1}{2}\\ n\end{pmatrix},\end{aligned} \quad (6.3)$$

where the ± superscript denotes the top and bottom masses. In the symmetrised basis, this yields

$$\vec{\psi}_R(n,\phi) \approx \phi\left|\begin{matrix}\circlearrowleft\\ n\end{matrix}\right\rangle := n\phi\left|\begin{matrix}\uparrow\\ \uparrow\end{matrix}\right\rangle - \frac{\phi}{2}\left|\begin{matrix}\leftarrow\\ \rightarrow\end{matrix}\right\rangle \approx \vec{\psi}_{A-}(n,\phi) - \vec{\psi}_{A-}(n,0) \tag{6.4}$$

The reason for which the rotational zero-mode seemed absent of the spectrum is because it is non-Bloch in nature: we need a superposition of two modes infinitesimally close to $\phi = 0$ to express it. The zero-energy character of this mode then puts a constraint on the spectrum, inducing the quadratic dispersion associated to the asymmetric waves. This argument might be generalisable to Lamb waves. In this context, we surmise that the existence of zero-frequency rigid rotations around axes lying in the plane of the plate implies that asymmetric Lamb waves must have a slowly-growing spectrum in the vicinity of $\vec{k} = 0$.

6.2 Power-law mode profiles in oligomodal geometries.

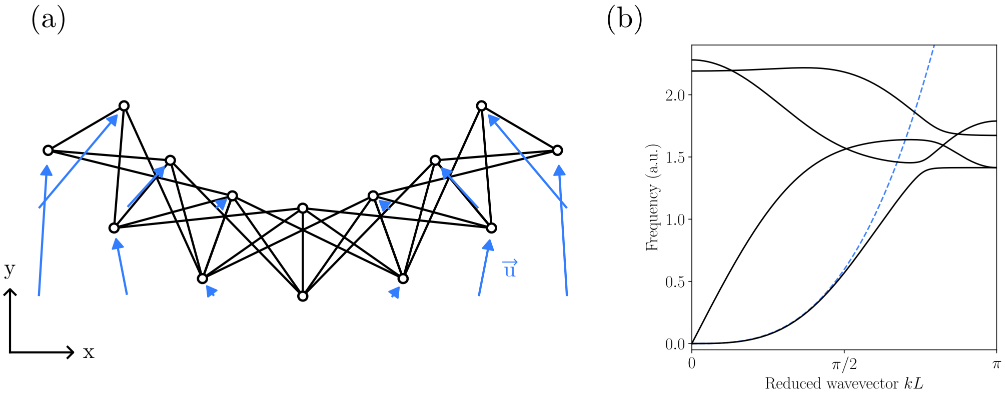

Figure 6.2: Cubic spectral signature of a non-Bloch zero-mode in an elastic chain. (a) Non-trivial zero-mode in a unimodal elastic chain, with the displacement shown in blue. (b) Corresponding spectrum, with a reference cubic curve drawn as a dashed blue line.

This line of argument generalises to elastic chains with additional non-Bloch zero-modes besides the rotational one. As an example, we consider the chain depicted in Fig.6.2(a). It is based on the same inverted four-bar mechanism as the chain of Fig.6.1(a), simply rotated by $\pi/2$. In order to limit the number of available zero-modes to one and therfore make the chain oligomodal, a stretched copy of the mechanism is added to connect next-nearest neighbours. The resulting global zero-mode, which is depicted in Fig.6.1, also cannot be written as a Bloch wave. Indeed, the displacement patterns grows monotonously away from the chain center. We note in passing that the displaced masses lie on two concentric circles. In the following discussion, we will call this the "flexion mode".

In order to uncover the spectral signature of this zero-mode, we leverage the simplicity of the chain to investigate its dynamical matrix analytically. In the M_x-antisymmetrised sector, the dynamical matrix of this chain has the form

$$\mathscr{D}_A = \begin{pmatrix} 5\cos(\phi) + 8\cos(2\phi) + 13 & i\sin(\phi)(8\cos(\phi) + 5) \\ -i\sin(\phi)(8\cos(\phi) + 5) & 2\sin\left(\frac{\phi}{2}\right)^2 (4\cos(\phi) + 9) \end{pmatrix}. \tag{6.5}$$

Diagonalising $\mathscr{D}_A$ yields the following dispersion for the transverse branch,

$$\begin{aligned} \omega_{A-}(\phi) &= \sqrt{3\cos(2\phi) + 10 - \sqrt{75\cos(\phi) + 30\cos(2\phi) + 5\cos(3\phi) + \frac{9}{2}\cos(4\phi) + \frac{109}{2}}} \\ &\approx \sqrt{\frac{5}{52}\phi^3 + \mathscr{O}(\phi^4)}, \end{aligned} \tag{6.6}$$

which shows that the band is indeed cubic near $\phi = 0$, as we could have guessed from the full band structure shown in Fig6.2(b). The eigenmode associated to this cubic branch is given by

$$\begin{aligned} \vec{u}_{A-}(\phi) &= \frac{\sin(\phi)(8\cos(\phi) + 5)}{13\phi} \left|\begin{matrix}\uparrow\\\uparrow\end{matrix}\right\rangle \\ &+ \frac{i(\sqrt{75\cos(\phi) + 30\cos(2\phi) + 5\cos(3\phi) + \frac{9}{2}\cos(4\phi) + \frac{109}{2}} - 3 - 5(\cos(\phi) + \cos(2\phi)))}{13\phi} \left|\begin{matrix}\leftarrow\\\rightarrow\end{matrix}\right\rangle \\ &\approx [1 - \frac{37}{78}\phi^2] \left|\begin{matrix}\uparrow\\\uparrow\end{matrix}\right\rangle + \frac{i\phi}{2} \left|\begin{matrix}\leftarrow\\\rightarrow\end{matrix}\right\rangle + \mathscr{O}(\phi^3). \end{aligned} \tag{6.7}$$

Expanding the mode profile in vicinity of $\phi = 0$ yields

$$\begin{aligned} e^{in\phi}\vec{u}_{A-} &= e^{in\phi}[f(\phi)\left|\begin{matrix}\leftarrow\\\rightarrow\end{matrix}\right\rangle + g(\phi)\left|\begin{matrix}\uparrow\\\uparrow\end{matrix}\right\rangle] \\ &= (\sum_{m=0}^{\infty} \frac{(in\phi)^m}{m!})[\sum_{m=0}^{\infty} \alpha_m \phi^{2m+1}\left|\begin{matrix}\leftarrow\\\rightarrow\end{matrix}\right\rangle + \sum_{m=0}^{\infty} \beta_m \phi^{2m}\left|\begin{matrix}\uparrow\\\uparrow\end{matrix}\right\rangle] \\ &= [\alpha_0\phi + in\alpha_0\phi^2]\left|\begin{matrix}\leftarrow\\\rightarrow\end{matrix}\right\rangle + [\beta_0 + in\beta_0\phi + (\beta_1 - \frac{n^2}{2}\beta_0)\phi^2]\left|\begin{matrix}\uparrow\\\uparrow\end{matrix}\right\rangle + \mathscr{O}(\phi^3) \\ &= (1 + \frac{37}{78}\phi^2)\left|\begin{matrix}\uparrow\\\uparrow\end{matrix}\right\rangle + i\phi\left|\begin{matrix}\circlearrowleft\\ n\end{matrix}\right\rangle - \phi^2\left[\frac{n}{2}\left|\begin{matrix}\leftarrow\\\rightarrow\end{matrix}\right\rangle + \frac{n^2}{2}\left|\begin{matrix}\uparrow\\\uparrow\end{matrix}\right\rangle\right] + \mathscr{O}(\phi^3). \end{aligned} \tag{6.8}$$

Since the frequency now scales like $\omega \sim \phi^3$, we can access terms of order ϕ^2 for a negligible energetic cost. As we can see in the last line Eq.(6.8), there are now three accessible modes, namely the transverse mode $\left|\begin{matrix}\uparrow\\ \uparrow\end{matrix}\right\rangle$, the rotation mode $\left|\begin{matrix}\circlearrowleft\\ n\end{matrix}\right\rangle$ and a mystery mode highlighted in blue, which encouragingly contains a term quadratic in the site index n. This clearly evokes the shape of the nontrivial flexion mode. Does the strategy that we applied to the rigid rotation zero-mode also work in this case ? To make sure, we need to compare the third term of Eq.(6.8) to the exact nonlinear formulation of the flexion mode. The displacements corresponding to this flexion mode are given[II] by

$$\vec{u}_n^+ = \begin{pmatrix}\mathrm{Re}[(z(\theta) - i)\sum_{m=0}^{n-1} e^{im\theta}) - n] \\ \mathrm{Im}[(z(\theta) - i)\sum_{m=0}^{n-1} e^{im\theta}) - n]\end{pmatrix} \qquad \vec{u}_n^- = \begin{pmatrix}\mathrm{Re}[(z(\theta) - ie^{i\theta})\sum_{m=0}^{n-1} e^{im\theta}) - n] \\ \mathrm{Im}[(z(\theta) - ie^{i\theta})\sum_{m=0}^{n-1} e^{im\theta}) - n]\end{pmatrix}. \tag{6.9}$$

where $z(\theta) = i/2(1 + e^{i\theta}) + 1/2\sqrt{6e^{i\theta} - e^{2i\theta} - 1}$. Expanding these expressions with the angle θ as a small parameter, and symmetrising the displacement basis with respect to M_x, we get

$$\vec{u}_n \approx \theta \left[\frac{n}{2} \left|\begin{matrix}\leftarrow\\ \rightarrow\end{matrix}\right\rangle + \frac{n^2}{2} \left|\begin{matrix}\uparrow\\ \uparrow\end{matrix}\right\rangle \right] + \mathcal{O}(\theta^2). \tag{6.10}$$

Upon the identification $\theta = -\phi^2$, we retrieve precisely the third term in the expansion of Eq.(6.8), thereby confirming the connection between a quadratic spatial profile and a cubic dispersion. More generally, spatial dependencies of the order n^m can only arise at the order ϕ^m and beyond. Therefore, the existence of a non-Bloch zero-mode with a power-law spatial profile seems to imply the existence of a dispersion branch with a higher power law dependency, in order to be able to express this zero-mode as a linear combination of Bloch waves with negligible energy in the immediate vicinity of $\phi = 0$.

This connection also holds in a two-dimensional setting. Recall the modes discussed in Sec.4.1; they had a distinct non-Bloch profile. As a reminder, see Fig.6.3(a), in which we can observe a stark gradient in the deformation magnitude along direction (i). In the limit of small deformations, this gradient consists in a linear profile. Because the associated kinematic graphs, described in Fig.2.9, are not compatible with Floquet-Bloch boundary conditions, we do not expect these modes to induce anomalous cones. Instead, computing the spectrum of the associated spring-mass model reveals the same quadratic signature, shown in Fig.6.3(b). Note that the wave-vectors in Fig.6.3(b) point in direction (i). As for the neutral direction (ii), it is associated to a linear dispersion, as shown in Fig.6.3(c). This dispersion anisotropy is clearly visible in the isofrequency contours of Fig.6.3(d). This clearly indicates that the quadratic spectral signature is again associated to a linear mode profile. The connection between power-

---

[II] It is convenient to treat such problems by writing vectors in the plane as complex numbers.

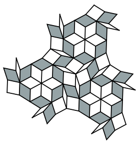

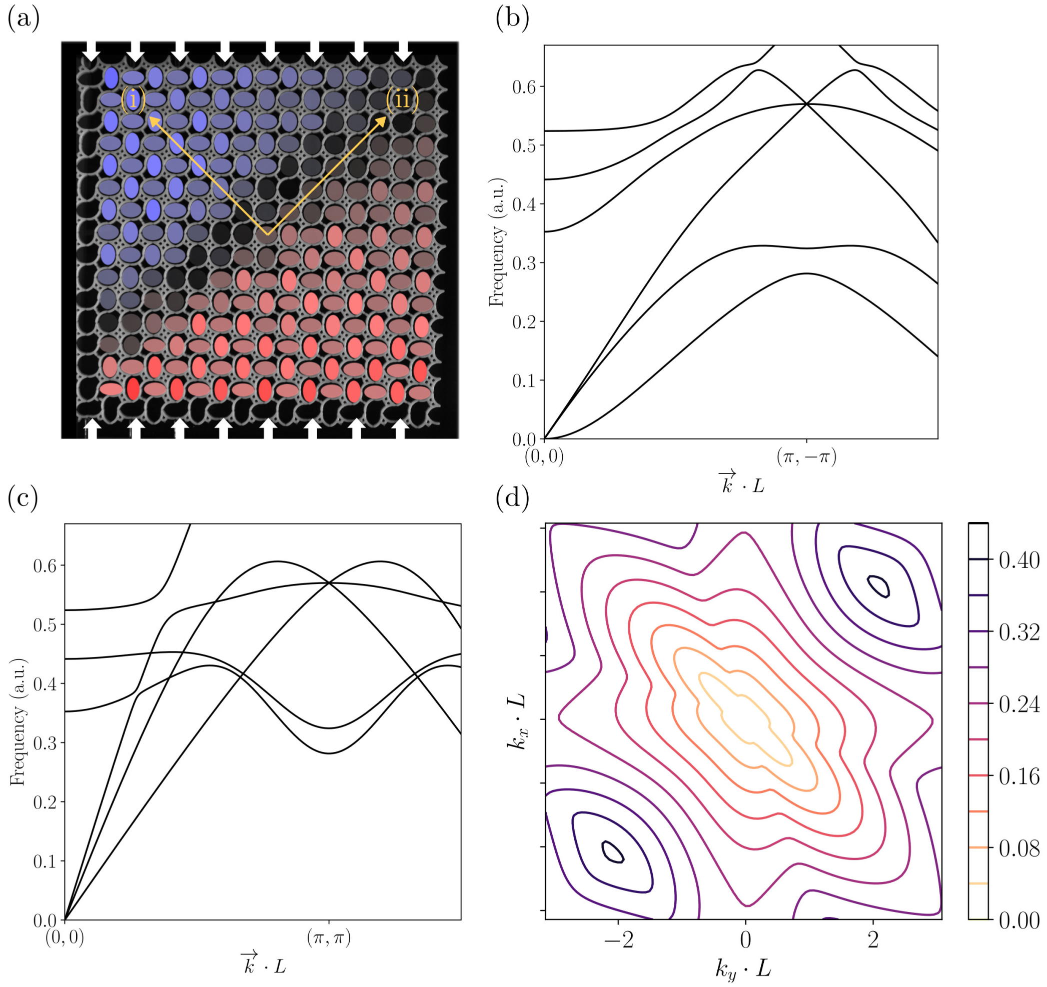

Figure 6.3: Quadratic spectral signature of a non-Bloch 2D zero-mode with linearly growing profile. (a) Experimental mode profile from Fig.4.2(b), with two directions of interest indicated with yellow arrows. (b) Corresponding band structure along direction (i), that is along the linear growth direction. (c) Band structure along direction (ii), with a mostly periodic variation. (d) Isofrequency contours of the first band in the vicinity of Γ.

law mode profiles and power-law spectral signatures is therefore clearly present in higher dimensions as well.

6.3 Concluding remarks.

In this chapter, we solved two mysteries. The first consisted in the incomplete correspondence between standard elastic waves and global rigid modes, in which the rotation mode was not assigned to a wave. It turns out that this rigid rotation mode, which corresponds to a linear displacement profile in the small-angle limit, manifests itself in the spectrum through as a quadratic dispersion. Encouraged by this success, we then applied the same method to two cases of global, but non-Bloch, zero-modes. Continued success in these cases seems to indicate a general connection between non-Bloch, power-law spatial profiles and power-law dispersions. The slow growth of frequency associated to such dispersions in the vicinity of $k = 0$ allowed us to express the mysterious non-Bloch zero-modes as linear superpositions of modes close enough to $k = 0$ to have effectively vanishing frequency.

Of course, the analytical arguments we used to uncover this relationship were a bit cavalier. For one thing, we reasoned in terms of Bloch waves while implicitly using a N-site chain with open boundary conditions. Additional care might be required to make this line of thought fully rigorous, but we expect the underlying ideas to be correct. We note in passing that we also considered another type of non-Bloch modes, for which the Bloch description fails because the geometry that supports them lacks periodic order. For completeness, we briefly discuss this quasicrystalline case in Appendix C.

The conceptual tools we developed to solve these problems will prove useful in the next chapter, by allowing us to correctly assign wave types to various dispersion branches in complex three-dimensional metamaterials. In the process, we will also develop other helpful tools to treat these intricate situations, by formalising symmetry considerations.

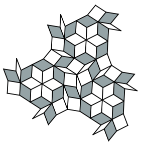

7 The Role of Symmetry

> *"Tyger Tyger, burning bright,*
> *In the forests of the night;*
> *What immortal hand or eye,*
> *Dare frame thy fearful symmetry?"*
> — W. Blake

In the preceding chapters, symmetry was often lurking in the shadows; we mostly used it to pick convenient bases for our analytical models and to distinguish various types of waves. In this chapter, we want to address symmetry more directly and make it an integral part of our design process. In order to access the richer realm of three-dimensional symmetries, we will also consider another design path for elastic nonlocal resonances, distinct from the kinematic graph approach.

7.1 Space group redux

As usual, we start this chapter in company of our old friend, the 1D elastic chain. In this section, we will use this minimal model to refresh a few notions in the representation theory of space groups, before applying this theory to higher-dimensional cases in the remainder of the chapter. Besides the concrete application of these concepts to our toy model, none of the results presented in this section are new; rigorous in-depth expositions of group theory can be found in Ref. [220].

When we say that a geometric object has a certain symmetry, what we mean is that there exists an isometry[I] that leaves it invariant. In crystals, these isometries consist of translations along Bravais-lattice vectors, as well as a series of rotations, reflections and glide symmetries. These isometries form a group: indeed, the identity is always an isometry, and the inverse of a given isometry is also an isometry. Furthermore, successive applications of isometries

---

[I] A transformation that preserves distances.

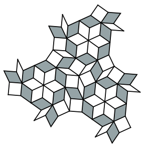

on the symmetric object leave it invariant, and this isometry composition is associative. The resulting group of symmetries is called the *space group* of the crystal; we will denote it as S.

To leverage this algebraic structure, we first need some elements of finite group theory. The action of an element g of a group G on some vector space V, for instance the space of displacements $\vec{u}$ of a collection of point masses, can be represented with a matrix $\boldsymbol{\rho}(g)$. We say that these matrices form a *representation* of the group if and only if they preserve the group structure, in the sense that $\boldsymbol{\rho}(g)\boldsymbol{\rho}(h) = \boldsymbol{\rho}(gh)$. Note that the map $\boldsymbol{\rho} : G \to GL(V)$ is only an homomorphism, meaning that two distinct group elements can be mapped to the same matrix $\boldsymbol{\rho}$. An extreme example is the trivial representation, admitted by any group, which is simply defined as $\boldsymbol{\rho}(g) = 1$ for every group element.

Any representation can be decomposed into elementary blocks called irreducible representations (*irreps*) in the following sense: one can find a basis P_{irr} in which all matrices $\boldsymbol{\rho}(g)$ become block-diagonal simultaneously,

$$P_{irr}\boldsymbol{\rho}(g)P_{irr}^{-1} = \begin{pmatrix} \boldsymbol{\rho}_1(g) & & & & \\ & \boldsymbol{\rho}_2(g) & & & \\ & & \boldsymbol{\rho}_2(g) & & \\ & & & \boldsymbol{\rho}_3(g) & \\ & & & & \ddots \end{pmatrix}, \tag{7.1}$$

where the subscripts denote different irreps. The decomposition is essentially unique, and no blocks smaller than the irrep ones can be found. Note that in this decomposition, each irrep can show up more than once, or not at all; here, the second irrep $\boldsymbol{\rho}_2(g)$ appears twice.

This group machinery becomes extremely useful as we start considering dynamical aspects. Indeed, all symmetry operations must commute with the dynamical matrix: $[\mathscr{D}, \boldsymbol{\rho}(g)] = 0$. As a corollary of Schur's lemma, only multiples of the identity can commute with every matrix of an irrep. This means in particular that $\mathscr{D}$ must take on the form

$$\mathscr{D}_{irr} = \begin{pmatrix} \omega_1^2 \mathbb{1}_{n1} & & & & \\ & \alpha_2 \mathbb{1}_{n2} & \beta_2 \mathbb{1}_{n2} & & \\ & \gamma_2 \mathbb{1}_{n2} & \delta_2 \mathbb{1}_{n2} & & \\ & & & \omega_3^2 \mathbb{1}_{n3} & \\ & & & & \ddots \end{pmatrix} \tag{7.2}$$

in the irrep basis to satisfy the commutation relation [II]. Note that the blocks associated to an

---

[II] In this expression, $\mathbb{1}_{ni}$ denotes an $n_i \times n_i$ identity matrix, and the greek letters are complex numbers.

irrep that appears only once in the decomposition must be multiples of the identity, while irreps that appear with a certain multiplicity d leave a little bit more freedom to the form of the dynamical matrix.

This has two major physical consequences. First, it implies that every eigenmode can be assigned to an irrep. In particular, this allows us to infer how this mode transforms when we apply an isometry g: we just have to let the associated $\boldsymbol{\rho}_{irr}(g)$ act on the mode. If the irrep is one-dimensional, as in the 1D chain example we will consider shortly, this symmetry operation simply amounts to multiplying the mode by a scalar.

The second consequence relates to the case in which the irrep has a dimension $n_{irr} > 1$. In this case, we can infer from the shape of $\mathscr{D}$ in Eq.(7.2) that n_{irr} modes share the same eigenvalue, yielding a spectral degeneracy. Because of the irreducibility of the representation associated to this sector, perturbations must break the symmetry to lift this degeneracy; it is symmetry-protected. We will explore this case using more complex geometries in Sec.7.3.

These considerations look promising, but how can we apply them to infinitely-extended crystals and their equally infinite space groups? One potential starting point is to note that these infinities are rooted in the presence of translations. This suggests the following strategy: we begin by somehow separating the translation content of S from the other symmetries. We then treat the infinity problem in this restricted setting and construct irreducible representations of S from there.

The first step of our strategy is most easily achieved with so-called symmorphic[III] space groups, which can be expressed as a semi-direct product $S = P \ltimes T$ involving the point group P and the translation group T. For concreteness, consider the case of our minimal spring-mass chain: it has the largest group of symmetries that a chain in the plane can have[IV], namely $S = p2mm$ [V]. As discussed in Ch.3, this group is generated by translations along the chain axis, a reflection across the chain axis and a reflection perpendicular to the chain axis; in the semi-direct product, we have $P = \{\mathbb{1}, M_x, M_y, R_\pi\} = D_2 \sim \mathbb{Z}_2 \times \mathbb{Z}_2$.

Having isolated T as a normal subgroup of S, we need a trick to make our finite group considerations applicable. Instead of considering an infinite crystal, we consider a N-sites chain with periodic boundary conditions, with the idea of later letting N tend to infinity. In this setting, T is isomorphic to the cyclic group C_N; it consists of N translations. The abelian group C_N admits N one-dimensional irreps. We can write the mth such irrep as $\boldsymbol{\rho}_m(t_n) = e^{i\phi_m n} = e^{ik_m L n}$, where the intercell phase can now only take on the discretised values $\phi_m = m\frac{2\pi}{N}$ with $m \in \{1, \ldots, N\}$.

This is actually the content of Bloch's theorem ! Since $[\mathscr{D}, t_n] = 0$, we can apply Schur's lemma and go over to the irrep basis. There, the large dynamical matrix of the N-site chain splits in N

[III] Non-symmorphic space groups, which we will not use in this thesis, contain some symmetry elements that combine a point operation with a translation **without** also containing both of the latter. A prototypical example is the glide symmetry of footprints in the sand.

[IV] In this context, S is called a frieze group.

[V] Under the International Union of Crystallography convention.

Table 7.1: Character table of the D_2 point group. Each column corresponds to an irreducible representation, and each row to a conjugacy class. Each irrep is labeled by two states that transform under it.

	$\vec{u}_S^+$ $\vec{u}_Z$	$\vec{u}_S^-$ $\vec{u}_T$	$\vec{u}_A^+$ $\vec{u}_L$	$\vec{u}_A^-$ $\vec{u}_S$
$\mathbb{1}$	1	1	1	1
M_y	1	1	-1	-1
M_x	1	-1	1	-1
R_π	1	-1	-1	1

blocks, each associated to a particular irrep of the translation group T[VI]. As promised, we also learn something about the shape of the modes, namely that a mode in the mth sector must pick up a phase of $e^{i\phi_m n}$ under the translation t_n. In other words, the modes must take on the shape of Bloch waves, with Bloch wavenumbers k_m.

The power of the space group approach starts to become apparent; it implies Bloch's theorem as a special case. To unleash its full potential, we need to construct irreps for the whole of S, instead of its normal subgroup T. To do so, we introduce a so-called "little group" $L(e^{i\phi_m})$ associated to each translation irrep. $L(e^{i\phi_m})$ is a subgroup of S that leaves ϕ_m fixed. In the symmorphic case, it can be expressed as $L(e^{i\phi_m}) = P_{\phi_m} \ltimes T$, where P_{ϕ_m} consists of the point-group operations that leave ϕ_m unchanged. Concretely, in our 1D chain example, we have to consider three cases. First, we tackle the case of a generic ϕ_m; exactly two point operations leave it unchanged, yielding $P_{\phi_m} = \{\mathbb{1}, M_x\}$. The remaining point operations also leave the two special values $\phi_m = 0, \pi$ invariant, yielding $P_0 = P_\pi = P$. With this, we constructed a little group for every wavenumber.

The symmorphic character of S then again comes to our aid to construct irreps of $L(e^{i\phi_m})$: they are simply given by $\boldsymbol{\rho}_L(g) = \boldsymbol{\rho}_L(p; t_n) = \boldsymbol{\rho}_{P_\phi}(p) e^{i\phi_m n}$. With this, we reduced the problem to finding the irreps $\boldsymbol{\rho}_P$ of the point group. This is a standard exercise of finite group theory. Concretely, in our p_2mm example, we need to find the irreps of the dihedral group D_2. First, we note that its four elements $\{\mathbb{1}, M_x, M_y, R_\pi\}$ each belong to a distinct conjugacy class. Consequently, there are four irreps in total. Since $\sum_{i=1}^4 n_i^2 = |D_2| = 4$ must hold, we can deduce that these irreps are all one-dimensional. In particular, this means that the irrep matrices are simply equal to their characters. We then only need to construct the character table of D_2, which is easily achieved using the orthogonality relations between the characters of different irreps and some general properties of character tables. The result is shown in Table 7.1.

Finally, we are in a position to construct the irreps of the space group from those of the little groups. For generic wavenumbers ϕ_m/L, the construction of an irrep requires the introduction

---

[VI] Note that each translation irrep enters the decomposition with a multiplicity corresponding to the number of DOFs in the unit cell. Consequently, the corresponding block of the dynamical matrix is not constrained to be a multiple of identity; this is the group-theoretical justification of the reduced, wavevector-dependent shape of the dynamical matrices we heavily used in previous chapters.

of the concept of a star of wavevectors, namely a set of wavevectors related by point group operations. In our 1D chain case, the star consists of $\{-\phi_m, \phi_m\}$, which are exchanged by the operations $\{M_y, R_\pi\}$. Concretely, we can build the irreps using the combinations $\vec{u}^{\pm}_{A,S}(\phi) = \vec{u}_{A,S}(\phi) \pm \vec{u}_{A,S}(-\phi)$, where the subscript A, S indicates whether the state is antisymmetric under the action of M_x. This accounts for the effect of the nontrivial P_{ϕ_m} restricted point group, which we already leveraged in Eq.(3.5). As for the ± superscript, it indicates whether we consider a symmetric or antisymmetric combination of modes evaluated on the star of ϕ_m; to see how a given combination transforms under the action of a particular space group isometry, multiply it by the entry of Table 7.1 corresponding to the underlying point operation and then by the translation irrep $e^{i\phi_m n}$.

At the special point $\phi = 0$ and $\phi = \pi$, no need for stars[VII]; to obtain an irrep of p_2mm there, simply pick a column of Table 7.1 and multiply it by the appropriate translation irrep, namely $e^{i0n} = 1$ or $e^{i\pi n} = (-1)^n$. We can use this to learn more about the symmetry of the modes at these special points.

We start with $\phi = \pi$ and go over to the irrep basis; this diagonalises the dynamical matrix, assigning every branch to a particular 1D irrep. In Table 7.1, the irrep names were chosen to reflect this fact. From this table, we learn how each mode at $\phi = \pi$ transforms under isometries: the zero-mode $\vec{u}_Z$ is invariant under every point group operation, the transverse $\vec{u}_T$ picks up a minus sign under M_x and R_π, the longitudinal $\vec{u}_L$ picks up a minus sign under M_y and R_π, and finally the in-plane sheared wave $\vec{u}_S$ picks up a minus sign under M_x and M_y. Naturally, all of these modes also pick up a minus sign if the full isometry involves a translation by an odd number of sites, since $\phi = \pi$.

The same reasoning holds at $\phi = 0$, with two slight twists. First, the four irreps are not assigned to the same bands: the bands that were anomalous and longitudinal at $\phi = \pi$ switch their point-group irreps at $\phi = 0$. As for the two other wave types, they stay on the same branch, but both acquire mixed type in the intervening wavenumbers. Second, the associated eigenvalues are now degenerate. Here, we must distinguish two different situations. As discussed in Ch.3 and Ch.6, the zero-frequency degeneracy involving transverse and longitudinal waves arises from the broken translation symmetry and is unavoidable for freely moving crystals. The higher-frequency degeneracy between the two other wave types, on the other hand, constitutes a so-called *accidental degeneracy*. It has nothing to do with the space group; as we can see in Fig.5.1(b), this degeneracy is actually lifted by the introduction of the frustrating spring, which does not break the spatial symmetries of the chain.

The sieve of group theory allowed us to sift through the spectrum and examine the elementary grains that compose it one by one, illuminating their symmetrical features. Our 1D chain example was unusually nice, in the sense the unit cell was so small that we could bring eigenmodes in one-to-one correspondance with space-group irreps. In general, we can still

---

[VII] For more complex Brillouin zones, points with smaller stars are labeled with capital letters, such as Γ or K, because of these symmetry properties.

assign eigenmodes or stars of eigenmodes to irreps, but a given space-group irrep may appear in the spectrum more than once or not at all; the spectrum splits into sectors labeled by the irreps of S.

This exercise in representation theory, while conceptually satisfying, mostly consisted in describing a model we already understood well using a different language. It also provided group-theoretical underpinnings to the band-structure tools we heavily used in the preceding chapters. In Secs.7.2 and 7.3, we will show that this group-theoretical point of view also constitutes a strong addition to our design toolbox for nonlocally-resonant metamaterials. In particular, the accidental degeneracy observed at the $k = 0$ in our chain model must be contrasted with the symmetry-protected degeneracies we will discuss in Sec.7.3, which arise when higher-dimensional irreps show up in the decomposition. Frieze groups are not large enough to carry such irreps; we need bigger space groups to investigate symmetry-protected degeneracies.

7.2 Weakly coupled elastic IWMs

Three-dimensional geometries would be very helpful to construct interesting spectral degeneracies in nonlocally-resonant metamaterials. Indeed, point groups in lower dimensions are quite restricted in terms of irreps, with 2D irreps only timidly appearing in two spatial dimensions. To obtain a larger variety of irreps and their associated spectral degeneracies, we would therefore like to move on to three spatial dimensions. However, a nontrivial extension of the kinematic graph approach to three dimensions seems far from obvious, mostly because of the non-planar character of hinge motions in this setting. For this reason and also in order to extend our toolbox of nonlocally-resonant mechanisms, we introduce an alternative approach to zero-modes.

It simply consists in taking the interlaced wire media described in Fig.1.6 and treating them elastically instead of electromagnetically. To warm up, we first consider the one-dimensional case of two interlaced twisting rods, with the unit-cell shown in Fig.7.1(a). In order to ensure mechanical stability, we also introduced a small spring connecting the two disconnected giant components (GCs), as seen in Fig.7.1(b). To compute the associated band structure, we set up a FEM eigenfrequency simulation with Floquet-Bloch boundary conditions and sweep over the Bloch wavenumber. The resulting band structure is shown in Fig.7.1[VIII].

To analyse this spectrum, let us first imagine the situation in the absence of the stabilising spring. At $\omega = 0$, we can think of the two GCs as being perfectly rigid bodies. Therefore, each GC carries six zero-modes: three translations and three rotations. Considering a twisting GC in isolation, for instance by ignoring the yellow GC in Fig.7.1(d-f), the zero-modes can be interpreted as follows. The translation along the chain axis, shown in Fig.7.1(d), corresponds to an infinite-wavelength longitudinal wave. As for the two translations perpendicular to

---

[VIII] Note that this structure retains a continous screw symmetry, which should also put strong constraints on the modes.

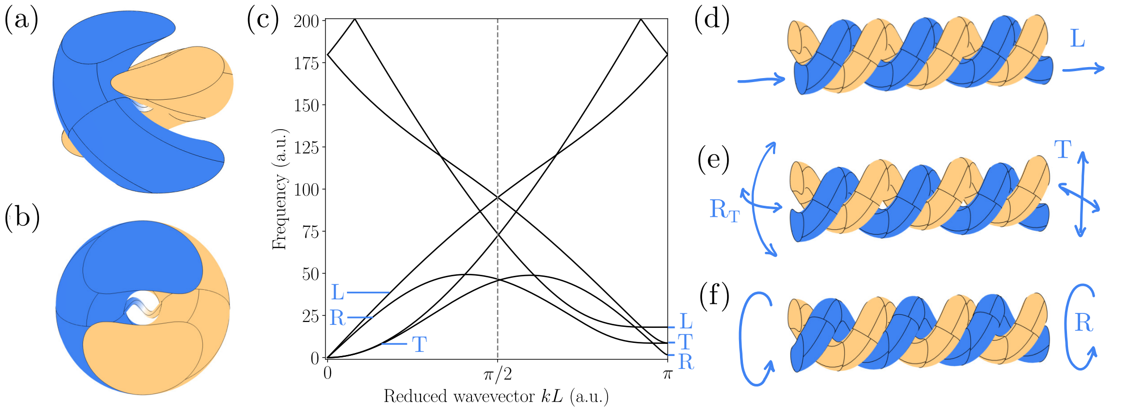

Figure 7.1: Nonlocal resonances in a weakly-coupled twisted elastic chain. (a) Geometry of the unit cell, colored to highlight the two independent giant components. (b) Top view of the unit cell, with the coupling spring in the center. (c) Associated band structure, with the bands labeled according to the nature of the associated waves: L for longitudinal, T for transverse and R for torsional. (def) Zero-modes of the chain: (d) translation along the chain direction, which gives rise to longitudinal waves; (e) remaining translations and their associated rotations, which give rise to quadratically dispersive transverse waves; (f) rotation around the chain axis, giving rise to torsional waves.

the chain axis, shown in Fig.7.1(e), they can be interpreted as infinite-wavelength transverse waves. As discussed in Ch.6, these transverse waves have a quadratic dispersion relation, which allows us to also express two rotations as sums of Bloch modes in the vicinity of the Γ point. Finally, the rotation around the chain axis gives rise to a fourth dispersion branch, that of torsion waves.

Keeping these four bands in mind, we stop ignoring the second GC, which carries the same six zero-modes. The key to include it in the spectrum is to note that the blue and yellow GCs can either move in-phase or out-of-phase, with the latter case shown in Fig.7.1(d-f). Their in-phase motion yields the same four branches as in the single-GC case, as seen near the Γ point in Fig.7.1(c). As for the out-of-phase motion, it simply produces a copy of these four bands at the edge of the Brillouin zone. The presence of the small coupling spring becomes relevant again at this stage of the analysis. Indeed, much like the realistic hinges in Ch.3, the coupling spring induces mass-gaps at the basis of these four anomalous dispersion branches, as seen in the vicinity of $kL = \pi$ in Fig.7.1(c).

7.3 Permuting giant components with isometries

The idea of an elastic IWM easily generalises to higher dimensions; in a sense, these structures even require at least three spatial dimensions to achieve nontrivial interlacing patterns. Indeed, while the unit-cell of the chain only repeated along one direction, the geometry itself was three-dimensional; anything less makes it impossible to permute GCs without crossing. In this section, we will investigate a truly three-dimensional crystal and adopt a symmetry viewpoint in our design process. The key idea is to consider that symmetry operations that leave the geometry invariant may still lead to a permutation of the GCs. For instance, a rotation of π around the axis of the twisted chain of Fig.7.1 exchanges the position of the blue and yellow GC. Interpreting the GCs as a vector space on which the symmetries act then naturally leads to representations of the group of symmetries of the IWM.

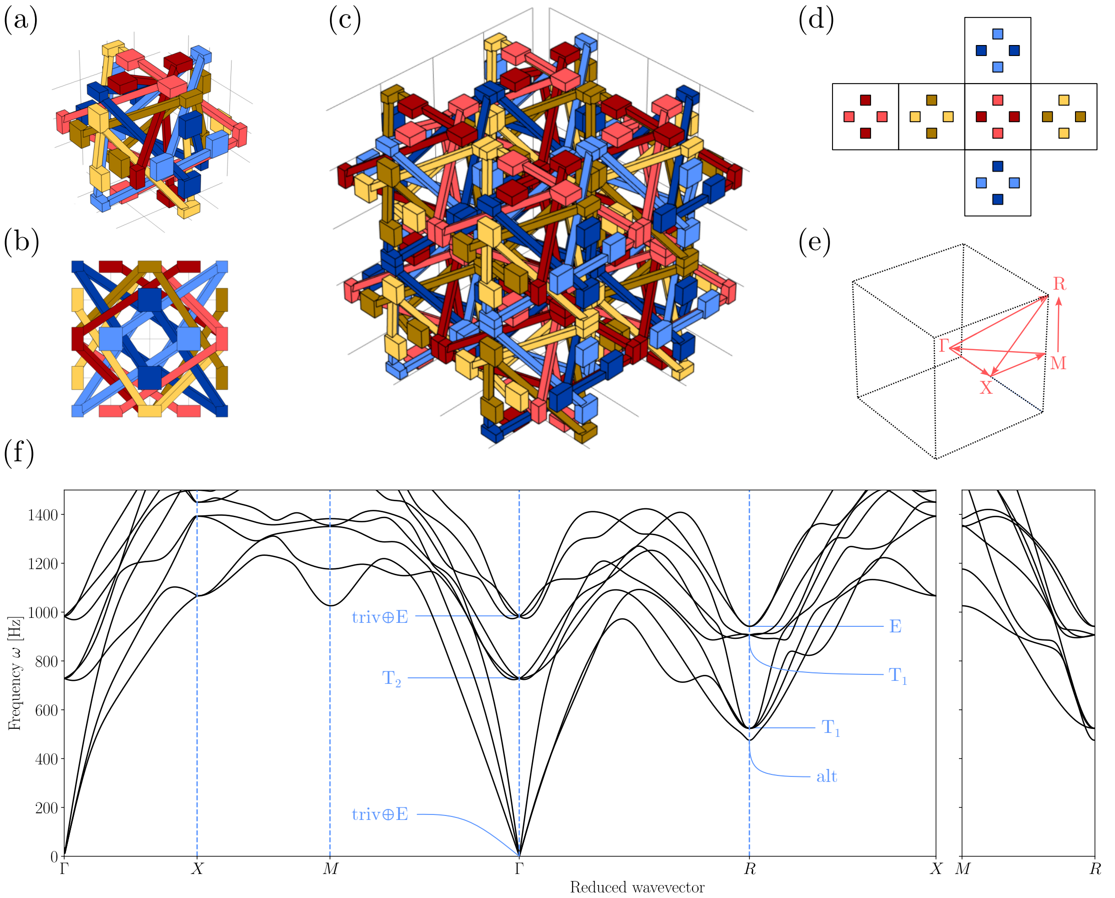

Figure 7.2: Nonlocal resonances in an interlaced 3D elastic metamaterial. (a) Geometry of the unit cell, with elements colored to highlight the six independent giant components. (b) Side view of the unit cell. (c) $2 \times 2 \times 2$ crystal demonstrating the nontrivial interlacing of the giant components. (d) Flattened surface of the unit cell, with only the four central points of each face retained to clarify the interlacing pattern. (e) Cubic Brillouin zone, with a high-symmetry path depicted in pink. (f) Phononic spectrum along the aforementioned high-symmetry path. Spectral degeneracies at the Γ and R points are labeled according to the irreducible representation that protect them.

Concretely, we consider the symmorphic space group $P432 = O \ltimes T$, whose point group O consists of the 24 rotations that leave a cube invariant. The first step in creating an elastic IWM with this symmetry is to insert a single solid domain into a cubic unit cell, for instance one of the light blue domains in Fig.7.2(ab). Then, we symmetrize the unit cell by applying the operator $\sum_{g\in O}\boldsymbol{\rho}_{xyz}(g)$ to this domain, where $\boldsymbol{\rho}_{xyz}$ is the representation of O acting on $\mathbb{R}^3$ [IX].

In this case, this yields the 12 domains[X] depicted in Fig.7.2(ab). As we start filling space with this unit cell to create a 3D crystal, such as the one shown in Fig.7.2(c), the 12 local domains connect with each other in such a way that only six disconnected GCs remain. Each colour in Fig.7.2(a-d) correspond to a different GC. Note in particular that the positions of the GCs on opposing faces of the unit cell are exchanged: this is made apparent in Fig.7.2(d), where we show the development of the cube faces on a net. There, we highlight the positions at which the GCs cross each face with colours.

The next step is to understand how the GCs are permuted under the action of the point group O; this furnishes a six-dimensional representation of O, which we will denote by $\boldsymbol{\rho}_6$. In terms of design, this is promising: we need enough GCs to have a large representation of the point group. If we only had obtained one or two GCs after the symmetrisation and tiling steps, we would already know that no interesting irrep can arise, and would select another initial domain for the whole design procedure.

In order to decompose the six-dimensional GC-swapping representation $\boldsymbol{\rho}_6$ into irreps of O, we only need one representative from each conjugacy class of O. Let us list these conjugacy classes explicitely, and then evaluate the trace of a $\boldsymbol{\rho}_6(g)$ matrix for a representative of each class. We will thus obtain a character vector $\vec{\chi}(\boldsymbol{\rho}_6)$ that we will use to find an irrep decomposition.

The first class has a single element: it consists in doing nothing. The associated character is ~~laziness~~ given by $\chi(\boldsymbol{\rho}_6(\mathbb{1})) = Tr(\mathbb{1}_6) = 6$. The second class consists of six elements, namely rotations by π around a line connecting the midpoints of two diametrically opposed edges of the cube. As a representative of this class, we pick the rotation that leaves the initial light blue domain invariant. If we denote the initial GC vector as $(\bullet\bullet\bullet\bullet\bullet\bullet)^T$, this rotation is given by the matrix

$$\boldsymbol{\rho}_6(\curvearrowleft) = \begin{pmatrix} & & & & 1 & \\ & & & & & 1 \\ & & 1 & & & \\ & & & 1 & & \\ 1 & & & & & \\ & 1 & & & & \end{pmatrix} \Longleftrightarrow \boldsymbol{\rho}_6(\curvearrowleft)\begin{pmatrix}\bullet\\\bullet\\\bullet\\\bullet\\\bullet\\\bullet\end{pmatrix} = \begin{pmatrix}\bullet\\\bullet\\\bullet\\\bullet\\\bullet\\\bullet\end{pmatrix}, \tag{7.3}$$

which yields $\chi(\boldsymbol{\rho}_6(\curvearrowleft)) = 2$. The third conjugacy class consists of three rotations by π around axes normal to the faces: picking the blue face as a representative gives us the matrix

---

[IX] $\boldsymbol{\rho}_{xyz}$ simply contains the 24 appropriate 3×3 rotation matrices.

[X] Not 24, because the initial domain was already invariant under a rotation by π around a line connecting the midpoints of two opposing edges of the cube.

$$\boldsymbol{\rho}_6(\circlearrowleft\Box) = \begin{pmatrix} & 1 & & & & \\ 1 & & & & & \\ & & 1 & & & \\ & & & 1 & & \\ & & & & & 1 \\ & & & & 1 & \end{pmatrix} \Longleftrightarrow \boldsymbol{\rho}_6(\circlearrowleft\Box)\begin{pmatrix} \textcolor{red!70!black}{\bullet} \\ \textcolor{red!60}{\bullet} \\ \textcolor{blue!70!black}{\bullet} \\ \textcolor{blue!50}{\bullet} \\ \textcolor{yellow!60!black}{\bullet} \\ \textcolor{yellow!70}{\bullet} \end{pmatrix} = \begin{pmatrix} \textcolor{red!60}{\bullet} \\ \textcolor{red!70!black}{\bullet} \\ \textcolor{blue!70!black}{\bullet} \\ \textcolor{blue!50}{\bullet} \\ \textcolor{yellow!70}{\bullet} \\ \textcolor{yellow!60!black}{\bullet} \end{pmatrix}, \tag{7.4}$$

also leading to $\chi(\boldsymbol{\rho}_6(\circlearrowleft\Box)) = 2$. In the fourth conjugacy class, we find eight rotations by $\pm 2\pi/3$ around the four main diagonals of the cube. Picking a representative corner yields the matrix

$$\boldsymbol{\rho}_6(\circlearrowleft\mathsf{Y}) = \begin{pmatrix} & & 1 & & & \\ & & & 1 & & \\ & & & & 1 & \\ & & & & & 1 \\ 1 & & & & & \\ & 1 & & & & \end{pmatrix} \Longleftrightarrow \boldsymbol{\rho}_6(\circlearrowleft\mathsf{Y})\begin{pmatrix} \textcolor{red!70!black}{\bullet} \\ \textcolor{red!60}{\bullet} \\ \textcolor{blue!70!black}{\bullet} \\ \textcolor{blue!50}{\bullet} \\ \textcolor{yellow!60!black}{\bullet} \\ \textcolor{yellow!70}{\bullet} \end{pmatrix} = \begin{pmatrix} \textcolor{blue!70!black}{\bullet} \\ \textcolor{blue!50}{\bullet} \\ \textcolor{yellow!60!black}{\bullet} \\ \textcolor{yellow!70}{\bullet} \\ \textcolor{red!70!black}{\bullet} \\ \textcolor{red!60}{\bullet} \end{pmatrix}, \tag{7.5}$$

this time leading to a character of $\chi(\boldsymbol{\rho}_6(\circlearrowleft\mathsf{Y})) = 0$. Finally, the last 6 elements of the group are rotations by $\pm\pi/2$ around the three axes normal to the faces; picking the blue face again, we get

$$\boldsymbol{\rho}_6(\hookleftarrow\Box) = \begin{pmatrix} & & & & 1 & \\ & & & & & 1 \\ & & & 1 & & \\ & & 1 & & & \\ 1 & & & & & \\ & 1 & & & & \end{pmatrix} \Longleftrightarrow \boldsymbol{\rho}_6(\hookleftarrow\Box)\begin{pmatrix} \textcolor{red!70!black}{\bullet} \\ \textcolor{red!60}{\bullet} \\ \textcolor{blue!70!black}{\bullet} \\ \textcolor{blue!50}{\bullet} \\ \textcolor{yellow!60!black}{\bullet} \\ \textcolor{yellow!70}{\bullet} \end{pmatrix} = \begin{pmatrix} \textcolor{yellow!60!black}{\bullet} \\ \textcolor{yellow!70}{\bullet} \\ \textcolor{blue!50}{\bullet} \\ \textcolor{blue!70!black}{\bullet} \\ \textcolor{red!70!black}{\bullet} \\ \textcolor{red!60}{\bullet} \end{pmatrix}, \tag{7.6}$$

which also leads to a character of $\chi(\boldsymbol{\rho}_6(\hookleftarrow\Box)) = 0$. Collecting these characters in a single vector, we obtain

$$\vec{\chi}(\boldsymbol{\rho}_6) = (6,2,2,0,0)^T = \vec{\chi}(triv) + \vec{\chi}(E) + \vec{\chi}(T_1). \tag{7.7}$$

where we decomposed the character vector $\vec{\chi}(\boldsymbol{\rho}_6)$ as a sum of column vectors from the character table of the O cubic point group, given in Tab.7.2. This, in turn, allows us to deduce the

Table 7.2: Character table of the O cubic point group. Each column corresponds to an irreducible representation, and each row to a conjugacy class. The first column lists the number of elements within the conjugacy class.

	triv	alt	E	T_1	T_2
𝟙	1	1	2	3	3
↶⫯	1	-1	0	1	-1
⤹□	1	1	2	-1	-1
⤹Y	1	1	-1	0	0
↲□	1	-1	0	-1	1

irrep decomposition $\boldsymbol{\rho}_6 = triv \oplus E \oplus T_1$. If we were in an electromagnetic setting, we could stop our point-group analysis right here, and skip directly to the band structure aspects of the design process, because each GC carries a single scalar electric potential which does not transform under the point group operation. In our present elastic setting, however, we have to carry on a bit longer to account for the vectorial nature of the displacement field $\vec{u}$, which transforms nontrivially under the action of O.

We leave it to the reader to follow the procedure outlined above to prove that $\boldsymbol{\rho}_{xyz} = triv \oplus E$. Since, like the axes, the displacement field also transforms under $\boldsymbol{\rho}_{xyz}$, we can deduce that the 18 independent displacement components carried by our six GCs transform under the representation $\boldsymbol{\rho}_6 \otimes \boldsymbol{\rho}_{xyz} = (triv \oplus E \oplus T_1) \otimes (triv \oplus E)$. We can easily compute the character vector associated to this representation using the relation $\chi(\boldsymbol{\rho}_6(g) \otimes \boldsymbol{\rho}_{xyz}(g)) = \chi(\boldsymbol{\rho}_6(g))\chi(\boldsymbol{\rho}_{xyz}(g))$, which we can again express as a sum of character vectors of the irreps, found in Tab.7.2. We can then deduce that the $\boldsymbol{\rho}_6 \otimes \boldsymbol{\rho}_{xyz}$ admits the irrep decomposition

$$\boldsymbol{\rho}_6 \otimes \boldsymbol{\rho}_{xyz} = (triv \oplus E \oplus T_1) \otimes (triv \oplus E) = 2(triv \oplus E) \oplus T_2 \oplus alt \oplus 2T_1 \oplus E. \tag{7.8}$$

What is this decomposition good for ? Well, it contains several higher-dimensional irreps of O, which should impact the irreps of the full space group $P432$ and therefore show up in the band structure as symmetry-protected spectral degeneracies. To see them clearly, we introduce a coupling spring between two GCs and symmetrise it with the operator $\sum_{g \in O} \boldsymbol{\rho}_{xyz}(g)$, to preserve the $P432$ symmetry. We do so at a location that fully connects the GCs as a result. As discussed in Sec.7.2, this should give rise to mass-gaps, giving finite frequencies to 15 out of the 18 zero-modes present in the decoupled system. The remaining three modes correspond to the three DOFs of continuum elasticity.

To obtain the corresponding band structure, we then set up an eigenfrequency FEM simulation in COMSOL with Floquet-Bloch boundary conditions between opposing faces of the unit cell. We then sweep the wavevector over the high-symmetry path shown in Fig.7.2(e), which results in the band structure depicted in Fig.7.2(f). There, we see six gapped bands at the Γ point and nine at the R point. As promised, these bands exhibit symmetry-protected degeneracies, which are labeled with the relevant irreps of the O group. In particular, there are irrep-protected threefold spectral degeneracies both at the Γ point and at the R point.

As discussed in Sec.7.1, the irreps also teach us something about the symmetries of the associated modes. Forming mental pictures of the action of each irrep helps in understanding these modal symmetries better. Let us consider the alt irrep as our first example. Imagine the biggest tetrahedron that can be inscribed in a cube. Then, consider its dual, which is also inscribed in the cube. The permutations of these two tetrahedra under the action of group elements furnish a two-dimensional representation of O. Restricting the underlying vector space to its antisymmetric sector, we get a geometrical object that transforms under the alt irrep, namely an antisymmetric sum of the two tetrahedra. The displacement profile of the non-degenerate mode at the R point transforms in the same way !

Similarly, since that the modes at $triv \oplus E$ degeneracies transform like orthonormal axes, we can remove the symmetric sector from the axes vector space to obtain an explicit 2D vector space of geometrical objects that transforms under E, spanned by antisymmetric combinations of two axes. We can keep playing the same game for the other irreps, for instance by noting that the main diagonals of the cube transform as $triv \oplus T_2$ and removing the symmetric sector. This provides the seed for a mental picture of how the deformation modes that occur at each spectral degeneracy transform under the action of O.

A more precise algebraic approach, which does not depend on geometric intuition[XI], consists in explicitly finding the irrep basis transformation which block-diagonalises $\boldsymbol{\rho}_6 \otimes \boldsymbol{\rho}_{xyz}$. This tells us precisely which displacement profiles are associated to each irrep. We could then also analyse these displacement profiles to assign the irrep-protected spectral degeneracies to the proper wavevectors before explicitly computing the band structure.

To add one last instrument in our design toolbox, we want to emphasise the connection between the location of the coupling spring, the modal profiles, and the height of the mass gaps. Leveraging our knowledge of the modal profiles is indeed the key to open mass gaps in a controlled way: in the same spirit as the discriminant hinges of Ch.4, a well-positioned spring can preferentially frustrate the modes associated to a particular irrep, hence opening a larger mass gap for these branches. Doing this with enough precision, we could potentially lift most irrep degeneracies to higher frequencies, keeping only a degeneracy of interest in the low-frequency spectrum.

[XI] *“Algebra is the offer made by the devil to the mathematician. The devil says: ‘I will give you this powerful machine, it will answer any question you like. All you need to do is give me your soul: give up geometry and you will have this marvellous machine.’ ”* (M. Atiyah)

7.4 Conclusion

As we have seen in Sec.7.1, symmetry considerations make many aspects of wave physics in crystals conceptually clearer. For one thing, they contain Bloch's theorem as a special case, and extend its logic to other isometries preserving the crystal. On a practical level, this approach also allows us to write dynamical equations in a particularly nice basis, in which the displacements are decoupled into symmetrical subsectors. Concretely, it made it much easier to analytically treat symmetric chain models, like the one given in Eq.(3.5). Given the high symmetry of the underlying geometry, it would certainly also make a matrix like the one given in Eq.(3.8) much more tractable. Another selling point is that representation theory is particularly easy to apply to the case of elastic IWMs.

Indeed, one of the most salient features of our design process for high-symmetry elastic IWMs is that we did not need to consider the symmetries and commutation properties of a differential operator explicitly, unlike in Sec.7.1. Instead, we leveraged our *a priori* knowledge of the zero-modes carried by the GCs to directly study the relevant representation of the point-group O. The symmetry protection provided by the irreps then ensured that the spectral degeneracies survived the promotion of zero-modes to soft modes.

However elegant it may seem, this approach remains a design tool and comes with limitations. For one thing, in the preceding analysis, we hid rotational zero-modes under the carpet. As discussed in Ch.6, the rotation DOFs have a spatial profile incompatible with a pure Bloch mode shape. It would be interesting to uncover their spectral signature, in particular in the continuum elasticity limit, for which tricks from Ch.6 do not seem to work as is.

A second issue with the symmetry approach is that space-group symmetries are rather easily broken in practice[XII]. This means trouble for the degeneracies they protect. Like the kinematic graph method we introduced in Ch.2, we should take symmetry aspects with a grain of salt: compromise and imperfections will necessarily come up in the manufacturing process and break the strict applicability of the method. Starting the design process with kinematic graphs or symmetry provides powerful mental pictures on which we can anchor second-order effects like mass gaps and symmetry-breaking. Keeping this in mind, one can use these design tools to produce architected media in which waves propagate in unusual and wonderful ways.

[XII] One could even say that they are *spontaneously* broken in some cases.

8 Discussion and Outlook

> *"La mer jusqu'à l'approche de ses limites est une chose simple qui se répète flot par flot. Mais les choses les plus simples dans la nature ne s'abordent pas sans y mettre beaucoup de formes, faire beaucoup de façons, les choses les plus épaisses sans subir quelque amenuisement. C'est pourquoi l'homme, et par rancune aussi contre leur immensité qui l'assomme, se précipite aux bords ou à l'intersection des grandes choses pour les définir"*
>
> — F. Ponge

8.1 What we explored

In this section, we summarise and discuss our research findings.

8.1.1 A design pathway based on nonlocal resonances

In this thesis, we introduced a third design path to control elastic waves in architected media, distinct from phononic crystals and locally-resonant metamaterials, which we discussed in Ch.1. The central concept of our method consists in designing nonlocal resonances, *i.e.* zero-frequency modes with non-zero wave-vectors. Nonlocal resonances heavily impact wave propagation by introducing anomalous dispersion cones in the spectrum.

In Ch.2, we introduced kinematic graphs, a convenient, visual design tool for zero-energy modes in elastic metamaterials. Under the same small-displacements assumption as linear elasticity theory, kinematic graphs distillate the search for global degrees of freedom into a minimal combinatorial problem. Using this tool, we identified various classes of zero-mode scaling in flexible metamaterials, and then zeroed in on the oligomodal class. This class of elastic metamaterials, which we introduced in [141], is characterised as hosting a fixed number of global deformation modes that does not scale with system size.

Inspired by IWMs, we then added a Bloch-wave requirement on the modes hosted by oligo-

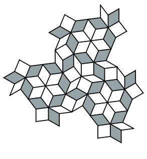

modal geometries, thereby defining the notion of nonlocal resonance. We explored the wave physics of these objects in Ch.3 using dynamical models and full-wave simulations. There, we emphasised the negative-index properties of anomalous cones and introduced an inverse design method to move such cones at arbitrary locations in k-space.

Finally, we completed our first design cycle in Ch.4, wherein we reported compression and vibration experiments that we performed to anchor oligomodal geometries and nonlocally-resonant metamaterials in reality. In the process, we made a small detour to discuss a more mechanical perspective on oligomodality, which can also be leveraged to achieve complex shape-morphing properties and mechanical multifunctionality.

8.1.2 A map of boundaries

Having established our core concept, we started charting out its boundaries, both on the practical and theoretical level.

First, we contextualised the various nonlocally-resonant structures we studied along the way within the landscape of architected media we explored in Ch.1. To do this, we updated the state-of-the-art of Fig.1.5 by including our own designs, a process that resulted in Fig.8.1. As discussed in the introduction, the traditional designs form a continuum, with an inherent trade-off between bandwidth and subwavelengthness. Nonlocally-resonant metamaterials, colour-coded in violet, clearly escape this limitation. They are able to do so because their working principle does not rely on a collection of somewhat isolated local units, but rather on the entire material acting in concert.

With the benefit of hindsight, we were able to uncover the signatures of nonlocal resonances in a few elastic architected media from the existing literature, even though only one of them directly tackled negative-index properties. The latter is a rotator metamaterial studied in Ref.[221], in which a wave perspective on the counter-rotating squares mechanism is adopted. This explicit wave treatment allowed us to include this study as a data point in Fig.8.1, within the nonlocally-resonant group. As for the two other studies, they are focused on other physical properties but exhibit clear signatures of nonlocal resonance.

The first study [34] aims to create wide band gaps using crystals of cubically-packed and densely-packed spheres, with hinge-type connections. The associated band structures clearly exhibit anomalous cones, but the authors do not discuss them. Instead, they attribute the width of their band gaps to an interplay of the Bragg and local-resonance mechanisms. In line with our discussion in Sec.5.3, we surmise that the hybridisation of standard dispersion cones with anomalous ones also plays a central role in the formation of these wide gaps.

The second study is dedicated to studying the topology of square Maxwell frames [202]. There, the authors clearly identify zero-frequency energy modes with nontrivial wave vectors which fit our definition of nonlocal resonance. Interpreting the associated spectral features as Weyl points, they go on to define topological charges and associated edge states, albeit also without

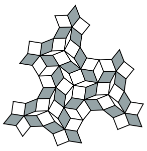

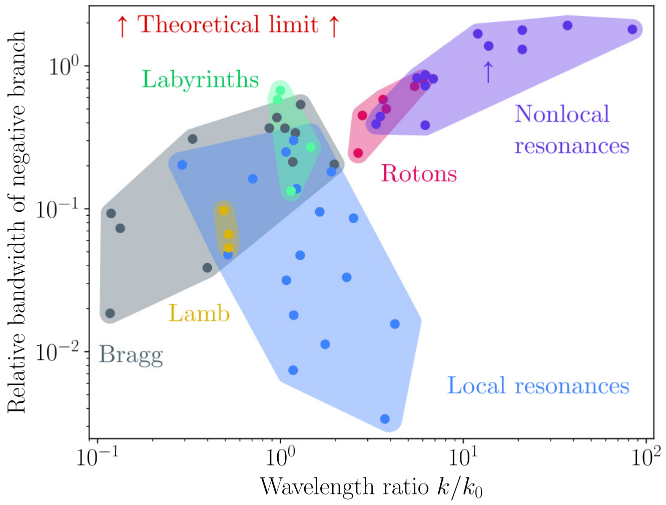

Figure 8.1: Negative index bandwidth versus subwavelength ratio k/k_0 for nonlocally-resonant metamaterials (violet), phononic crystals (grey), labyrinthine crystals (green), Lamb waves (yellow), locally-resonant metamaterials (blue) and roton metamaterials (pink). The upper edge of the plot corresponds to the theoretical maximum of relative bandwidth, namely $\Delta\omega/\omega_c = 2$. The point corresponding to the experimental band structure obtained in Sec.4.2 is indicated with an arrow.

discussing wave propagation aspects. This framework seems ideal to assign a topological charge to the edge states we uncovered in Sec.5.2 on the basis of kinematic graph arguments.

Coming back to the nonlocally-resonant structures introduced in this thesis, we note that we only included full-wave simulations and experiments among the violet data points of Fig.8.1. Our rationale is that a theoretical, non-gapped anomalous cone would simply reach the absolute maxima of both relative bandwith of the negative-index band and subwavelength ratio. In practice, the only factor that limits these metrics is the height of the mass-gap that opens at the basis of the anomalous cone, as discussed in Ch.5. This mass gap is directly related to the non-ideality of the hinges; if required, it can be reduced by optimising hinge design. Such an optimisation process would certainly hit a hard minimum at some point, even if the precise nature of this mininum is unclear for now. It is certainly influenced by technological aspects, such as manufacturing constraints, which are subject to an extremely fast-paced evolution. If this were still insufficient for a particular purpose, one could consider the inclusion of active elements, which compensate the residual mass gaps with negative stiffness.

We pursued our quest with more conceptual boundaries, relaxing some defining characteristics of nonlocal resonances and studying the resulting edge cases. In Ch.5, this approach produced a weird counterpart to the tip-blunting mass gaps, namely momentum gaps opening around nonlocal resonances. Left unchecked, such gaps correspond to exponential-growth instabilities. The boundary of such a momentum gap consists of so-called exceptional points; studying the marginally unstable temporal evolution at these points led us to realise that nonlocal resonances also exhibit exceptional-point dynamics.

Next, we progressively relaxed our Bloch wave requirement at the kinematic graph level. We did so by studying geometries whose local arrow rules were close to yielding coherent plane coverings: this combinatorial frustration also had the effect of opening mass gaps at the basis of anomalous cones. In most cases, this meant that the nonlocal resonance acquired a finite frequency. This, however, is not a necessary consequence of the mass-gap opening: some perturbed arrow-rules instead lead to the apparition of edge states. They simply disappear from the band structure, but retain their zero-frequency character.

Such states are still continuously related to Bloch waves, in the sense that we can interpret them as Bloch waves with complex-valued wavevectors. This is to be expected, since we obtained them as perturbations of nonlocal resonances. In Ch.6, we took a more radical step and considered the fate of oligomodal geometries whose zero-modes did not fit the Bloch wave requirement at all. There, we uncovered a power-law spectral signature associated to power-law displacement profiles. Interestingly, this approach also seems applicable beyond the confines of nonlocally-resonant metamaterials, for instance by providing a rotation-based interpretation of the quadratic dispersion of asymmetric Lamb waves. These power-law signatures proved useful to properly count and interpret waves in the elastic IWMs that we treated in Ch.7.

Finally, we introduced and studied elastic IWMs to better understand the interplay of symmetry with nonlocal resonances, having realised that representation theory applies very naturally to elastic IWMs. Indeed, the action of a given symmetry operation is easily represented as a permutation in the space of GCs. This also had the added benefit of allowing us to study elastic nonlocal resonances in a three-dimensional setting.

These studies on elastic IWMs are also included within the nonlocally-resonant group of Fig.8.1. Removing coupling between GCs altogether provides a practical path to ideal anomalous cones, with their associated marginal instabilities. The resulting secular growth would however quickly be stopped in its tracks by a nonlinear term taking the form of a hard-sphere interaction, preventing GCs from crossing each other. In plain terms, interlaced GCs would be free to move with respect to each other only until the amplitude of motion became large enough for them to rattle.

8.2 *Hic sunt dracones*

We now provide an outlook on future work and discuss connections to other lines of research, increasingly further away from the subject at hand, before wrapping the thesis up with some general remarks.

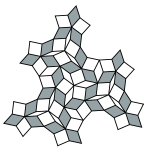

8.2.1 Metamaterials with roton-like dispersion and gapped elastic IWMs are two faces of the same coin

The overlap of the pink and violet domains in Fig.8.1 suggests a connection between nonlocal resonances and roton-like dispersion relations; we are now in a position to discuss it in more detail. In the roton-like approach, one builds in long-range interactions within a standard crystal. This produces a roton-like dip in the dispersion, which yields negative index physics. Such an approach could be characterised as “top-down”.

Our concept, like its IWM precusors, goes the other way around. Using kinematic graphs or electrostatics, we ensure the presence of a nonlocal resonance and then design the material around this requirement. Then, as seen in Ch.5, we can introduce mass gaps of varying height. This approach has a more “bottom-up” nature.

This abstract correspondence breaks down as we consider the physical mechanisms underlying electromagnetic IWMs, roton-hosting metamaterials and our planar flexible metamaterials. In particular, roton-hosting metamaterials rely on explicit long-range couplings that require three spatial dimensions. In contrast, the purely planar nature of our metamaterials demonstrates that such long-range couplings are not a logical necessity to obtain nonlocally-resonant behaviour.

To push the “top-down”/“bottom-up” correspondence further, one needs to turn to the elastic IWMs we introduced in Ch.7. Indeed, the correspondence also holds at the level of the underlying physics for this class of nonlocally-resonant metamaterials. To see the “top-down” correspondence, consider the limit in which the nontrivial long-range couplings largely dominate the short range ones. What we’re left with is essentially an elastic IWM, containing disconnected GCs that are held together by strong long-range couplings. In the opposite, “bottom-up” direction, we can take an elastic IWM and weakly couple its GCs, as we did in Ch.7. By increasing this GC coupling, we can make increase the mass gap and therefore make the dispersion more roton-like.

8.2.2 Continuum theories for nonlocally-resonant metamaterials

In this thesis, we reported our efforts on microstructural design, and did not pursue effective continuum descriptions. The interesting question of obtaining an effective continuum model of nonlocally-resonant metamaterials remains open. Standard long-wavelength elasticity is certainly inadequate, since it would fail to capture anomalous cones. On top of that, the presence of internal rotating elements probably indicates a need for nonstandard continuum elasticity theories, such as Cosserat or micropolar elasticity.

Looking at minimal anomalous dispersions like Eq.(3.6) suggests that higher-derivative terms need to be included in any effective theory that hopes to treat standard and anomalous waves simultaneously. We made a minimal phenomenological attempt by extending a 1D wave equation with spatial derivatives of up to fourth order. Making a plane-wave Ansatz then yields a dispersion relation with encouraging features. For instance, by varying the weights of the various spatial terms, one can get a zero-frequency solution with nonzero wavevector. This amounts to solving the equation $\omega(k)^2 = 0$ and enforcing degenerate roots. Two distinct real roots lead to a momentum gap and a pair of conjugate complex roots leads to a mass gap.

A proper treatment of this problem necessitates a form of homogenisation; in that regard, the presence of two competing lengthscales of equal importance – the standard-elastic and anomalous lengthscales – is intriguing.

8.2.3 Entering the nonlinear regime

One of the earliest obstacles we faced, namely the geometric nonlinearity we encountered in Fig.2.2, actually constitutes a great advantage of the elastic platform compared to say acoustics or microwaves. Indeed, we can easily enter the nonlinear regime through the gate of geometric nonlinearities, a feat much harder to achieve in other physical platforms. We now report a slight foray in the nonlinear regime, to motivate further research in that direction. Some studies [254–258] have started exploring this regime, uncovering transition waves and soliton behaviour, among a wealth of other nonlinear phenomena. We propose a different entry point in the nonlinear regime: it is based on a defining characteristic of nonlocally-resonant metamaterials, namely the finite number of global mechanical DOFs they host.

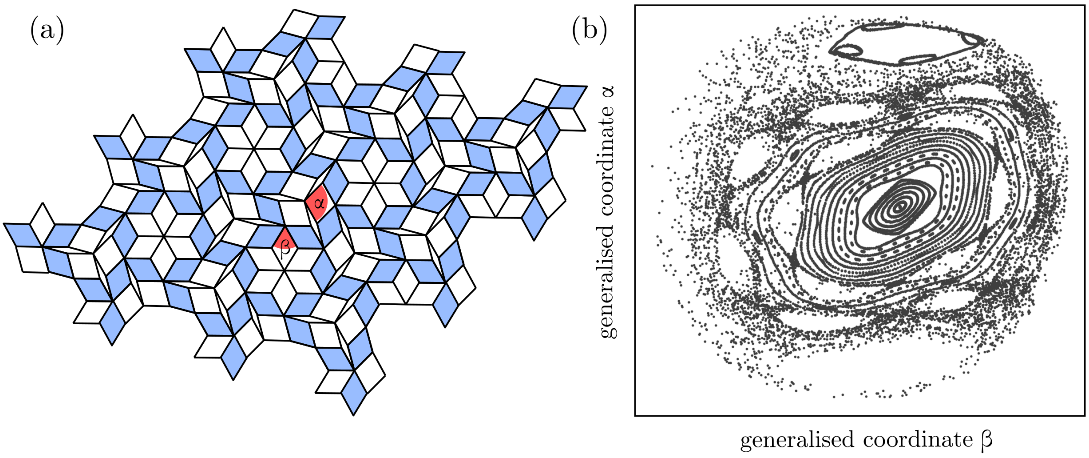

Figure 8.2: Poincaré section of a 2-DOF nonlinear hamiltonian model. (a) Patch of metamaterial modelled, with the generalised coordinates α and β indicated in red. (b) corresponding Poincaré section, with the reference surface defined through vanishing generalised momenta.

This suggests an alternative way to include dynamics, without relaxing the rigid-bar assumption of kinematic graph theory. We can instead associate a generalised coordinate to each global zero-mode, for instance the two angles highlighted in red in Fig.8.2(a). We then write down a Hamiltonian for the finite patch of Fig.8.2(a), assigning torsional elastic energy to the hinges to get some restoring forces. Integrating the resulting equations of motion with a fourth-order Runge-Kutta scheme then yields the Poincaré section depicted in Fig.8.2(b). The intercepting surface in this section was defined by making both generalised momenta vanish. The results are typical of Hamiltonian chaos. Indeed for small angles, one sees a somewhat regular foliation of the phase space, while outer regions are ripe with hyperbolic points and irregular orbits.

This preliminary distributed-pendulum study raises interesting questions. For instance, does this chaotic behaviour qualitatively survive relaxing the rigidity assumptions ? How would chaos manifest itself on the wave level ? If chaos does survive, is it connected to the oligomodality of the underlying geometry ? Other nonlinear effects would certainly enter the fray, and one should keep an open mind for phenomena that we did not anticipate, irrespective of our entry point in that fascinating realm.

8.2.4 Potential connections to condensed-matter physics

Ideal, non-gapped nonlocal resonances are marginally unstable, as discussed in Sec.5.1. This suggests a path towards extreme negative-index behaviour induced at the atomic scale. Indeed, one could search for materials close to a single-DOF structural instability through databases and existing literature. The concept of nonlocal resonance then suggests that such a material should support additional negative-index waves on top of the standard waves of continuum elasticity, which may open the way to highly miniaturised negative-index devices. But instead of asking ourselves what condensed-matter physics can do for us, we should maybe think about what we can do for condensed-matter physics.

Indeed, an intriguing idea has been put forward in the context of high-temperature supraconductivity [259–261], connecting a phonon-softening phenomenon with an increase of the critical temperature. Concretely, in [259], the authors add a gaussian dip in the phonon dispersion “manually” at a nonzero wavevector, and then use Migdal-Eliashberg theory to predict that this leads to increased electron–phonon coupling and higher critical temperature. While they mention the formation of charge-density waves as a potential driver of phonon softening, their theoretical treatment remains agnostic as to the phenomenon causing the phonon softening.

In particular, their effective approach does not provide a concrete underlying microstructure. This is a long shot, but our theory could provide an unusual designer-like vantage point on such questions, providing tools to create nonlocally-resonant microstructures instead of adding dispersion minima manually.

8.3 Conclusion

In this thesis, we systematically studied the peculiar physics associated to nonlocal resonances, uncovering a vast landscape of wave phenomena that are not subject to the same limitations as traditional architected wave media.

The concept of nonlocal resonance has the potential to unify interlaced wire media, extreme roton dispersions and oligomodal metamaterials by identifying their common abstract core. This name emphasises the essential ingredient that underlies anomalous dispersion cones, namely a delocalised low energy mode with a nontrivial wavevector.

A Proof of lattice-integer relation

We start by proving that if the nodes of a four-bar linkage sit on a Bravais lattice, the resulting arrow weights can be written as integers. Let $\vec{v}, \vec{w} \in \mathbb{R}^2$ be the basis vector of said lattice. Then, the ith bar in the linkage can be written in the form $\vec{z}_i = n_i \vec{v} + m_i \vec{w}$, where $n_i, m_i \in \mathbb{Z}$. As a consequence of the area law, we know that any arrow weight α, up to a sign, can be written in the form $\alpha = \vec{z}_i \times \vec{z}_j$. Inserting the lattice condition, this yields $\alpha = \vec{z}_i \times \vec{z}_j = (n_i \vec{v} + m_i \vec{w}) \times (n_j \vec{v} + m_j \vec{w}) = (n_i m_j - m_i n_j) \vec{v} \times \vec{w}$. Dividing all arrow weights by the area of the lattice unit-cell, we get $\alpha / (\vec{v} \times \vec{w}) = n_i m_j - m_i n_j \in \mathbb{Z}$.

We now prove the converse: if the arrow weights are integer numbers, the nodes must sit on a Bravais lattice. To see this, define $\vec{v} := \vec{z}_1 / (\vec{z}_1 \times \vec{z}_2)$, $\vec{w} := \vec{z}_1 / (\vec{z}_1 \times \vec{z}_2)$, $n := \vec{z}_3 \times \vec{z}_2$, $m := \vec{z}_2 \times \vec{z}_1 + \vec{z}_4 \times \vec{z}_1$ and $p := \vec{z}_1 \times \vec{z}_2$. Without loss of generality, we can rescale the dimensions of the linkage uniformly such that the triangle areas are integer numbers, by hypothesis and application of the area law. This implies $m, n, p \in \mathbb{Z}$. We then note that $\vec{z}_1 = p\vec{v}$ and $\vec{z}_2 = p\vec{w}$. We also have

$$\begin{aligned}\vec{z}_3 = \frac{(\vec{z}_1 \times \vec{z}_2)\vec{z}_3}{\vec{z}_1 \times \vec{z}_2} = \frac{-(\vec{z}_2 \times \vec{z}_3)\vec{z}_1 - (\vec{z}_3 \times \vec{z}_1)\vec{z}_2}{\vec{z}_1 \times \vec{z}_2} &= -\frac{\vec{z}_2 \times \vec{z}_3}{\vec{z}_1 \times \vec{z}_2}\vec{z}_1 + \frac{\vec{z}_1 \times \vec{z}_3 + \vec{z}_1 \times \vec{z}_2}{\vec{z}_1 \times \vec{z}_2}\vec{z}_2 - \frac{\vec{z}_1 \times \vec{z}_2}{\vec{z}_1 \times \vec{z}_2}\vec{z}_2 \\ &= \frac{\vec{z}_2 \times \vec{z}_3}{\vec{z}_1 \times \vec{z}_2}\vec{z}_1 - \frac{\vec{z}_1 \times \vec{z}_4}{\vec{z}_1 \times \vec{z}_2}\vec{z}_2 - \frac{\vec{z}_1 \times \vec{z}_2}{\vec{z}_1 \times \vec{z}_2}\vec{z}_2 = n\vec{v} + m\vec{w}\end{aligned}$$

so the vector joining any pair of hinges can be expressed as a linear combination of $\vec{v}$ and $\vec{w}$, thus completing the proof that arrow weights can be expressed as integer numbers if and only if the hinges can be placed on a Bravais lattice. ■

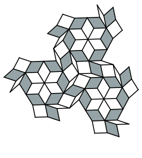

B Details of the inverse design method

This appendix is directly lifted from the Supplementary Material of [142], up to slight formatting changes.

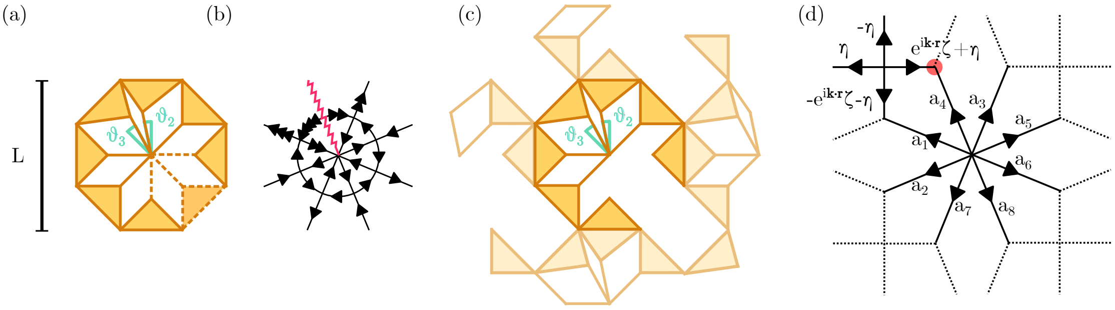

Figure B.1: (a) Geometry of inversely-designed unit cell, with the tuning angles indicated in green. Connections depicted with dashed lines will later be removed. (b) Vertex model of the unit cell mechanism for generic tuning angles. The incompatibility of the constitutive linkages is indicated with a red line. (c) Unit cell in the metamaterial, with frustrating connections removed and neighboring unit cells depicted in reduced opacity. (b) Corresponding arrow weights on a directed graph, with $a5 = -(\sqrt{2}-1)\zeta + \xi - a3$, $a6 = -(\sqrt{2}+1)\xi - a4$, $a7 = (\sqrt{2}-1)\zeta - \xi - a2$ and $a8 = (\sqrt{2}+1)\xi - a1$.

The inverse design procedure described in the main text allows us to tune the unit cell geometry to induce a prescribed shift of the anomalous cone to an arbitrary position in k-space. We now provide the computational details of this procedure, applied to the case of the octagonal unit cell shown in Fig.3.8(b). We know that this graph exhibits an anomalous cone at the M point, and our goal is to move it to a controlled location. To obtain the necessary degrees of freedom, we allow two geometric parameters to vary, namely the two angles θ_2 and θ_3 indicated in Fig.B.1(a). In Fig.B.1(b), we see that trying to propagate arrows on the graph of this modified unit cell typically leads to incompatible configurations (red zigzag line). The mechanism becomes frustrated as we lift the octagonal symmetry, which was making some of the link constraints redundant. In order to compensate for this increase in the number of effective constraints, we remove four links from the unit cell (the dashed ones in Fig.B.1(a)).

We then consider the compatibility of the unit cell-mechanism with neighboring cells within the crystal, which are depicted in Fig.B.1(c). They must deform together following the Floquet-Bloch boundary conditions, which we enforce by considering arrow conservation at hinges on the unit-cell boundary. For instance, consider the hinge highlighted in red in Fig.B.1(d), where three edges meet. There, the sum of arrows is given by $a_4 + e^{ik_yL}a_7 + e^{ik_xL+ik_yL}\zeta + \eta = 0$. We collect all such arrow-conservation equations in the matrix

$$\begin{pmatrix} 0 & -1 & 0 & \cos(\tilde{k_x}) & \cos(\tilde{k_x}) & -\sin(\tilde{k_x}) & -1 & 0 & 1 & 0 \\ 0 & 0 & 0 & \sin(\tilde{k_x}) & \sin(\tilde{k_x}) & \cos(\tilde{k_x}) & 0 & -1 & 0 & 1 \\ -1 & 0 & \cos(\tilde{k_x}) & 0 & \cos(\tilde{\kappa}) & -\sin(\tilde{\kappa}) & \sqrt{2}+1 & 0 & -\sqrt{2}-1 & 0 \\ 0 & 0 & \sin(\tilde{k_x}) & 0 & \sin(\tilde{\kappa}) & \cos(\tilde{\kappa}) & 0 & \sqrt{2}+1 & 0 & -\sqrt{2}-1 \\ 0 & \cos(\tilde{k_y}) & 0 & -1 & -\cos(\tilde{\kappa}) & \sin(\tilde{\kappa}) & -\sqrt{2}-1 & 0 & 0 & 0 \\ 0 & \sin(\tilde{k_y}) & 0 & 0 & -\sin(\tilde{\kappa}) & -\cos(\tilde{\kappa}) & 0 & -\sqrt{2}-1 & 0 & 0 \\ \cos(\tilde{k_y}) & 0 & -1 & 0 & -\cos(\tilde{k_y}) & \sin(\tilde{k_y}) & 1 & 0 & \cos(\tilde{k_x})+\sqrt{2}-1 & \sin(\tilde{k_x}) \\ \sin(\tilde{k_y}) & 0 & 0 & 0 & -\sin(\tilde{k_y}) & -\cos(\tilde{k_y}) & 0 & 1 & -\sin(\tilde{k_x}) & \cos(\tilde{k_x})+\sqrt{2}-1 \end{pmatrix}$$

where the variables $\tilde{k_x} := k_yL$, $\tilde{k_y} := k_yL$ and $\tilde{\kappa} := \tilde{k_x} + \tilde{k_y}$ correspond to the components of the wavevector at which we want to create an anomalous cone. The components of the vectors upon which this matrix acts correspond to arrow weights in the vertex model. Our objective is to find the kernel of this matrix, which by design corresponds to abstract sample-spanning mechanisms with the spatial periodicities of the target Bloch wave. As an example, the arrow configuration depicted in Fig.3(d) of the main text was obtained in this way. Such vectors have the form

$$\begin{pmatrix} a_1 & a_2 & a_3 & a_4 & \Re(\eta) & \Im(\eta) & \Re(\xi) & \Im(\xi) & \Re(\zeta) & \Im(\zeta) \end{pmatrix}, \tag{B.1}$$

where the components are assigned as in Fig.B.1(d). Note that the a_i parameters must have the same complex phase, since they move in concert; we can therefore set them all to be real and only consider the relative phases that may be picked up by the arrow weights η, ξ and ζ. Having found two such vectors (our matrix has two more columns than rows), the second step of the method begins; we need to find geometric parameters that produce arrow rules compatible with the null vectors we identified. For the particular class of deformations we chose, only a_1, a_2, a_3 and a_4 depend on the geometric parameters. Since the norm of the arrow vector is arbitrary, we can normalize three of these arrow weights with respect to the first and obtain

$$\begin{pmatrix} a_2(w)/a_1(w) \\ a_3(w)/a_1(w) \\ a_4(w)/a_1(w) \end{pmatrix} = \begin{pmatrix} \sin\left(\frac{\pi}{8}\right)(-\csc(\theta_2))\sec\left(\theta_3+\frac{\pi}{8}\right)\sin(\theta_2-\theta_3) \\ -\cos\left(\theta_2+\frac{\pi}{8}\right)\csc(\theta_2)\sin\left(\theta_3+\frac{\pi}{4}\right)\sec\left(\theta_3+\frac{\pi}{8}\right) \\ \sqrt{\sqrt{2}+2}\cos\left(\theta_2+\frac{\pi}{8}\right)\csc(\theta_2)\cos\left(\frac{\pi}{8}-\theta_3\right)\sec\left(\theta_3+\frac{\pi}{8}\right) \end{pmatrix},$$

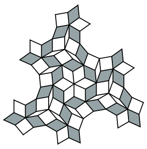

in which the parameter w encodes the linear combination of the two null vectors we found in the kernel of the boundary-condition matrix. This system can then be numerically solved for w, θ_2 and θ_3, yielding a geometry with the desired nonlocal resonance. This can be verified by removing the scaffolding and directly computing the band structure for this inversely-designed geometry, as we did in the main text.

C Fractal spectrum in quasicrystals

In the main body of this thesis, we covered the dynamical behaviour of three out of the four zero-mode scaling classes uncovered in Ch.2. Indeed, we treated the oligomodal case at length in Chapters 3 and 6, and briefly touched upon the plurimodal case in Fig.3.3. As mentioned there, the latter class is covered extensively in other parts of the flexible metamaterials literature. Regarding the more generic rigid class, we mentioned that it can be treated with standard continuum elasticity at low frequencies, noting that the origin of the resulting transverse and longitudinal waves can be traced back to the rigid translation modes of the medium.

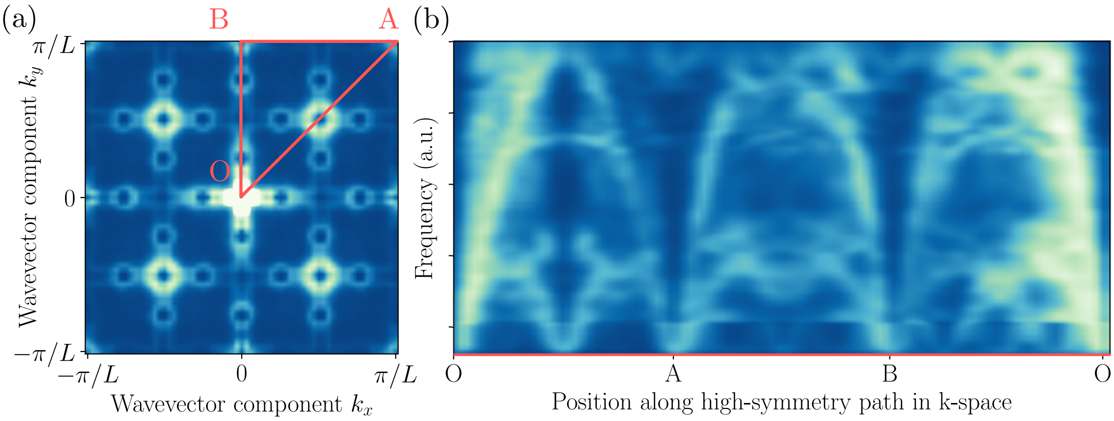

Figure C.1: Spectrum of a quasicrystalline oligomodal metamaterial with 32 × 32 cells. (a) Spatial FFT of a low-frequency mode, with a high-symmetry path indicated in red. (b) Normalized spectrum along the high-symmetry path, confirming the presence of multiple anomalous cones.

For completeness, we now discuss wave propagation in a structure belonging to the fourth class, which is characterised by its logarithmically-scaling number of zero-modes. The absence of periodic order that characterises members of that class prevents us from applying band structure theory. In the absence of this tool, we fall back to the study of finite systems and consider a 32×32 version of the quasicrystal depicted in Fig.2.10. We diagonalise the associated dynamical matrix and apply a spatial FFT to the resulting mode profiles. This results in the spectrum depicted in Fig.C.1.

Several sets of dispersion cones appear. Like the underlying modes, these cones appear at different scales. This is particularly striking in Fig.C.1, where some nested cone structures are apparent. To push the analysis further, a potential angle of attack would be to interpret the fractal substitution rule as a symmetry operation, allowing us to apply group theory. This might improve our understanding of such spectra, and also potentially allow us to study infinite structures instead of finite metamaterial patches.

Bibliography

[1] A. Dudle, “DXA- and QCT-based modeling of the human proximal femur towards improved hip fracture prediction”, PhD thesis (Universität Bern, 2023).

[2] R. Lakes, “Materials with structural hierarchy”, en, Nature **361**, 511–515 (1993).

[3] E. O. Hall, “The Deformation and Ageing of Mild Steel: III Discussion of Results”, en, Proc. Phys. Soc. B **64**, 747–753 (1951).

[4] N. J. Petch, “The Cleavage Strength of Polycrystals”, en, Journal of the Iron and Steel Institute **174**, 25–28 (1953).

[5] T. Suzuki, S. Takeuchi, and H. Yoshinaga, *Dislocation Dynamics and Plasticity*, en, Google-Books-ID: ZMLuCAAAQBAJ (Springer Science & Business Media, New York, Mar. 2013).

[6] S. M. Ott, “Cortical or Trabecular Bone: What’s the Difference?”, en, Am J Nephrol **47**, 373–375 (2018).

[7] T. M. Keaveny, E. F. Morgan, G. L. Niebur, and O. C. Yeh, “Biomechanics of Trabecular Bone”, en, Annu. Rev. Biomed. Eng. **3**, 307–333 (2001).

[8] R. Oftadeh, M. Perez-Viloria, J. C. Villa-Camacho, A. Vaziri, and A. Nazarian, “Biomechanics and Mechanobiology of Trabecular Bone: A Review”, en, Journal of Biomechanical Engineering **137**, 010802 (2015).

[9] J.-Y. Rho, L. Kuhn-Spearing, and P. Zioupos, “Mechanical properties and the hierarchical structure of bone”, en, Medical Engineering & Physics **20**, 92–102 (1998).

[10] J. J. B. Anderson and S. C. Garner, *Calcium and Phosphorus in Health and Disease*, en, Google-Books-ID: dpjj1ai4sX4C (CRC Press, Oct. 1995) Chap. 9.

[11] R. Hooke, *Micrographia, or Some Physiological Descriptions of Minute Bodies Made by Magnifying Glasses*, en (J. Martyn and J. Allestry, London, 1665).

[12] J. Zi, X. Yu, Y. Li, X. Hu, C. Xu, X. Wang, X. Liu, and R. Fu, “Coloration strategies in peacock feathers”, en, Proceedings of the National Academy of Sciences **100**, 12576–12578 (2003).

[13] S. Vignolini, P. J. Rudall, A. V. Rowland, A. Reed, E. Moyroud, R. B. Faden, J. J. Baumberg, B. J. Glover, and U. Steiner, “Pointillist structural color in *Pollia* fruit”, en, Proc. Natl. Acad. Sci. U.S.A. **109**, 15712–15715 (2012).

[14] S. Kinoshita, S. Yoshioka, and J. Miyazaki, “Physics of structural colors”, en, Rep. Prog. Phys. **71**, 076401 (2008).

[15] M. Deopura, C. K. Ullal, B. Temelkuran, and Y. Fink, "Dielectric omnidirectional visible reflector", en, Opt. Lett. **26**, 1197 (2001).

[16] J. D. Wilson and Z. D. Schwartz, "Multifocal flat lens with left-handed metamaterial", Applied Physics Letters **86**, 021113 (2005).

[17] Z. Liu, X. Zhang, Y. Mao, Y. Y. Zhu, Z. Yang, C. T. Chan, and P. Sheng, "Locally Resonant Sonic Materials", en, Science **289**, 1734–1736 (2000).

[18] F. Lemoult, N. Kaina, M. Fink, and G. Lerosey, "Soda Cans Metamaterial: A Subwavelength-Scaled Phononic Crystal", en, Crystals **6**, 82 (2016).

[19] E. Yablonovitch, "Inhibited Spontaneous Emission in Solid-State Physics and Electronics", en, Phys. Rev. Lett. **58**, 2059–2062 (1987).

[20] L. Lu, L. Fu, J. D. Joannopoulos, and M. Soljačić, "Weyl points and line nodes in gyroid photonic crystals", en, Nature Photon **7**, 294–299 (2013).

[21] R. Zengerle, "Light Propagation in Singly and Doubly Periodic Planar Waveguides", en, Journal of Modern Optics **34**, 1589–1617 (1987).

[22] S. John, "Strong localization of photons in certain disordered dielectric superlattices", en, Phys. Rev. Lett. **58**, 2486–2489 (1987).

[23] J. N. Winn, S. Fan, J. D. Joannopoulos, and E. P. Ippen, "Interband transitions in photonic crystals", en, Phys. Rev. B **59**, 1551–1554 (1999).

[24] M. Notomi, "Theory of light propagation in strongly modulated photonic crystals: Refractionlike behavior in the vicinity of the photonic band gap", en, Phys. Rev. B **62**, 10696–10705 (2000).

[25] B. Gralak, S. Enoch, and G. Tayeb, "Anomalous refractive properties of photonic crystals", en, J. Opt. Soc. Am. A **17**, 1012 (2000).

[26] K. Srinivasan and O. Painter, "Momentum space design of high-Q photonic crystal optical cavities", en, Opt. Express **10**, 670 (2002).

[27] F. D. M. Haldane and S. Raghu, "Possible Realization of Directional Optical Waveguides in Photonic Crystals with Broken Time-Reversal Symmetry", en, Phys. Rev. Lett. **100**, 013904 (2008).

[28] Y. Fink, J. N. Winn, S. Fan, C. Chen, J. Michel, J. D. Joannopoulos, and E. L. Thomas, "A Dielectric Omnidirectional Reflector", en, Science **282**, 1679–1682 (1998).

[29] C. Luo, S. G. Johnson, J. D. Joannopoulos, and J. B. Pendry, "All-angle negative refraction without negative effective index", en, Phys. Rev. B **65**, 201104 (2002).

[30] M. S. Kushwaha, P. Halevi, L. Dobrzynski, and B. Djafari-Rouhani, "Acoustic band structure of periodic elastic composites", en, Phys. Rev. Lett. **71**, 2022–2025 (1993).

[31] N. Laforge, V. Laude, F. Chollet, A. Khelif, M. Kadic, Y. Guo, and R. Fleury, "Observation of topological gravity-capillary waves in a water wave crystal", en, New J. Phys. **21**, 083031 (2019).

[32] V. Laude, *Phononic Crystals: Artificial Crystals for Sonic, Acoustic, and Elastic Waves*, en, Google-Books-ID: UFs8EAAAQBAJ (Walter de Gruyter GmbH & Co KG, Berlin, München, Boston, June 2020).

[33] T. Christensen, H. C. Po, J. D. Joannopoulos, and M. Soljačić, “Location and Topology of the Fundamental Gap in Photonic Crystals”, en, Phys. Rev. X **12**, 021066 (2022).

[34] Z. Jia, Y. Chen, H. Yang, and L. Wang, “Designing Phononic Crystals with Wide and Robust Band Gaps”, en, Phys. Rev. Applied **9**, 044021 (2018).

[35] O. McGee, H. Jiang, F. Qian, Z. Jia, L. Wang, H. Meng, D. Chronopoulos, Y. Chen, and L. Zuo, “3D printed architected hollow sphere foams with low-frequency phononic band gaps”, en, Additive Manufacturing **30**, 100842 (2019).

[36] J. O. Vasseur, P. A. Deymier, B. Chenni, B. Djafari-Rouhani, L. Dobrzynski, and D. Prevost, “Experimental and Theoretical Evidence for the Existence of Absolute Acoustic Band Gaps in Two-Dimensional Solid Phononic Crystals”, en, Phys. Rev. Lett. **86**, 3012–3015 (2001).

[37] F. Warmuth, M. Wormser, and C. Körner, “Single phase 3D phononic band gap material”, en, Sci Rep **7**, 3843 (2017).

[38] Y. F. Li, F. Meng, S. Zhou, M.-H. Lu, and X. Huang, “Broadband All-angle Negative Refraction by Optimized Phononic Crystals”, en, Sci Rep **7**, 7445 (2017).

[39] H. Liu, F. Ren, K. Liu, and X. Li, “Multiple Re-Entrant Star-Shaped Honeycomb with Double Negative Parameters and Bandgap Properties”, en, Physica Status Solidi (b) **259**, 2200277 (2022).

[40] A. A. Mokhtari, Y. Lu, and A. Srivastava, “On the emergence of negative effective density and modulus in 2-phase phononic crystals”, en, Journal of the Mechanics and Physics of Solids **126**, 256–271 (2019).

[41] B. Morvan, A. Tinel, A.-C. Hladky-Hennion, J. Vasseur, and B. Dubus, “Experimental demonstration of the negative refraction of a transverse elastic wave in a two-dimensional solid phononic crystal”, en, Appl. Phys. Lett. **96**, 101905 (2010).

[42] J. H. Page, “Focusing of ultrasonic waves by negative refraction in phononic crystals”, en, AIP Advances **6**, 121606 (2016).

[43] A. Sukhovich, L. Jing, and J. H. Page, “Negative refraction and focusing of ultrasound in two-dimensional phononic crystals”, en, Phys. Rev. B **77**, 014301 (2008).

[44] S.-D. Zhao and Y.-S. Wang, “Negative refraction and imaging of acoustic waves in a two-dimensional square chiral lattice structure”, en, Comptes Rendus Physique **17**, 533–542 (2016).

[45] H. Lamb, “On Group - Velocity”, en, Proc. Lond. Math. Soc. **s2-1**, 473–479 (1904).

[46] A. Schuster, *An Introduction to the Theory of Optics*, en (E. Arnold & Company, London, 1924).

[47] V. G. Veselago, “The electrodynamics of substances with simultaneously negative values of ϵ and μ”, en, Sov. Phys. Uspekhi **10**, 509–514 (1968).

[48] J. B. Pendry, “Negative Refraction Makes a Perfect Lens”, en, Physical Review Letters **85**, 3966–3969 (2000).

[49] J. Pendry, “Positively negative”, en, Nature **423**, 22–23 (2003).

[50] J. B. Pendry, A. J. Holden, W. J. Stewart, and I. Youngs, “Extremely Low Frequency Plasmons in Metallic Mesostructures”, en, Physical Review Letters **76**, 4773–4776 (1996).

[51] J. Pendry, A. Holden, D. Robbins, and W. Stewart, “Magnetism from conductors and enhanced nonlinear phenomena”, en, IEEE Trans. Microw. Theory Techn. **47**, 2075–2084 (1999).

[52] D. R. Smith, W. J. Padilla, D. C. Vier, S. C. Nemat-Nasser, and S. Schultz, “Composite Medium with Simultaneously Negative Permeability and Permittivity”, en, Phys. Rev. Lett. **84**, 4184–4187 (2000).

[53] R. A. Shelby, D. R. Smith, and S. Schultz, “Experimental Verification of a Negative Index of Refraction”, en, Science **292**, 77–79 (2001).

[54] D. R. Smith, J. B. Pendry, and M. C. K. Wiltshire, “Metamaterials and Negative Refractive Index”, en, Science **305**, 788–792 (2004).

[55] A. Sihvola, S. Tretyakov, and A. de Baas, “Metamaterials with extreme material parameters”, en, J. Commun. Technol. Electron. **52**, 986–990 (2007).

[56] M. J. Freire, R. Marques, and L. Jelinek, “Experimental demonstration of a $\mu = -1$ metamaterial lens for magnetic resonance imaging”, en, Applied Physics Letters **93**, 231108 (2008).

[57] X.-X. Liu, “Limitations and potentials of metamaterial lenses”, en, J. Nanophoton **5**, 053509 (2011).

[58] S. Palomba, S. Zhang, Y. Park, G. Bartal, X. Yin, and X. Zhang, “Optical negative refraction by four-wave mixing in thin metallic nanostructures”, en, Nature Mater **11**, 34–38 (2012).

[59] A. B. Khanikaev, S. Hossein Mousavi, W.-K. Tse, M. Kargarian, A. H. MacDonald, and G. Shvets, “Photonic topological insulators”, en, Nature Mater **12**, 233–239 (2013).

[60] N. Fang, D. Xi, J. Xu, M. Ambati, W. Srituravanich, C. Sun, and X. Zhang, “Ultrasonic metamaterials with negative modulus”, en, Nat. Mater. **5**, 452–456 (2006).

[61] C. T. Chan, J. Li, and K. H. Fung, “On extending the concept of double negativity to acoustic waves”, en, J. Zhejiang Univ. - Sci. A **7**, 24–28 (2006).

[62] N. Kaina, F. Lemoult, M. Fink, and G. Lerosey, “Negative refractive index and acoustic superlens from multiple scattering in single negative metamaterials”, en, Nature **525**, 77–81 (2015).

[63] Y. Lai, Y. Wu, P. Sheng, and Z.-Q. Zhang, “Hybrid elastic solids”, en, Nature Mater **10**, 620–624 (2011).

[64] R. S. Lakes, T. Lee, A. Bersie, and Y. C. Wang, “Extreme damping in composite materials with negative-stiffness inclusions”, en, Nature **410**, 565–567 (2001).

[65] X. Lin, E. Li, Z. He, Y. Wu, and Q. Li, “Design of single-phase chiral metamaterials for broadband double negativity via shape optimization”, en, Applied Mathematical Modelling **91**, 335–357 (2021).

[66] R. S. Lakes, “Extreme Damping in Composite Materials with a Negative Stiffness Phase”, en, Phys. Rev. Lett. **86**, 2897–2900 (2001).

[67] H. Liu, Q. Zhang, K. Zhang, G. Hu, and H. Duan, “Designing 3D Digital Metamaterial for Elastic Waves: From Elastic Wave Polarizer to Vibration Control”, en, Adv. Sci. **6**, 1900401 (2019).

[68] X. N. Liu, G. K. Hu, G. L. Huang, and C. T. Sun, “An elastic metamaterial with simultaneously negative mass density and bulk modulus”, en, Appl. Phys. Lett. **98**, 251907 (2011).

[69] J. Mei, G. Ma, M. Yang, Z. Yang, W. Wen, and P. Sheng, “Dark acoustic metamaterials as super absorbers for low-frequency sound”, en, Nat Commun **3**, 756 (2012).

[70] J. H. Oh, Y. E. Kwon, H. J. Lee, and Y. Y. Kim, “Elastic metamaterials for independent realization of negativity in density and stiffness”, en, Sci Rep **6**, 23630 (2016).

[71] M. Chen, W. Xu, Y. Liu, K. Yan, H. Jiang, and Y. Wang, “Band gap and double-negative properties of a star-structured sonic metamaterial”, en, Applied Acoustics **139**, 235–242 (2018).

[72] J. H. Oh, H. M. Seung, and Y. Y. Kim, “Doubly negative isotropic elastic metamaterial for sub-wavelength focusing: Design and realization”, en, Journal of Sound and Vibration **410**, 169–186 (2017).

[73] S. Sang and Z. Wang, “A design of elastic metamaterials with multi-negative pass bands”, en, Acta Mech **229**, 2647–2655 (2018).

[74] Y. Wu, Y. Lai, and Z.-Q. Zhang, “Elastic Metamaterials with Simultaneously Negative Effective Shear Modulus and Mass Density”, en, Phys. Rev. Lett. **107**, 105506 (2011).

[75] Y.-F. Wang, Y.-S. Wang, and C. Zhang, “Two-dimensional locally resonant elastic metamaterials with chiral comb-like interlayers: Bandgap and simultaneously double negative properties”, en, J. Acoust. Soc. Am. **139**, 3311–3319 (2016).

[76] J.-E. Wu, X. Wang, B. Tang, Z. He, K. Deng, and H. Zhao, “Elastic metamaterial with simultaneously negative refraction for longitudinal and transverse waves”, en, AIP Advances **7**, 105309 (2017).

[77] W. Wang, B. Bonello, B. Djafari-Rouhani, Y. Pennec, and J. Zhao, “Double-Negative Pillared Elastic Metamaterial”, en, Phys. Rev. Applied **10**, 064011 (2018).

[78] Y.-F. Wang, S.-Y. Zhang, Y.-S. Wang, and V. Laude, “Hybridization of resonant modes and Bloch waves in acoustoelastic phononic crystals”, en, Phys. Rev. B **102**, 144303 (2020).

[79] H. Wang, S. Cheng, C. Wang, Y. Sun, and Y. Xin, “Tunable band gaps and double-negative properties of innovative acoustic metamaterials”, en, Appl. Phys. A **127**, 495 (2021).

[80]Y. Xin, K. Zhang, X. Du, Q. Ding, Q. Yan, Y. Sun, S. Cheng, and L. Wang, “Bandgap and Wave Propagation Properties of 2D Curved and Chiral Hybrid Star-Shaped Metamaterials”, en, Physica Status Solidi (b), 2200333 (2022).

[81]X. Chen, L. Cai, and J. Wen, “Extreme mechanical metamaterials with independently adjustable elastic modulus and mass density”, en, Appl. Phys. Express **15**, 047001 (2022).

[82]Z. Yang, J. Mei, M. Yang, N. H. Chan, and P. Sheng, “Membrane-Type Acoustic Metamaterial with Negative Dynamic Mass”, en, Physical Review Letters **101**, 204301 (2008).

[83]M. Yang, G. Ma, Z. Yang, and P. Sheng, “Subwavelength perfect acoustic absorption in membrane-type metamaterials: a geometric perspective”, en, EPJ Applied Metamaterials **2**, edited by A. Christos and M. Alessio, 10 (2015).

[84]R. Zhu, X. N. Liu, G. K. Hu, C. T. Sun, and G. L. Huang, “Negative refraction of elastic waves at the deep-subwavelength scale in a single-phase metamaterial”, en, Nat Commun **5**, 5510 (2014).

[85]H. Zhang, Y. Chen, X. Liu, and G. Hu, “An asymmetric elastic metamaterial model for elastic wave cloaking”, en, Journal of the Mechanics and Physics of Solids **135**, 103796 (2020).

[86]D. Yu, Y. Liu, H. Zhao, G. Wang, and J. Qiu, “Flexural vibration band gaps in Euler-Bernoulli beams with locally resonant structures with two degrees of freedom”, en, Physical Review B **73**, 5 (2006).

[87]X. Zhou, X. Liu, and G. Hu, “Elastic metamaterials with local resonances: an overview”, en, Theor. Appl. Mech. Lett. **2**, 041001 (2012).

[88]R. V. Craster and S. Guenneau, *Acoustic Metamaterials: Negative Refraction, Imaging, Lensing and Cloaking*, en, Google-Books-ID: uv4lQ0tQJtkC (Springer Science & Business Media, New York, Dec. 2012).

[89]W. Wang, B. Bonello, B. Djafari-Rouhani, Y. Pennec, and J. Zhao, “Elastic stubbed metamaterial plate with torsional resonances”, en, Ultrasonics **106**, 106142 (2020).

[90]J. Christensen and F. J. G. de Abajo, “Anisotropic Metamaterials for Full Control of Acoustic Waves”, en, Phys. Rev. Lett. **108**, 124301 (2012).

[91]S. Yves, R. Fleury, T. Berthelot, M. Fink, F. Lemoult, and G. Lerosey, “Crystalline metamaterials for topological properties at subwavelength scales”, en, Nat Commun **8**, 16023 (2017).

[92]S. A. Cummer, J. Christensen, and A. Alù, “Controlling sound with acoustic metamaterials”, en, Nat Rev Mater **1**, 16001 (2016).

[93]H.-W. Dong, S.-D. Zhao, P. Wei, L. Cheng, Y.-S. Wang, and C. Zhang, “Systematic design and realization of double-negative acoustic metamaterials by topology optimization”, en, Acta Materialia **172**, 102–120 (2019).

[94]H.-W. Dong, S.-D. Zhao, Y.-S. Wang, and C. Zhang, “Topology optimization of anisotropic elastic metamaterial with broadband double-negative index”, en, Journal of the Mechanics and Physics of Solids **105**, 54–80 (2017).

[95] H. H. Huang and C. T. Sun, “Anomalous wave propagation in a one-dimensional acoustic metamaterial having simultaneously negative mass density and Young’s modulus”, en, J. Acoust. Soc. Am. **132**, 2887–2895 (2012).

[96] H. Huang and C. Sun, “Theoretical investigation of the behavior of an acoustic metamaterial with extreme Young’s modulus”, en, J. Mech. Phys. Solids. **59**, 2070–2081 (2011).

[97] M. Silveirinha and N. Engheta, “Tunneling of Electromagnetic Energy through Subwavelength Channels and Bends using ϵ -Near-Zero Materials”, en, Phys. Rev. Lett. **97**, 157403 (2006).

[98] B. Edwards, A. Alù, M. E. Young, M. Silveirinha, and N. Engheta, “Experimental Verification of Epsilon-Near-Zero Metamaterial Coupling and Energy Squeezing Using a Microwave Waveguide”, en, Phys. Rev. Lett. **100**, 033903 (2008).

[99] N. Engheta, “Pursuing Near-Zero Response”, en, Science **340**, 286–287 (2013).

[100] R. Fleury and A. Alù, “Extraordinary Sound Transmission through Density-Near-Zero Ultranarrow Channels”, en, Phys. Rev. Lett. **111**, 055501 (2013).

[101] A. Alù and N. Engheta, “Achieving transparency with plasmonic and metamaterial coatings”, en, Phys. Rev. E **72**, 016623 (2005).

[102] G. W. Milton, M. Briane, and J. R. Willis, “On cloaking for elasticity and physical equations with a transformation invariant form”, en, New J. Phys. **8**, 248–248 (2006).

[103] U. Leonhardt, “Optical Conformal Mapping”, en, Science **312**, 1777–1780 (2006).

[104] J. B. Pendry, D. Schurig, and D. R. Smith, “Controlling Electromagnetic Fields”, en, Science **312**, 1780–1782 (2006).

[105] D. Schurig, J. J. Mock, B. J. Justice, S. A. Cummer, J. B. Pendry, A. F. Starr, and D. R. Smith, “Metamaterial Electromagnetic Cloak at Microwave Frequencies”, en, Science **314**, 977–980 (2006).

[106] M. Farhat, S. Guenneau, and S. Enoch, “Ultrabroadband Elastic Cloaking in Thin Plates”, en, Phys. Rev. Lett. **103**, 024301 (2009).

[107] R. Liu, C. Ji, J. J. Mock, J. Y. Chin, T. J. Cui, and D. R. Smith, “Broadband Ground-Plane Cloak”, en, Science **323**, 366–369 (2009).

[108] P.-Y. Chen, M. Farhat, S. Guenneau, S. Enoch, and A. Alù, “Acoustic scattering cancellation via ultrathin pseudo-surface”, en, Applied Physics Letters **99**, 191913 (2011).

[109] S. Brûlé, E. H. Javelaud, S. Enoch, and S. Guenneau, “Experiments on Seismic Metamaterials: Molding Surface Waves”, en, Phys. Rev. Lett. **112**, 133901 (2014).

[110] A. Colombi, P. Roux, S. Guenneau, P. Gueguen, and R. V. Craster, “Forests as a natural seismic metamaterial: Rayleigh wave bandgaps induced by local resonances”, en, Sci Rep **6**, 19238 (2016).

[111] S. Brûlé, B. Ungureanu, Y. Achaoui, A. Diatta, R. Aznavourian, T. Antonakakis, R. Craster, S. Enoch, and S. Guenneau, “Metamaterial-like transformed urbanism”, en, Innov. Infrastruct. Solut. **2**, 20 (2017).

[112] J. B. Pendry, “Time Reversal and Negative Refraction”, en, Science **322**, 71–73 (2008).

[113] D. Forcella, C. Prada, and R. Carminati, “Causality, Nonlocality, and Negative Refraction”, en, Physical Review Letters **118**, 134301 (2017).

[114] F. Monticone and A. Alu, “Do cloaked objects really scatter less?”, Physical Review X **3**, 041005 (2013).

[115] F. Monticone and A. Alu, “Invisibility exposed: physical bounds on passive cloaking”, Optica **3**, 718–724 (2016).

[116] S. H. Lee and O. B. Wright, “Origin of negative density and modulus in acoustic metamaterials”, en, Phys. Rev. B **93**, 024302 (2016).

[117] Z. Liang and J. Li, “Extreme Acoustic Metamaterial by Coiling Up Space”, en, Phys. Rev. Lett. **108**, 114301 (2012).

[118] Y. Xie, B.-I. Popa, L. Zigoneanu, and S. A. Cummer, “Measurement of a Broadband Negative Index with Space-Coiling Acoustic Metamaterials”, en, Phys. Rev. Lett. **110**, 175501 (2013).

[119] B. Liu, B. Ren, J. Zhao, X. Xu, Y. Feng, W. Zhao, and Y. Jiang, “Experimental realization of all-angle negative refraction in acoustic gradient metasurface”, en, Applied Physics Letters **111**, 221602 (2017).

[120] C. Liu, B. Xia, and D. Yu, “The spiral-labyrinthine acoustic metamaterial by coiling up space”, en, Physics Letters A **381**, 3112–3118 (2017).

[121] Y. Liu, W. Xu, M. Chen, T. Yang, K. Wang, X. Huang, H. Jiang, and Y. Wang, “Three-dimensional fractal structure with double negative and density-near-zero properties on a subwavelength scale”, en, Materials & Design **188**, 108470 (2020).

[122] C. Prada, O. Balogun, and T. W. Murray, “Laser-based ultrasonic generation and detection of zero-group velocity Lamb waves in thin plates”, en, Applied Physics Letters **87**, 194109 (2005).

[123] F. D. Philippe, T. W. Murray, and C. Prada, “Focusing on Plates: Controlling Guided Waves using Negative Refraction”, en, Sci Rep **5**, 11112 (2015).

[124] Q. Xie, S. Mezil, P. H. Otsuka, M. Tomoda, J. Laurent, O. Matsuda, Z. Shen, and O. B. Wright, “Imaging gigahertz zero-group-velocity Lamb waves”, en, Nat Commun **10**, 2228 (2019).

[125] E. Glushkov and N. Glushkova, “Multiple zero-group velocity resonances in elastic layered structures”, en, Journal of Sound and Vibration **500**, 116023 (2021).

[126] D. A. Kiefer, S. Mezil, and C. Prada, *Beating resonance patterns and orthogonal wave propagation due to zero-group-velocity guided elastic waves*, en, arXiv:2307.14259 [cond-mat, physics:physics], July 2023.

[127] J. Kishine, A. S. Ovchinnikov, and A. A. Tereshchenko, “Chirality-Induced Phonon Dispersion in a Noncentrosymmetric Micropolar Crystal”, en, Physical Review Letters **125**, 245302 (2020).

[128] J. A. Iglesias Martínez, M. F. Groß, Y. Chen, T. Frenzel, V. Laude, M. Kadic, and M. Wegener, “Experimental observation of roton-like dispersion relations in metamaterials”, en, Sci. Adv. **7**, eabm2189 (2021).

[129] Y. Chen, M. Kadic, and M. Wegener, “Roton-like acoustical dispersion relations in 3D metamaterials”, en, Nat Commun **12**, 3278 (2021).

[130] K. Wang, Y. Chen, M. Kadic, C. Wang, and M. Wegener, “Nonlocal interaction engineering of 2D roton-like dispersion relations in acoustic and mechanical metamaterials”, en, Commun Mater **3**, 35 (2022).

[131] Z. Zhou, S. Huang, D. Li, J. Zhu, and Y. Li, “Broadband impedance modulation via non-local acoustic metamaterials”, en, National Science Review **9**, nwab171 (2022).

[132] Z. Zhu, Z. Gao, G.-G. Liu, Y. Ge, Y. Wang, X. Xi, B. Yan, F. Chen, P. P. Shum, H.-x. Sun, and Y. Yang, “Observation of multiple rotons and multidirectional roton-like dispersion relations in acoustic metamaterials”, en, New J. Phys. **24**, 123019 (2022).

[133] G. Chaplain, I. Hooper, A. Hibbins, and T. Starkey, “Reconfigurable Elastic Metamaterials: Engineering Dispersion with Beyond Nearest Neighbors”, en, Phys. Rev. Applied **19**, 044061 (2023).

[134] Y. Chen, J. L. G. Schneider, M. F. Groß, K. Wang, S. Kalt, P. Scott, M. Kadic, and M. Wegener, “Observation of Chirality-Induced Roton-Like Dispersion in a 3D Micropolar Elastic Metamaterial”, en, Adv Funct Materials, 2302699 (2023).

[135] K. Wang, Y. Chen, M. Kadic, C. Wang, and M. Wegener, “Cubic-symmetry acoustic metamaterials with roton-like dispersion relations”, en, Acta Mech. Sin. **39**, 723020 (2023).

[136] L. Landau, “Theory of the Superfluidity of Helium II”, en, Physical Review **60**, Publisher: American Physical Society, 356–358 (1941).

[137] R. P. Feynman and M. Cohen, “Energy Spectrum of the Excitations in Liquid Helium”, en, Physical Review **102**, 1189–1204 (1956).

[138] P. Nozières, “Is the Roton in Superfluid ^{4} He the Ghost of a Bragg Spot?”, en, Journal of Low Temperature Physics **137**, 45–67 (2004).

[139] P. Nozières, “More about Rotons in Superfluid Helium 4”, en, J Low Temp Phys **142**, 91–99 (2006).

[140] H. Godfrin, K. Beauvois, A. Sultan, E. Krotscheck, J. Dawidowski, B. Fåk, and J. Ollivier, “Dispersion relation of Landau elementary excitations and thermodynamic properties of superfluid He 4”, en, Phys. Rev. B **103**, 104516 (2021).

[141] A. Bossart, D. M. J. Dykstra, J. van der Laan, and C. Coulais, “Oligomodal metamaterials with multifunctional mechanics”, en, Proc. Natl. Acad. Sci. U.S.A. **118**, e2018610118 (2021).

[142] A. Bossart and R. Fleury, “Extreme Spatial Dispersion in Nonlocally Resonant Elastic Metamaterials”, en, Phys. Rev. Lett. **130**, 207201 (2023).

[143] W.-J. Chen, B. Hou, Z.-Q. Zhang, J. B. Pendry, and C. T. Chan, “Metamaterials with index ellipsoids at arbitrary k-points”, en, Nat Commun **9**, 2086 (2018).

[144] P. A. Belov, R. Marqués, S. I. Maslovski, I. S. Nefedov, M. Silveirinha, C. R. Simovski, and S. A. Tretyakov, “Strong spatial dispersion in wire media in the very large wavelength limit”, en, Physical Review B **67**, 113103 (2003).

[145] H. Latioui and M. G. Silveirinha, “Light tunneling anomaly in interlaced metallic wire meshes”, en, Phys. Rev. B **96**, 195132 (2017).

[146] D. Sakhno, E. Koreshin, and P. A. Belov, “Longitudinal electromagnetic waves with extremely short wavelength”, en, Phys. Rev. B **104**, L100304 (2021).

[147] E. A. Koreshin and M. V. Rybin, “Interlaced wire medium with quasicrystal lattice”, en, Phys. Rev. B **105**, 024307 (2022).

[148] D. Sakhno, E. Koreshin, and P. A. Belov, “Controlling the dispersion of longitudinal waves via the affine deformation of the interlaced wire medium”, en, Photonics and Nanostructures - Fundamentals and Applications **55**, 101150 (2023).

[149] J. Shim, S. Shan, A. Košmrlj, S. H. Kang, E. R. Chen, J. C. Weaver, and K. Bertoldi, “Harnessing instabilities for design of soft reconfigurable auxetic/chiral materials”, en, Soft Matter **9**, 8198 (2013).

[150] M. Stern, V. Jayaram, and A. Murugan, “Shaping the topology of folding pathways in mechanical systems”, en, Nat Commun **9**, 4303 (2018).

[151] M. Kadic, G. W. Milton, M. van Hecke, and M. Wegener, “3D metamaterials”, en, Nat Rev Phys **1**, 198–210 (2019).

[152] M. Fruchart, Y. Zhou, and V. Vitelli, “Dualities and non-Abelian mechanics”, en, Nature **577**, 636–640 (2020).

[153] G. W. Milton, “Complete characterization of the macroscopic deformations of periodic unimode metamaterials of rigid bars and pivots”, en, Journal of the Mechanics and Physics of Solids **61**, 1543–1560 (2013).

[154] T. Bückmann, R. Schittny, M. Thiel, M. Kadic, G. W. Milton, and M. Wegener, “On three-dimensional dilational elastic metamaterials”, en, New J. Phys. **16**, 033032 (2014).

[155] B. Florijn, C. Coulais, and M. van Hecke, “Programmable Mechanical Metamaterials”, en, Phys. Rev. Lett. **113**, 175503 (2014).

[156] C. Coulais, J. T. B. Overvelde, L. A. Lubbers, K. Bertoldi, and M. van Hecke, “Discontinuous Buckling of Wide Beams and Metabeams”, en, Phys. Rev. Lett. **115**, 044301 (2015).

[157] J. Christensen, M. Kadic, O. Kraft, and M. Wegener, “Vibrant times for mechanical metamaterials”, en, MRS Commun. **5**, 453–462 (2015).

[158] J. T. B. Overvelde, J. C. Weaver, C. Hoberman, and K. Bertoldi, “Rational design of reconfigurable prismatic architected materials”, en, Nature **541**, 347–352 (2017).

[159] T. Frenzel, M. Kadic, and M. Wegener, “Three-dimensional mechanical metamaterials with a twist”, en, Science **358**, 1072–1074 (2017).

[160] K. Bertoldi, V. Vitelli, J. Christensen, and M. van Hecke, “Flexible mechanical metamaterials”, en, Nat Rev Mater **2**, 17066 (2017).

[161] R. Lakes, “Foam Structures with a Negative Poisson’s Ratio”, en, Science **235**, 1038–1040 (1987).

[162] K. E. Evans, M. A. Nkansah, I. J. Hutchinson, and S. C. Rogers, “Molecular network design”, en, Nature **353**, 124–124 (1991).

[163] J. N. Grima and K. E. Evans, “Auxetic behavior from rotating squares”, en, Journal of Materials Science Letters **19**, 1563–1565 (2000).

[164] K. Bertoldi, P. M. Reis, S. Willshaw, and T. Mullin, “Negative Poisson’s Ratio Behavior Induced by an Elastic Instability”, en, Adv. Mater. **22**, 361–366 (2010).

[165] H. M. A. Kolken, S. Janbaz, S. M. A. Leeflang, K. Lietaert, H. H. Weinans, and A. A. Zadpoor, “Rationally designed meta-implants: a combination of auxetic and conventional metabiomaterials”, en, Mater. Horiz. **5**, 28–35 (2018).

[166] A. P. Giddy, M. T. Dove, G. S. Pawley, and V. Heine, “The determination of rigid-unit modes as potential soft modes for displacive phase transitions in framework crystal structures”, en, Acta Crystallogr. A **49**, 697–703 (1993).

[167] K. D. Hammonds, M. T. Dove, A. P. Giddy, V. Heine, and B. Winkler, “Rigid-unit phonon modes and structural phase transitions in framework silicates”, en, American Mineralogist **81**, 1057–1079 (1996).

[168] M. T. Dove, “Theory of displacive phase transitions in minerals”, en, American Mineralogist **82**, 213–244 (1997).

[169] G. W. Milton and A. V. Cherkaev, “Which Elasticity Tensors are Realizable?”, en, J. Eng. Mater. Technol. **117**, 483–493 (1995).

[170] G. W. Milton, *The theory of composites*, en (SIAM, Philadelphia, PA, 2022).

[171] G. W. Milton and J. R. Willis, “On modifications of Newton’s second law and linear continuum elastodynamics”, en, Proc. R. Soc. A. **463**, 855–880 (2007).

[172] A. Martin, M. Kadic, R. Schittny, T. Bückmann, and M. Wegener, “Phonon band structures of three-dimensional pentamode metamaterials”, en, Phys. Rev. B **86**, 155116 (2012).

[173] M. Kadic, T. Bückmann, N. Stenger, M. Thiel, and M. Wegener, “On the practicability of pentamode mechanical metamaterials”, en, Applied Physics Letters **100**, 191901 (2012).

[174] E. M. P. Cosserat and F. Cosserat, *Théorie des corps déformables*, fr (A. Hermann et fils, Paris, 1909).

[175] D. Bigoni and W. J. Drugan, “Analytical Derivationof Cosserat Moduli via Homogenization of Heterogeneous ElasticMaterials”, en, Journal of Applied Mechanics **74**, 741–753 (2007).

[176] Z. Rueger and R. S. Lakes, “Strong Cosserat Elasticity in a Transversely Isotropic Polymer Lattice”, en, Phys. Rev. Lett. **120**, 065501 (2018).

[177] A. C. Eringen, “Linear Theory of Micropolar Elasticity”, en, Journal of Mathematics and Mechanics **15**, Publisher: Indiana University Mathematics Department, 909–923 (1966).

[178]V. A. Eremeyev, L. P. Lebedev, and H. Altenbach, *Foundations of Micropolar Mechanics*, en, Google-Books-ID: NZAZS8bBg7MC (Springer Science & Business Media, New York, July 2012).

[179]Y. Chen, T. Frenzel, S. Guenneau, M. Kadic, and M. Wegener, “Mapping acoustical activity in 3D chiral mechanical metamaterials onto micropolar continuum elasticity”, en, Journal of the Mechanics and Physics of Solids **137**, 103877 (2020).

[180]J. Shim, C. Perdigou, E. R. Chen, K. Bertoldi, and P. M. Reis, “Buckling-induced encapsulation of structured elastic shells under pressure”, en, Proc. Natl. Acad. Sci. U.S.A. **109**, 5978–5983 (2012).

[181]Y. Cho, J.-H. Shin, A. Costa, T. A. Kim, V. Kunin, J. Li, S. Y. Lee, S. Yang, H. N. Han, I.-S. Choi, and D. J. Srolovitz, “Engineering the shape and structure of materials by fractal cut”, en, Proc. Natl. Acad. Sci. U.S.A. **111**, 17390–17395 (2014).

[182]A. Sydney Gladman, E. A. Matsumoto, R. G. Nuzzo, L. Mahadevan, and J. A. Lewis, “Biomimetic 4D printing”, en, Nature Mater **15**, 413–418 (2016).

[183]R. M. Neville, F. Scarpa, and A. Pirrera, “Shape morphing Kirigami mechanical metamaterials”, en, Sci Rep **6**, 31067 (2016).

[184]G. P. T. Choi, L. H. Dudte, and L. Mahadevan, “Programming shape using kirigami tessellations”, en, Nat. Mater. **18**, 999–1004 (2019).

[185]L. A. Shaw, F. Sun, C. M. Portela, R. I. Barranco, J. R. Greer, and J. B. Hopkins, “Computationally efficient design of directionally compliant metamaterials”, en, Nat Commun **10**, 291 (2019).

[186]E. Siéfert, E. Reyssat, J. Bico, and B. Roman, “Bio-inspired pneumatic shape-morphing elastomers”, en, Nature Mater **18**, 24–28 (2019).

[187]Y. Zhu, M. Birla, K. R. Oldham, and E. T. Filipov, “Elastically and Plastically Foldable Electrothermal Micro-Origami for Controllable and Rapid Shape Morphing”, en, Adv. Funct. Mater. **30**, 2003741 (2020).

[188]F. Wenz, I. Schmidt, A. Leichner, T. Lichti, S. Baumann, H. Andrae, and C. Eberl, “Designing Shape Morphing Behavior through Local Programming of Mechanical Metamaterials”, en, Advanced Materials **33**, 2008617 (2021).

[189]C. Coulais, E. Teomy, K. de Reus, Y. Shokef, and M. van Hecke, “Combinatorial design of textured mechanical metamaterials”, en, Nature **535**, 529–532 (2016).

[190]P. Dieleman, N. Vasmel, S. Waitukaitis, and M. van Hecke, “Jigsaw puzzle design of pluripotent origami”, en, Nat. Phys. **16**, 63–68 (2020).

[191]A. S. Meeussen, E. C. Oğuz, Y. Shokef, and M. v. Hecke, “Topological defects produce exotic mechanics in complex metamaterials”, en, Nat. Phys. **16**, 307–311 (2020).

[192]B. Pisanty, E. C. Oğuz, C. Nisoli, and Y. Shokef, “Putting a spin on metamaterials: Mechanical incompatibility as magnetic frustration”, en, SciPost Phys. **10**, 136 (2021).

[193] R. van Mastrigt, M. Dijkstra, M. van Hecke, and C. Coulais, “Machine Learning of Implicit Combinatorial Rules in Mechanical Metamaterials”, en, Phys. Rev. Lett. **129**, 198003 (2022).

[194] D. M. J. Dykstra and C. Coulais, *Inverse design of multishape metamaterials*, en, arXiv:2304.12124 [cond-mat, physics:physics], Apr. 2023.

[195] R. Oftadeh, B. Haghpanah, D. Vella, A. Boudaoud, and A. Vaziri, “Optimal Fractal-Like Hierarchical Honeycombs”, en, Phys. Rev. Lett. **113**, 104301 (2014).

[196] D. Mousanezhad, S. Babaee, H. Ebrahimi, R. Ghosh, A. S. Hamouda, K. Bertoldi, and A. Vaziri, “Hierarchical honeycomb auxetic metamaterials”, en, Sci Rep **5**, 18306 (2015).

[197] X. Li, R. Fan, Z. Fan, and Y. Lu, “Programmable mechanical metamaterials based on hierarchical rotating structures”, en, International Journal of Solids and Structures **216**, 145–155 (2021).

[198] K. K. Dudek, R. Gatt, M. R. Dudek, and J. N. Grima, “Controllable Hierarchical Mechanical Metamaterials Guided by the Hinge Design”, en, Materials **14**, 758 (2021).

[199] C. L. Kane and T. C. Lubensky, “Topological boundary modes in isostatic lattices”, en, Nature Phys **10**, 39–45 (2014).

[200] T. C. Lubensky, C. L. Kane, X. Mao, A. Souslov, and K. Sun, “Phonons and elasticity in critically coordinated lattices”, en, Rep. Prog. Phys. **78**, 073901 (2015).

[201] J. Paulose, B. G.-g. Chen, and V. Vitelli, “Topological modes bound to dislocations in mechanical metamaterials”, en, Nature Phys **11**, 153–156 (2015).

[202] D. Z. Rocklin, B. G.-g. Chen, M. Falk, V. Vitelli, and T. C. Lubensky, “Mechanical Weyl Modes in Topological Maxwell Lattices”, en, Phys. Rev. Lett. **116**, 135503 (2016).

[203] X. Ni, M. Weiner, A. Alù, and A. B. Khanikaev, “Observation of higher-order topological acoustic states protected by generalized chiral symmetry”, en, Nature Mater **18**, 113–120 (2019).

[204] A. S. Meeussen, J. Paulose, and V. Vitelli, “Geared Topological Metamaterials with Tunable Mechanical Stability”, en, Physical Review X **6**, 041029 (2016).

[205] A. Bossart and R. Fleury, “Non-Hermitian time evolution: From static to parametric instability”, en, Phys. Rev. A **104**, 042225 (2021).

[206] J. Maxwell, “London, edinburgh dublin philos. mag”, J. sci **27**, 294–299 (1864).

[207] C. Calladine, “Buckminster fuller’s “tensegrity” structures and clerk maxwell’s rules for the construction of stiff frames”, International Journal of Solids and Structures **14**, 161–172 (1978).

[208] J. D. Bernal and R. H. Fowler, “A Theory of Water and Ionic Solution, with Particular Reference to Hydrogen and Hydroxyl Ions”, en, The Journal of Chemical Physics **1**, 515–548 (1933).

[209] E. H. Lieb, “Residual Entropy of Square Ice”, en, Phys. Rev. **162**, 162–172 (1967).

[210] R. J. Baxter, “Partition function of the eight-vertex lattice model”, en, Annals of Physics **70**, Publisher: Elsevier, 193–228 (1972).

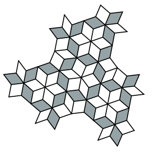

[211] S. Guest, “On the determinacy of repetitive structures”, en, Journal of the Mechanics and Physics of Solids **51**, 383–391 (2003).

[212] D. B. Liarte, O. Stenull, and T. C. Lubensky, “Multifunctional twisted kagome lattices: Tuning by pruning mechanical metamaterials”, en, Phys. Rev. E **101**, 063001 (2020).

[213] M. F. Ashby, T. Evans, N. A. Fleck, J. W. Hutchinson, H. N. G. Wadley, and L. J. Gibson, *Metal Foams: A Design Guide*, en, Google-Books-ID: C0daIBo6LjgC (Elsevier, July 2000).

[214] S. D. Papka and S. Kyriakides, “In-plane crushing of a polycarbonate honeycomb”, en, International Journal of Solids and Structures **35**, 239–267 (1998).

[215] S. Gaitanaros and S. Kyriakides, “On the effect of relative density on the crushing and energy absorption of open-cell foams under impact”, en, International Journal of Impact Engineering **82**, 3–13 (2015).

[216] D. Shechtman, I. Blech, D. Gratias, and J. W. Cahn, “Metallic Phase with Long-Range Orientational Order and No Translational Symmetry”, en, Phys. Rev. Lett. **53**, 1951–1953 (1984).

[217] D. Levine and P. J. Steinhardt, “Quasicrystals. I. Definition and structure”, en, Phys. Rev. B **34**, 596–616 (1986).

[218] W. Steurer and D. Sutter-Widmer, “Photonic and phononic quasicrystals”, en, J. Phys. D: Appl. Phys. **40**, R229–R247 (2007).

[219] L. Liu, G. P. T. Choi, and L. Mahadevan, “Quasicrystal kirigami”, en, Phys. Rev. Research **4**, 033114 (2022).

[220] L. Jansen and M. Boon, *Theory of Finite Groups: Applications in Physics : Symmetry Groups of Quantum Mechanical Systems*, en (North-Holland, Amsterdam, 1967).

[221] L. Fang and M. J. Leamy, “Negative Refraction in Mechanical Rotator Lattices”, en, Phys. Rev. Applied **18**, 064058 (2022).

[222] C. Coulais, C. Kettenis, and M. van Hecke, “A characteristic length scale causes anomalous size effects and boundary programmability in mechanical metamaterials”, en, Nature Phys **14**, 40–44 (2018).

[223] D. M. J. Dykstra, J. Busink, B. Ennis, and C. Coulais, “Viscoelastic Snapping Metamaterials”, en, Journal of Applied Mechanics **86**, 111012 (2019).

[224] J. A. Jackson, M. C. Messner, N. A. Dudukovic, W. L. Smith, L. Bekker, B. Moran, A. M. Golobic, A. J. Pascall, E. B. Duoss, K. J. Loh, and C. M. Spadaccini, “Field responsive mechanical metamaterials”, en, Sci. Adv. **4**, eaau6419 (2018).

[225] C. Song, B. Zou, Z. Cui, Z. Liang, and J. Ju, “Thermomechanically Triggered Reversible Multi-Transformability of a Single Material System by Energy Swapping and Shape Memory Effects”, en, Adv Funct Materials **31**, 2101395 (2021).

[226] R. Galea, K. K. Dudek, P.-S. Farrugia, L. Zammit Mangion, J. N. Grima, and R. Gatt, “Reconfigurable magneto-mechanical metamaterials guided by magnetic fields”, en, Composite Structures **280**, 114921 (2022).

[227] T. Chen, M. Pauly, and P. M. Reis, “A reprogrammable mechanical metamaterial with stable memory”, en, Nature **589**, 386–390 (2021).

[228] R. S. Lakes, *Viscoelastic Materials*, en, Google-Books-ID: BH6f2hWWBkAC (Cambridge University Press, Cambridge, Apr. 2009).

[229] S. Janbaz, K. Narooei, T. van Manen, and A. A. Zadpoor, “Strain rate–dependent mechanical metamaterials”, en, Sci. Adv. **6**, eaba0616 (2020).

[230] O. Malyuskin and V. Fusco, “Near Field Focusing Using Phase Conjugating Impedance Loaded Wire Lens”, en, IEEE Trans. Antennas Propagat. **58**, 2884–2893 (2010).

[231] S. Hrabar, I. Krois, I. Bonic, and A. Kiricenko, “Negative capacitor paves the way to ultra-broadband metamaterials”, en, Appl. Phys. Lett. **99**, 254103 (2011).

[232] R. Fleury, D. L. Sounas, and A. Alù, “Negative Refraction and Planar Focusing Based on Parity-Time Symmetric Metasurfaces”, en, Phys. Rev. Lett. **113**, 023903 (2014).

[233] B.-I. Popa, L. Zigoneanu, and S. A. Cummer, “Tunable active acoustic metamaterials”, en, Phys. Rev. B **88**, 024303 (2013).

[234] C. M. Bender and S. Boettcher, “Real Spectra in Non-Hermitian Hamiltonians Having P T Symmetry”, en, Phys. Rev. Lett. **80**, 5243–5246 (1998).

[235] S. Longhi, “Bloch Oscillations in Complex Crystals with P T Symmetry”, en, Phys. Rev. Lett. **103**, 123601 (2009).

[236] C. E. Rüter, K. G. Makris, R. El-Ganainy, D. N. Christodoulides, M. Segev, and D. Kip, “Observation of parity–time symmetry in optics”, en, Nature Phys **6**, 192–195 (2010).

[237] Z. Lin, H. Ramezani, T. Eichelkraut, T. Kottos, H. Cao, and D. N. Christodoulides, “Unidirectional Invisibility Induced by P T -Symmetric Periodic Structures”, en, Phys. Rev. Lett. **106**, 213901 (2011).

[238] A. Mostafazadeh, “Invisibility and PT symmetry”, en, Phys. Rev. A **87**, 012103 (2013).

[239] L. Feng, Y.-L. Xu, W. S. Fegadolli, M.-H. Lu, J. E. B. Oliveira, V. R. Almeida, Y.-F. Chen, and A. Scherer, “Experimental demonstration of a unidirectional reflectionless parity-time metamaterial at optical frequencies”, en, Nature Mater **12**, 108–113 (2013).

[240] J. S. Toll, “Causality and the Dispersion Relation: Logical Foundations”, en, Phys. Rev. **104**, 1760–1770 (1956).

[241] Y.-C. Lee, M.-H. Hsieh, S. T. Flammia, and R.-K. Lee, “Local P T Symmetry Violates the No-Signaling Principle”, en, Phys. Rev. Lett. **112**, 130404 (2014).

[242] A. Mostafazadeh, “Exact *PT* -symmetry is equivalent to Hermiticity”, en, J. Phys. A: Math. Gen. **36**, 7081–7091 (2003).

[243] A. Mostafazadeh and A. Batal, “Physical aspects of pseudo-Hermitian and *PT* -symmetric quantum mechanics”, en, J. Phys. A: Math. Gen. **37**, 11645–11679 (2004).

[244] R. Fleury, D. L. Sounas, C. F. Sieck, M. R. Haberman, and A. Alù, “Sound Isolation and Giant Linear Nonreciprocity in a Compact Acoustic Circulator”, en, Science **343**, 516–519 (2014).

[245] B.-I. Popa and S. A. Cummer, “Non-reciprocal and highly nonlinear active acoustic metamaterials”, en, Nat Commun **5**, 3398 (2014).

[246] M. Brandenbourger, X. Locsin, E. Lerner, and C. Coulais, “Non-reciprocal robotic metamaterials”, en, Nat Commun **10**, 4608 (2019).

[247] M. Fruchart, R. Hanai, P. B. Littlewood, and V. Vitelli, “Non-reciprocal phase transitions”, en, Nature **592**, 363–369 (2021).

[248] A. R. Katko, S. Gu, J. P. Barrett, B.-I. Popa, G. Shvets, and S. A. Cummer, “Phase Conjugation and Negative Refraction using Nonlinear Active Metamaterials”, en, Phys. Rev. Lett. **105**, 123905 (2010).

[249] A. Ghatak, M. Brandenbourger, J. van Wezel, and C. Coulais, “Observation of non-Hermitian topology and its bulk-edge correspondence”, en, Proceedings of the National Academy of Sciences **117**, 29561–29568 (2020).

[250] S. Shankar, A. Souslov, M. J. Bowick, M. C. Marchetti, and V. Vitelli, “Topological active matter”, en, Nat Rev Phys **4**, 380–398 (2022).

[251] C. Scheibner, A. Souslov, D. Banerjee, P. Surówka, W. T. M. Irvine, and V. Vitelli, “Odd elasticity”, en, Nat. Phys. **16**, 475–480 (2020).

[252] M. Fruchart, C. Scheibner, and V. Vitelli, “Odd Viscosity and Odd Elasticity”, en, Annu. Rev. Condens. Matter Phys. **14**, 471–510 (2023).

[253] M. Brandenbourger, C. Scheibner, J. Veenstra, V. Vitelli, and C. Coulais, *Limit cycles turn active matter into robots*, en, arXiv:2108.08837 [cond-mat], June 2022.

[254] L. Jin, R. Khajehtourian, J. Mueller, A. Rafsanjani, V. Tournat, K. Bertoldi, and D. M. Kochmann, “Guided transition waves in multistable mechanical metamaterials”, en, Proc. Natl. Acad. Sci. U.S.A. **117**, 2319–2325 (2020).

[255] A. Zareei, B. Deng, and K. Bertoldi, “Harnessing transition waves to realize deployable structures”, en, Proc. Natl. Acad. Sci. U.S.A. **117**, 4015–4020 (2020).

[256] A. Demiquel, V. Achilleos, G. Theocharis, and V. Tournat, “Modulation instability in nonlinear flexible mechanical metamaterials”, en, Phys. Rev. E **107**, 054212 (2023).

[257] B. Deng, J. Li, V. Tournat, P. K. Purohit, and K. Bertoldi, “Dynamics of mechanical metamaterials: A framework to connect phonons, nonlinear periodic waves and solitons”, en, Journal of the Mechanics and Physics of Solids **147**, 104233 (2021).

[258] B. Deng, J. R. Raney, K. Bertoldi, and V. Tournat, “Nonlinear waves in flexible mechanical metamaterials”, en, Journal of Applied Physics **130**, 040901 (2021).

[259] C. Jiang, E. Beneduce, M. Baggioli, C. Setty, and A. Zaccone, “Possible enhancement of the superconducting Tc due to sharp Kohn-like soft phonon anomalies”, en, J. Phys.: Condens. Matter **35**, 164003 (2023).

[260] N. K. Nepal, P. C. Canfeld, and L.-L. Wang, *Imaginary phonon modes and phonon-mediated superconductivity in Y2C3*, en, arXiv:2308.00201 [cond-mat], July 2023.

[261] C. Setty, M. Baggioli, and A. Zaccone, *Anharmonic theory of superconductivity and its applications to emerging quantum materials*, en, arXiv:2303.12977 [cond-mat], Mar. 2023.

Hobelwerkweg 41
8404 Winterthur
Switzerland
📱 *+4176 498 04 60*
✉ *aleksi.bossart@epfl.ch*
iD *0000-0003-4323-4360*
in *aleksi-bossart*

Aleksi Bossart

Physicist

Publications

Aleksi Bossart and Romain Fleury. Extreme spatial dispersion in nonlocally resonant elastic metamaterials. *Physical Review Letters*, 130:207201, May 2023.

Aleksi Bossart and Romain Fleury. Non-hermitian time evolution: From static to parametric instability. *Physical Review A*, 104:042225, Oct 2021.

Andrea Francesco Battaglia, José Roberto Canivete Cuissa, Flavio Calvo, Aleksi Bossart, and Oskar Steiner. The alfvénic nature of chromospheric swirls. *Astronomy & Astrophysics*, 649:A121, 2021.

Aleksi Bossart, David M. J. Dykstra, Jop van der Laan, and Corentin Coulais. Oligomodal metamaterials with multifunctional mechanics. *Proceedings of the National Academy of Sciences*, 118(21):e2018610118, 2021.

Aleksi Bossart and Wellington Galleas. Functional relations in nineteen-vertex models with domain-wall boundaries. *Journal of Mathematical Physics*, 60(10):103509, 10 2019.

Conferences

Symposium on Acoustic Metamaterials, *talk*, Nîmes, France. **10.2022**

Metamaterials, *talk*, Siena, Italy. **09.2022**

URSI GASS, *flash talk*, Rome, Italy. **09.2021**

Waves in Time-Varying Media, *poster*, online. **03.2021**

Positions

Ph.D. candidate, EPF Lausanne. **09.2019–**
Research on nonlocally-resonant elastic metamaterials and time-modulated active media.

Research intern, Universiteit van Amsterdam. **02.2019–08.2019**
Development and testing of mechanical metamaterials.

Research civilist, IRSOL, Locarno. **09.2018–12.2018**
Analysis of swirling structures in magnetohydrodynamic simulations of the solar atmosphere.

Education

MSc. in Physics, ETH Zürich. **09.2016–09.2018**
Thesis on 19-vertex models, in the quantum field theory group.

BSc. in Physics, ETH Zürich. **09.2013–09.2016**
Thesis on characterisation of electronics for a hybrid PET-MRI system, at CERN.